

**Transverse momentum evolution of neutral pion
triggered dihadron correlations in Au+Au
collisions at $\sqrt{s_{NN}} = 200$ GeV**

by

Andrew M. Adare

B.S. Wheaton College, 1998

A thesis submitted to the
Faculty of the Graduate School of the
University of Colorado in partial fulfillment
of the requirements for the degree of
Doctor of Philosophy
Department of Physics

2010

This thesis entitled:
Transverse momentum evolution of neutral pion triggered dihadron correlations in
Au+Au collisions at $\sqrt{s_{NN}} = 200$ GeV
written by Andrew M. Adare
has been approved for the Department of Physics

James L. Nagle

Prof. John Cumalat

Prof. Edward Kinney

Prof. Oliver DeWolfe

Date _____

The final copy of this thesis has been examined by the signatories, and we find that both the content and the form meet acceptable presentation standards of scholarly work in the above mentioned discipline.

Adare, Andrew M. (Ph.D., Physics)

Transverse momentum evolution of neutral pion triggered dihadron correlations in
 Au+Au collisions at $\sqrt{s_{NN}} = 200$ GeV

Thesis directed by Prof. James L. Nagle

Quantum Chromodynamics (QCD) stands as a cornerstone of the standard model and describes interactions occurring at nuclear length scales with the distinctive concepts of color charge, asymptotic freedom, and confinement. As a consequence of these features, a nuclear phase composed of quarks and gluons rather than their composites is predicted to exist at extremely high temperatures and densities, which are nevertheless achievable in the lab through relativistic nuclear collisions.

The experimental observation of this strongly-coupled quark gluon plasma (sQGP) phase of matter is of fundamental scientific interest for reasons including its presence in the early stages of the universe. Much information about the density of the sQGP, the nature of its coupling, and its transport properties can be inferred through the energy loss of fast partons generated by hard scattering processes *in situ* concurrently with the sQGP. These strongly-interacting particles radiate and scatter in their passage through the material before fragmenting into jets of observed color-neutral hadrons, and measurements of the correlated hadron production over a large event sample provide clues about the nature of partonic energy loss and its deposition into the hot nuclear material.

In this analysis, azimuthal correlations between neutral pions at moderate to high transverse momentum ($p_T = 4-12$ GeV/ c) and associated unidentified charged hadrons ($p_T = 0.5-7$ GeV/ c) are presented in $Au+Au$ and $p+p$ collisions at $\sqrt{s_{NN}} = 200$ GeV. Interpretation of the correlations is simplified by the exclusive use of π^0 trigger particles, which reduces potential influences of recombination effects compared to unidentified dihadron correlations. In central Au+Au collisions, an alteration is

observed in comparison to a p+p reference as partner p_T increases. In the direction opposing moderate-momentum leading π^0 s ($4 < p_T < 7$ GeV/ c), a medium-modified shape and enhanced yield evolves toward a suppressed but unmodified jet peak shape. At higher trigger p_T , however, the jet shape maintains consistency with p+p over the entire partner p_T range, although a similar trend from enhancement toward suppression in the jet pair yield modification remains. The same-side correlations indicate a weak modification in the jet yield at low trigger and partner p_T , while the jet peak shape reflects no discernible medium influences. The quantitative description of these trends over a broad momentum range provides new constraints on energy loss, fragmentation, and medium response scenarios attempting to describe the data.

Dedication

To mom, dad, Laura, Lou, Cathy, and the rest of my family—you know who you are.

Acknowledgements

Many, many people provided substantial assistance toward the completion of this work. I am indebted to all my colleagues in the PHENIX collaboration, in particular for what I have learned from their hard work and clever experimental acumen, as well as for the magnanimous alphabetical positioning of their surnames.

In particular, I would like to thank Jiangyong Jia for his technical mentorship and groundbreaking work in two-particle correlations, and for his willingness to answer emails, discuss analysis details late at night in the counting house, and provide many lines of code in my early days as a student. Justin Frantz also deserves acknowledgment for his generosity in sharing time, knowledge, and expertise in bringing many of our results to a finished state. His patience and selfless, collaborative attitude will continue to serve as an example to me. Matt Nguyen deserves credit for being one of the hardest-working and most responsive colleagues I have ever worked with. He was always willing to be helpful. Anne Sickles, whose sharp insight is always delivered graciously, has consistently been an excellent person to work with, and someone whose opinions and suggestions were always worth careful consideration. Mike McCumber deserves particular credit, especially in light of his reticence to secure it for himself. He stepped in repeatedly and with impressive proficiency to handle several critical tasks as the results in this work have progressed toward publication.

I owe thanks to my colleagues at CU Boulder; namely L. Alex Linden-Levy, whose cleverness, technical ability, and affability provided many learning opportunities and

laughs, and Matt Wysocki, whose encyclopedic knowledge of C++ and other computing topics were always helpful, especially when I was at a loss for what to look up. My advisor Jamie Nagle has remained one of the best scientists that one could hope to study under throughout my doctoral education. He always balanced his high standards and critical insights with fairness and generosity. He exploited his cleverness and abundance of good ideas on many occasions to position his students in a more favorable light, and was content to do so. An overlooked part of an education is training in character and in the art of making good decisions. To this end, I have received top-level instruction from someone who routinely stayed up all night in graduate school but does not require the same of his students.

Finally, I would like to thank my family, both at home, and at ASCB, whose support throughout the whole process of attaining my doctorate will never be forgotten.

Contents

Chapter

1	Introduction: the strong force, color, and phases of nuclear matter	1
1.1	The standard model	1
1.2	Quantum chromodynamics	2
1.2.1	Confinement and asymptotic freedom	3
1.2.2	Lattice gauge theory	5
1.2.3	Partonic fragmentation in e^+e^- and pp collisions	6
1.3	Phases of nuclear matter and the quark-gluon plasma	9
1.4	Heavy-ion collisions	14
1.4.1	Anisotropic flow	17
1.4.2	Hard scattering and jets	19
1.4.3	Energy loss	22
1.5	Two-particle correlations	25
1.6	Recent measurements and model predictions	27
1.6.1	Di-jet quenching and enhancement	30
1.7	Scope and purpose of this analysis	31
2	The PHENIX experiment at RHIC	34
2.1	The Relativistic Heavy Ion Collider	34
2.2	Overview of the PHENIX detector	36

2.3	Triggering and data acquisition	39
2.4	Global event characterization	40
2.4.1	BBC and ZDC	40
2.5	Central Arm Spectrometers	42
2.5.1	Central Arm Magnets	43
2.5.2	Electromagnetic Calorimeters	44
2.5.3	Drift chambers	46
2.5.4	Pad chambers	47
2.5.5	Ring imaging Cherenkov detector	49
2.5.6	Tracking in the central arms	51
2.6	The EMCal-RICH trigger	56
3	Data analysis	58
3.1	Centrality determination	58
3.2	Two-particle correlation framework	61
3.2.1	Event mixing and background normalization	62
3.2.2	The two-source model and elliptic flow as a residual correlation	63
3.2.3	The ZYAM method	65
3.2.4	The ABS method	67
3.3	Event mixing	71
3.4	Data quality	72
3.4.1	Event selection	72
3.4.2	DAQ runs and run QA	73
3.5	π^0 identification	75
3.5.1	Rejection of hot EMCal towers	80
3.5.2	Handling charged track contamination in photon clusters	81
3.6	Charged hadron track selection and high- p_T background	83

3.6.1	Background in charged tracks	84
3.6.2	Track quality	86
3.7	PC3 matching	88
3.8	Summary of track cuts	91
3.9	Elliptic flow measurements and background subtraction	92
3.10	Correlation functions	95
4	Data corrections and systematic uncertainties	96
4.1	Single-particle acceptance \times efficiency: Monte Carlo method	98
4.1.1	Generation	98
4.1.2	Simulation and Reconstruction	99
4.1.3	Momentum resolution	102
4.1.4	PC3 matching recalibration	102
4.1.5	Acceptance correction	104
4.1.6	Evaluation	108
4.1.7	Combining particle species	109
4.1.8	Systematic uncertainties for single-particle efficiency correction	110
4.2	The bootstrap method as a cross-check	111
4.3	Occupancy efficiency	112
4.3.1	Details of the study	115
4.3.2	Run 7 results	116
4.3.3	OEC cross-check and systematic uncertainties	117
5	Results and their uncertainties	119
5.1	Conditional jet pair yields	119
5.2	Systematic uncertainties on conditional yields	122
5.2.1	π^0 combinatoric background (type B)	123
5.2.2	Uncertainty from v_2 measurements (type B)	125

5.2.3	Charged hadron background (type B)	125
5.2.4	Background normalization (type B)	126
5.2.5	h^\pm efficiency correction (Type C)	126
5.3	Extracting jet shape information from conditional pair yields	127
5.3.1	Other shape parametrizations	131
5.4	Integrated yields and I_{AA}	132
5.4.1	Integrated yield and I_{AA} systematic uncertainties	135
6	Summary, Interpretation, and a Look Ahead	137
6.1	Transverse momentum dependence of jet shapes and yields	137
6.2	Low and intermediate p_T phenomenology: what causes the double peak?	138
6.2.1	Questions concerning the 2-source model	139
6.3	High p_T phenomenology: surface emission or punchthrough?	141
6.4	Conclusion	143
	Bibliography	144
	Appendix	
A	Correlation functions and conditional pair multiplicities	157
A.0.1	General pair correlation functions	157
A.0.2	Angular correlations	158
A.0.3	Conditional pair multiplicities	158
B	The negative binomial distribution	160
C	Run lists for Runs 6 and 7	162
D	$\pi^0 \rightarrow 2\gamma$ decay kinematics	163

D.1	Minimum and maximum decay photon energies	163
D.2	Distribution of decay angles	163
E	PC3 recalibration	166
E.1	PC3 match distributions from embedding output	166
E.2	Matching distributions from PISA simulations	166
E.2.1	Run 6	166
E.2.2	Run 7 embedding simulation output	166
F	Correlation Functions	170
F.1	p+p	170
F.2	Au+Au	171

Tables

Table

2.1	RHIC runs and luminosities	35
2.2	Description of PHENIX subsystems	38
3.1	0-20% ξ values	70
3.2	20-60% ξ values	70
3.3	DCH/PC1 track quality bit encoding	87
3.4	0-20% pair v_2 values	94
3.5	20-60% pair v_2 values	94
4.1	MC / data acceptance \times efficiency agreement	107
4.2	Single-particle acceptance \times efficiency uncertainties	111
5.1	π^0 background uncertainty	125

Figures

Figure

1.1	Ideas leading to the standard model	1
1.2	Light hadron mass spectrum: lattice and experiment	3
1.3	α_s vs. \sqrt{s}	4
1.4	Two-jet event in DELPHI	5
1.5	e^+e^- fragmentation functions	8
1.6	Hadron multiplicities vs. mass	10
1.7	Phase transitions from lattice QCD	13
1.8	QCD phase diagram	14
1.9	PHOBOS $dN_{ch}/d\eta$ distributions	16
1.10	Azimuthal collision diagram	16
1.11	Charged hadron v_2	18
1.12	Hydrodynamic v_2 predictions and data	18
1.13	π^0 , η , and prompt γ R_{AA}	21
1.14	R_{AA} in PHENIX data with model comparisons	26
1.15	Evolution of dihadron correlations with p_T	28
1.16	Fits to $R_{AA}(p_T)$ and $I_{AA}(z_T)$	31
2.1	RHIC diagrams	36
2.2	PHENIX detector configurations	37

2.3	PHENIX DAQ layout	39
2.4	PHENIX BBC	41
2.5	Central arm magnetic field configurations	43
2.6	EMCal elements	45
2.7	Drift Chamber photo and diagram	47
2.8	Pad chambers	48
2.9	PC pad and cell layout	48
2.10	RICH diagrams	51
2.11	DC tracking	52
2.12	Diagram of measured and initial tracking parameters	54
2.13	Track association efficiency	56
2.14	ERT tile layout	57
3.1	N_{part} and N_{coll} vs. impact parameter	59
3.2	N_{part} and N_{coll} distributions from GMC	60
3.3	Single-particle multiplicities	68
3.4	Single-particle multiplicities and residual multiplicity correction factor	68
3.5	Same- and mixed-event pair distributions	72
3.6	χ^2 distributions of $C(\Delta\phi)$ for central Au+Au	75
3.7	π^0 - γ decay angle distribution	76
3.8	Au+Au π^0 mass plots	78
3.9	Minimum photon energy cut	79
3.10	Tower hit frequency distribution in Run 7 EMCal sectors	81
3.11	Bad EMCal towers in Run 7	82
3.12	charged track contamination	82
3.13	charged track veto	83

3.14	PISA simulation of difference between true and reconstructed track momenta.	84
3.15	Track quality distributions	87
3.16	Examples of PC3 matching distributions for two different track p_T ranges	90
3.17	Ratio of p_T distributions with loose and tight PC3 mtach cuts	91
3.18	Run 7 $\pi^0 v_2$	93
3.19	Run 7 π^0 and $h^\pm v_2$ for combined centralities.	94
4.1	BBC tube hit multiplicities and z-vertex resolution	100
4.2	Two different z-vertex smearing distributions	101
4.3	PISA momentum resolution distribution	103
4.4	DCH/PC acceptance	106
4.5	Run 6 ϕ and z acceptance projections	107
4.6	Run 7 ϕ and z acceptance projections	107
4.7	Breakdown of cut efficiencies	108
4.8	Particle ID ratios for combining efficiencies	109
4.9	PID ratio errors	110
4.10	Run 6 single-particle acceptance \times efficiency curves	113
4.11	Run 7 single-particle acceptance \times efficiency curves	114
4.12	DC and DC+PC Occupancy efficiency	116
4.13	Occupancy efficiency vs. momentum	117
4.14	OEC centrality dependence cross-check	117
5.1	p+p conditional yields	120
5.2	0-20% Au+Au conditional yields	123
5.3	20-60% Au+Au conditional yields	124
5.4	Near-side σ fit parameters vs. $h^\pm p_T$	128
5.5	Near-side σ fit parameters vs. $h^\pm p_T$	129

5.6	χ^2 for Gaussian fits to jet peaks	130
5.7	Near side integrated conditional yields	133
5.8	Away side integrated conditional yields	133
5.9	Near-side I_{AA}	134
5.10	Away-side I_{AA}	135
6.1	Selection of conditional yields	138
6.2	Demonstrated influence of v_2 on subtracted jet function	140
E.1	PC3 $\Delta\phi$ matching distributions from embedding study	167
E.2	PC3 Δz matching distributions from embedding study	167
E.3	Run 6 PISA matching parameters	168
E.4	Run 6 PISA matching parameters, post-recalibration	168
E.5	Run 7 matching parameters vs. p_T from embedding simulation	168
E.6	Result of recalibration	169
F.1	p+p Correlation functions.	172
F.2	Au+Au Correlation functions, 0-20%.	173
F.3	Au+Au Correlation functions, 20-60%.	174

Chapter 1

Introduction: the strong force, color, and phases of nuclear matter

1.1 The standard model

The standard model of particle physics has been unfortunate to acquire such a prosaic name, given that it represents the most comprehensive and successful scientific theory in history and includes rich, precisely-verified concepts that were far from standard just decades ago. Relying on symmetries in nature and their deep connection with conserved quantities, it represents the unification of electromagnetism, special relativity and quantum mechanics. Notably, gravity remains excluded (figure 1.1). A small collection of quarks, leptons, and gauge bosons economically describes all visible matter and the interactions therein. They exist in a three-generation mass hierarchy as the quanta of symmetry-breaking fields in their excited states.

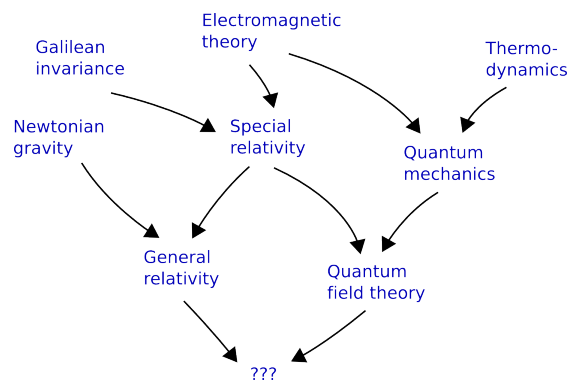


Figure 1.1: The intellectual heritage of general relativity and quantum field theory, the two primary but incompatible components of modern physics. The standard model is fundamentally rooted in quantum field theory, but does not include gravity. The strong interaction is well described by the QCD sector of the standard model.

The electroweak sector of the SM incorporates quantum electrodynamics (QED) as a calculational framework to account for nongravitational macroscopic forces and

the weak interactions governing radioactive decays and neutrino physics. Using perturbation theory, QED has exploited the small size of the electromagnetic coupling $\alpha_{EM} \approx 1/137$ with compelling success. For example, QED calculations involving α_{EM} and precise measurements of the electron's mass and anomalous magnetic dipole moment have demonstrated agreement between theory and experiment to the tune of one part in a billion, making it one of the most precisely verified theories ever.

The Higgs mechanism [47] is incorporated in the electroweak sector to render the elementary particles massive. In the advent of the Large Hadron Collider era, there is considerable excitement surrounding the possibility of directly observing the quanta of the Higgs field, whose place in the SM is currently justified on theoretical grounds only.

In an important sense, however, the Higgs mechanism is only a small part of the story. Over 99% of the mass in the visible universe is composed of protons and neutrons, and only about one percent of this mass is attributable to the light quarks that compose them. That tiny fraction is obtained from spontaneous electroweak symmetry breaking via the Higgs mechanism or from the process of chiral symmetry breaking [54]. The remainder comes instead from the energy of interaction ($m = E/c^2$) between the partons (quarks and force-carrying gluons) confined within nuclei. These interactions dominate at nuclear and sub-nuclear length scales, and are in fact well described by quantum chromodynamics (QCD), the theory inhabiting the strong sector of the standard model.

1.2 Quantum chromodynamics

QCD is cut from the same theoretical cloth as QED, but it contains an essential difference. All of the kinematics and dynamics of the theory are compactly encapsulated in the Lagrangian density [43]:

$$\mathcal{L}_{QCD} = i\bar{\psi}\gamma^\mu\partial_\mu\psi - g\bar{\psi}\gamma^\mu\psi A_\mu^a - m\bar{\psi}\psi - \frac{1}{4}F_{\mu\nu}^a F_a^{\mu\nu} \quad (1.1)$$

The fermion fields ψ are 4-component Dirac spinors representing quarks, and $F_{\mu\nu}^a = \partial_\mu A_\nu^a - \partial_\nu A_\mu^a - gf^{abc}A_\mu^b A_\nu^c$. Summation over flavors a is implied. The Lagrangian of QED has a very similar structure to equation 1.1, but the gauge potential A_μ is a real-valued massless scalar field (the photon) that couples to electric charge. In QCD this quantity is instead a 3×3 matrix gluon field able to interact with three color charges. The symmetry thus belongs to the $SU(3)$ gauge group as opposed to $SU(2) \times U(1)$ for the electroweak theory. The final term in $F_{\mu\nu}$ is a commutator which vanishes in QED, but not in QCD. The physical consequence of this non-Abelian behavior is that while photons do not couple to other photons, gluons interact with each other and even themselves. This unique feature is ultimately responsible for all the remarkable phenomena of QCD.

Many aspects of QCD are understood well enough to calculate the light hadron masses to excellent agreement with experiment [40], as shown in figure 1.2. Such calculations provide compelling evidence that QCD is on the right track as a correct theory of the strong force.

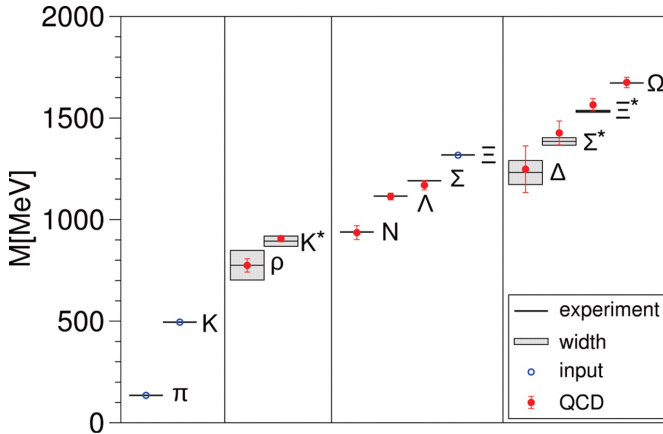


Figure 1.2: Light hadron mass spectrum as measured by experiment (dark lines and bands) and as calculated by lattice QCD simulations (red) [40]. The calculational inputs m_{ud} and m_s were set from the π , K and Ξ masses. With the coupling strength as the only additional input, excellent agreement is obtained with measured masses.

1.2.1 Confinement and asymptotic freedom

Quantum field theory prescribes the existence of antiparticles, which constantly appear ephemerally in pairs with their ordinary counterparts in accordance with the

uncertainty principle. Thus the vacuum is a busy, dynamic place, and is not “empty” in a strict sense as dictated by classical theory. This is one reason gravity is now incompatible with the standard model: general relativity offers a smooth, geometrical description of spacetime that does not account for these roiling microscopic fluctuations. Strongly-interacting particles interact with the vacuum fluctuations in an inherently different way than do the particles of QED, with profound consequences.

Since the transient particle-antiparticle pairs populating the vacuum resemble dipoles, the vacuum itself becomes polarized in the presence of charge, effectively screening the source and imparting a distance dependence to the measured charge, and a “running” of the coupling parameter. In QED this charge screening effect reduces the apparent field at greater distance, or equivalently, at smaller 4-momentum transfer Q^2 . Conversely, greater probe energies resolve details closer to the charge source, and a stronger charge is measured. In QCD, however, color charges behave in the opposite manner such that harder interactions expose a *weaker* coupling than softer probes (figure 1.3). This anti-screening effect is connected to gluon self-interaction and implies two

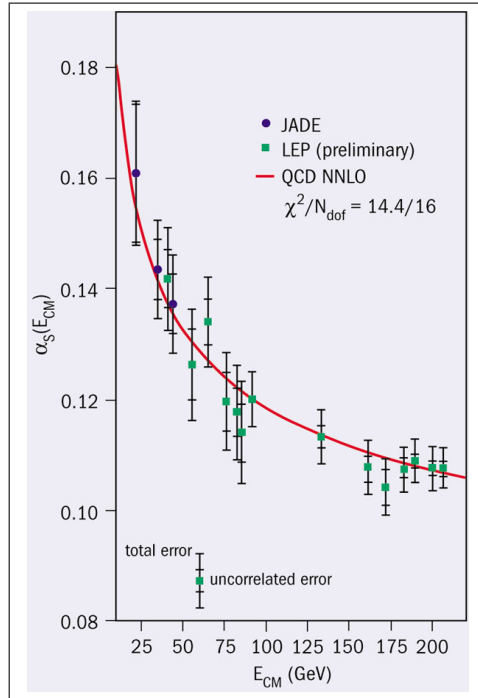


Figure 1.3: Evolution of the strong coupling parameter α_s as a function of center-of-mass beam energy from the JADE experiment at DESY and LEP at CERN [42]. The red curve depicts a prediction from perturbative QCD. In contrast to electrodynamics, the coupling becomes weaker at higher observational energies according to the phenomenon of asymptotic freedom. At lower energies, the growth of the coupling diminishes the efficacy of perturbative QCD, and lattice computations are of greater avail.

critical features, which are the cornerstones of QCD. These features, first described in 1971 by Gross, Politzer and Wilczek, are confinement and asymptotic freedom [73]. As probe energies increase to levels sufficient to resolve features at the femtometer scale, α_s becomes weak, and perturbation theory faithfully describes the data. Thus asymptotic freedom says that the partons are free in the sense that they do not notice each other when observed at energies asymptotically approaching infinity.

Confinement is the other side of the same coin: stronger coupling is observed at greater interquark distances, for instance those corresponding to lower beam energies in figure 1.3. The energy between quarks increases with separation as for an outstretched spring, and the partons remain bound at the fermi scale as color-neutral hadrons, either in pairs as mesons or in triplets as baryons. If quarks are forced apart by a violent collision, the energy of separation in the gluon fields can exceed the threshold for production of new quanta, and the particles regroup into additional hadronic states in a process known as jet fragmentation. Isolated quarks or gluons have thus never been directly observed, but their presence is inferred from the hadronization that occurs in hard scattering events such as the one in figure 1.4.



Figure 1.4: Event display of 2-jet production from the DELPHI experiment at CERN. The outgoing tracks composing the jets are imaged in the detector as the hadronic remains of a fragmented $q\bar{q}$ pair from the decay of a Z^0 boson produced in a $\sqrt{s} = 205$ GeV e^+e^- collision at LEP.

1.2.2 Lattice gauge theory

Due to the large coupling, perturbation theory becomes unreliable as the confinement regime is approached. Lattice gauge theory was developed to numerically simulate QCD statistical ensembles at equilibrium, providing an effective but computationally

expensive means of calculating aspects of QCD that are inaccessible to perturbation theory.¹ The full equations of QCD are directly integrated on a spacetime grid, and the results are extrapolated to a continuum limit. Implementations of lattice QCD typically involve transforming a discretized form of the action corresponding to \mathcal{L}_{QCD} into Euclidean space (eq. 1.1 is in Minkowski space) and evaluating the partition function between each lattice site n :

$$Z = \int \prod_n d\bar{\psi}(n)d\psi(n)dU_\mu(n) \exp(-S_E) \quad (1.2)$$

There are three fermion fields ψ at each lattice point, one for each color degree of freedom. The Euclidean action on the lattice is expressed in terms of the so-called link variables $U_\mu(n)$ which serve as the gauge fields A_μ in the simulation. The variables of a thermal QCD system can then be calculated as derivatives of $\ln Z$, or expectation values can be obtained by including operators within the integral. Due to difficulties in accounting for higher-order effects such as $q\bar{q}$ loops, lattice calculations often involve significant approximations. For example, the integral in equation 1.2 requires the evaluation of the determinant of a large spacetime matrix, which is replaced by a constant in the so-called quenched approximation, or it can be expanded in inverse powers of the quark masses as an improvement, which can involve unrealistically large mass scales. Despite such approximations, major refinements have been introduced in both computational techniques and algorithms since lattice gauge theory was initially developed. The result shown in figure 1.2 represents a major triumph of the systematic precision that has recently been achieved in lattice QCD calculations.

1.2.3 Partonic fragmentation in e^+e^- and pp collisions

Because the fragmentation process occurs as the partonic separations extend beyond the ~ 1 fm confinement scale, the large coupling at such lengths precludes a

¹ See [69] for a good introduction.

perturbative description, despite the high energies associated with jets. Moreover, lattice techniques have offered little direct help, since fragmentation is not modeled well as a thermal system. Instead, fragmentation is parametrized by using fits to data in an approach not unlike the extraction of PDFs, the functions describing parton momentum distributions within hadrons from processes like deep inelastic scattering. A distribution $D_q^h(z)$ of the fragmentation variable $z = E_h/E_q$ represents the probability that a final-state hadron carries a fraction z of the parton's momentum or energy. Hard-scattering processes involving hadrons in the final state are known to be factorizable into a perturbative component describing the initial state and a fragmentation component [38]. This suggests that the fragmentation depends only on the properties of the outgoing partons and is independent of the initial-state process that produces them. Therefore, e^+e^- data are preferred over interactions involving composite particles for extracting fragmentation functions from measured differential cross sections. For example [47], in electron-positron collisions, the quark energy is simply half the center of mass collision energy, and the calculable $2 \rightarrow 2$ component can be removed from measurements of the process

$$\frac{d\sigma(e^+e^- \rightarrow hX)}{dz} = \sum_q \sigma(e^+e^- \rightarrow q\bar{q}) \left[D_q^h(z) + D_{\bar{q}}^h(z) \right] \quad (1.3)$$

to reveal the fragmentation functions. They are then fit with a parametrization such as

$$D_q^h(z) = N \frac{(1-z)^n}{z}. \quad (1.4)$$

Since fragmentation functions are normalized probability distributions, jet multiplicities can be estimated from the relation

$$n_h = \sum_q \int_{z_{min}=2m_h/\sqrt{s}}^1 dz \left[D_q^h(z) + D_{\bar{q}}^h(z) \right] \quad (1.5)$$

Parametrizations such as eq. 1.4 suggest that hadron multiplicities grow logarithmically with beam energy.

Fragmentation functions have been measured over a broad kinematic range in many different experiments. A compilation of inclusive e^+e^- fragmentation functions

is plotted in figure 1.5. The left panel shows that the slopes of $D(z)$ are comparable

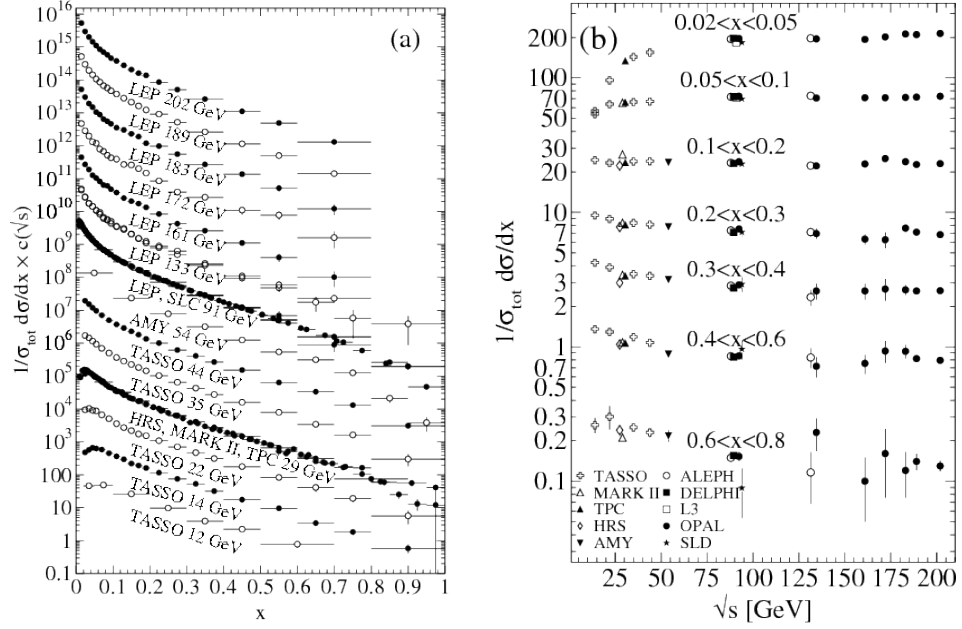


Figure 1.5: Inclusive e^+e^- fragmentation functions from [24] (a) as a function of $x = 2E_h/\sqrt{s}$, scaled for clarity by 10^i , where $i = 0 \dots 13$ for $\sqrt{s} = 12 \dots 202$ GeV. (b): fragmentation functions for various x ranges vs. beam energy.

for $z > 0.2$ for the different collision energies. At lower z values, this scaling behavior is broken for two reasons. The first is that gluons are radiated in the final state at higher orders, and the probability for this to happen increases with Q^2 . The gluons have a softer fragmentation, so their contribution at low z increases with beam energy. Secondly, as the threshold for charm and beauty production is crossed, their contribution at low z becomes substantial as well.

It is possible to obtain some information about the flavor of the parton from the final state from charge and isospin, as well as whether the parent parton is a quark or a gluon. For instance, gluons are not emitted at leading order in e^+e^- annihilation, so gluon fragmentation functions can only be extracted in reactions where a hard gluon is radiated, a phenomenon manifested in three-jet events.

Armed with the universally-applicable fragmentation information from e^+e^- data,

it is possible to move to the more complicated proton-(anti)proton case, where the initial-state quarks carry a fraction x of the proton's momentum as given by the PDFs. The number of possible processes increases since there the initial state can be a combination of quarks and antiquarks of various flavors as well as gluons.

Jet fragmentation is a key mechanism for the production of hadrons in collider experiments, but in hadronic collisions, particularly collisions of heavy ions, other production mechanisms may become relevant. In particular, the phenomenon of recombination, is believed to come into play when nuclear matter is subjected to extraordinary conditions and experiences a phase transformation to a new state. The physics of this process is described here with a motivation based on the multiplicity of hadronic mass states.

1.3 Phases of nuclear matter and the quark-gluon plasma

By the 1960's, the number of newly discovered hadronic resonances had grown rapidly in step with the energy of the accelerators that produced them. This proliferation led to questions about how to explain such large variety, and what, if any, the limitations are in the number of states. When degeneracies due to spin, charge, angular momentum, etc. were taken into account, the number of hadronic states was found to rise exponentially with mass (see figure 1.6 for a modern accounting). Several creative ideas emerged as attempts to explain the hadron spectra, but a simple and compelling line of reasoning by R. Hagedorn showed that the energy of a thermal hadron gas, given by the integral of this exponential density of states $\sim e^{m/T_0}$ with its Boltzmann factor, diverged as the temperature approached a limiting value. He concluded [45]:

It follows that T_0 is the *highest possible temperature*—a kind of ‘boiling point of hadronic matter’ in whose vicinity particle creation becomes so vehement that the temperature cannot increase anymore, no matter how much energy is fed in.

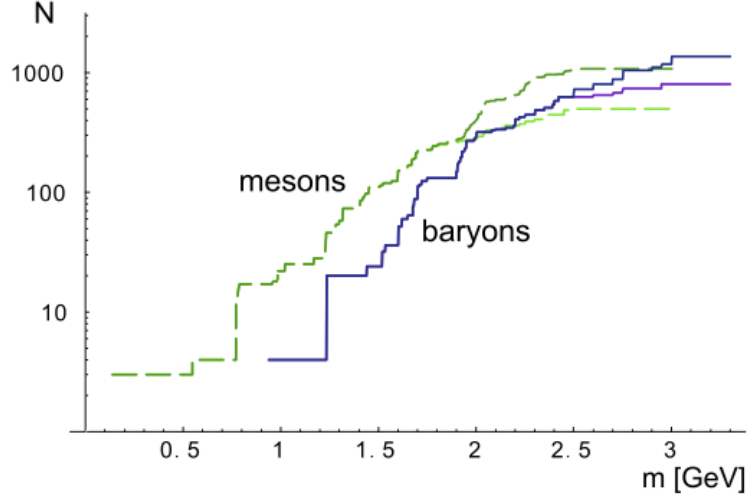


Figure 1.6: A recent accounting of the number of hadronic mass states with increasing mass [35]. The trend remains exponential as observed in the 1960's by R. Hagedorn, implying the existence of an upper bound on the temperature of hadronic matter.

This directly implied a change in the number of fundamental degrees of freedom of the system. Instead of remaining as a gas of hadrons, a superheated system would melt into a phase with simpler constituents at a temperature near T_0 , now known as the Hagedorn temperature. Using the best data available, he extrapolated from the known spectra to obtain a value of T_0 near 160 MeV,² or 10^{12} K.

This indication of a phase transition is corroborated by expectations from asymptotic freedom in QCD. In a thermal medium of partons, the temperature dictates the scale of the momentum transfer. By raising the temperature, or more specifically the energy density, the coupling continues to weaken below a confinement energy scale, and a description of the matter in terms of partonic degrees of freedom becomes more appropriate than that of a large collection of composite, color-neutral particles and resonances. This represents a fundamentally new phase of nuclear matter, the *quark-gluon plasma*.³

² In these units T includes the Boltzman factor $k_B = 8.617 \times 10^{-5}$ eV/K.

³ There is some dissatisfaction among experts over the naming of this state as a plasma, since a conventional (e.g. electromagnetic) plasma is typically understood as a fairly low-density gas whose particles interact very weakly relative to their kinetic energy. This has not been found to be the case

QCD suggests that the deconfinement phase transition is accompanied by a chiral phase transition. Like other systems in nature, these phase transformations are associated with changes in the symmetries of the system. Chiral symmetry is a symmetry of handedness, or invariance between particle pairs whose spin and momenta make them mirror images of each other. Chiral symmetry is an approximate symmetry which is broken in the vacuum to impart mass to the light quarks. It is predicted to be restored near the QGP phase transition, so that the light quarks again become massless.

The equation of state of a partonic system in different thermodynamic regimes is of great theoretical interest. A reference that can be simply calculated is the case of massless partons at high temperature. Assuming thermal equilibrium, the energy density, pressure, and entropy density ϵ , p , and s can be calculated as derivatives of the free energy $F = -T \ln Z$, the partition function being for free quarks and gluons in a volume V :

$$\ln Z(T, \mu, V) = \frac{gV}{2\pi^2 T} \int_0^\infty \frac{dk k^4}{3E} \left[\frac{1}{e^{(E-\mu)/T} \mp 1} + \frac{1}{e^{(E+\mu)/T} \mp 1} \right] \quad (1.6)$$

The first and second terms are for particles and antiparticles, g is the degeneracy, and the free-particle dispersion $E = \sqrt{k^2 + m^2}$ applies. For gluons (more generally for bosons) $\mu = 0$ and eq. 1.6 evaluates to [69]

$$T \ln Z|_{bosons} = \frac{g_b V}{90} \pi^2 T^4. \quad (1.7)$$

Fermions are produced in pairs, so $\mu_q = \mu_{\bar{q}} \neq 0$. For this case, eq. 1.6 is evaluated as

$$T \ln Z|_{fermions} = g_f V \left[\frac{7\pi^2}{360} T^4 + \frac{\mu_q^2}{12} T^2 + \frac{\mu_q^4}{24\pi^2} \right]. \quad (1.8)$$

While the gluon degeneracy is 2 spins \times 8 colors = 16, the quark degeneracy is temperature dependent. Accounting for only u, d quarks gives 2 flavors \times 2 spins \times 3 colors experimentally for the QGP, at least in the temperature ranges under recent exploration. E. Shuryak, who coined the original name in 1980, has updated the name to the ‘‘sQGP’’, where s connotes strong coupling.

= 12. Under these conditions, the QGP partition function is

$$T \ln Z|_{QGP} = V \left[\frac{37\pi^2}{90} T^4 + \mu_q T^2 + \frac{\mu_q^4}{2\pi^2} \right]. \quad (1.9)$$

The energy density is

$$\epsilon = \frac{T^2}{V} \frac{\partial \ln Z}{\partial T} + \mu_q n_q = \frac{37\pi^2}{30} T^4 + 3\mu_q^2 T^2 + \frac{3\mu_q^4}{2\pi^2}. \quad (1.10)$$

The pressure is given by $T \ln Z/V$, which is seen to be equivalent to $\epsilon/3$. Thus the QGP equation of state for massless partons at high temperature and at low baryon chemical potential is given by the simple relation

$$\epsilon = 3P \quad (1.11)$$

which provides a useful reference as one compares the state variables at different points in the phase transition. Finally, the entropy density is

$$s = \frac{\partial(T \ln Z)}{\partial T} = \frac{74\pi^2}{45} T^3 + 2\mu_q T \quad (1.12)$$

At high temperatures, the leading terms in the expressions for ϵ , P , and s dominate. Note that the leading prefactor in equation 1.12 is about 4/3 that in equation 1.10, enabling a simple comparison of these quantities if the temperature is scaled out, as is done in figure 1.7, which is discussed below.

For the same reasons noted in section 1.2.3, the scales corresponding to the QGP phase transformation are nonperturbative. Extensive effort has therefore been devoted to understanding the phase change with lattice calculations. An example of such work is shown in figure 1.7, where it can be seen that the energy density and entropy increase in a smooth but rapid fashion near $T = T_c$ indicating a crossover rather than a first- or second-order phase transition as the preferred interpretation. These calculations include u , d , and s quarks, and were carried out at vanishing baryon chemical potential μ_b . The order of the phase transition at finite μ is not yet well known. T_c has been

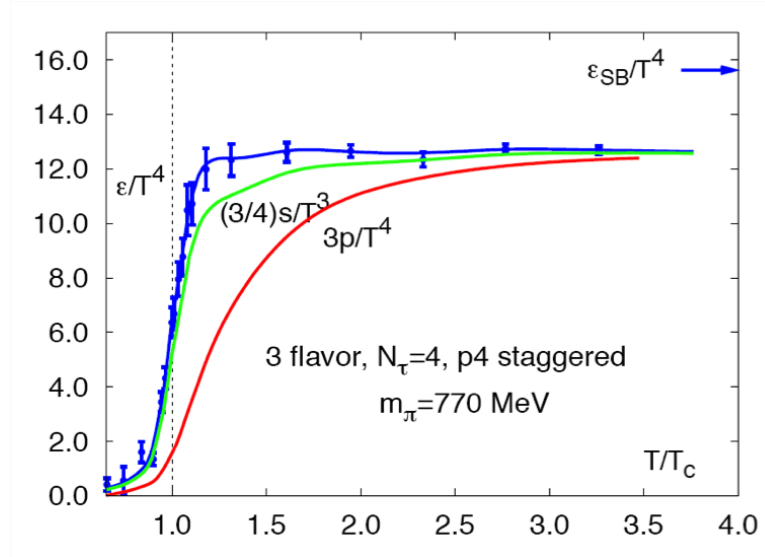


Figure 1.7: Lattice predictions for the phase transition from ordinary nuclear matter to the quark-gluon plasma [61]. Energy density ϵ , entropy density s , and pressure vs. temperature. The Stefan-Boltzmann expectation s_{SB} , valid for a weakly-interacting system, is shown for comparison.

calculated to be 173 ± 8 if only u , d quarks are simulated and 154 ± 8 if strange quarks are included [52].

Since computational expense dictates finite lattice extents, the calculations are performed within a somewhat limited volume with an extent in Euclidean time given by $N_\tau = 1/aT = 4$, where a is the lattice spacing. Newer calculations involving updated implementations of the lattice action and better grid spacing and sizing (e.g. $N_\tau = 6-8$) have been released with quantitatively similar results to those quoted here. The evolution of the equation of state with temperature shows that it is “soft” near T_c , meaning P/ϵ is smallest there, and that the relation approaches equation 1.11 as temperature increases. A rapid rise in the entropy density suggests a liberation of new degrees of freedom during deconfinement. However, the energy density remains at only about 80% of the Stefan-Boltzmann value, indicated by the arrow, suggesting that the matter may remain strongly-coupled well above T_c , and that the thermodynamic picture a free gas of massless quarks and gluons does not appear appropriate until potentially much higher

temperatures are attained.

Experimental probes of nuclear charge density have measured the number of nucleons per volume to be $\rho_0 \approx 0.16 \text{ fm}^{-3}$ [50]. At higher densities, a rich variety of exotic nuclear phases are conjectured (figure 1.8) which may be relevant in environments such as the interior of neutron stars. Among these is the color-flavor locked phase, which may exhibit superfluidity as well as a chromodynamic version of superconductivity [22]. Based on lattice calculations, the QGP transition is expected to occur at energy densities near $0.7 \text{ GeV}/\text{fm}^3$ [34], which can be achieved by increasing some combination of temperature and baryon chemical potential μ .

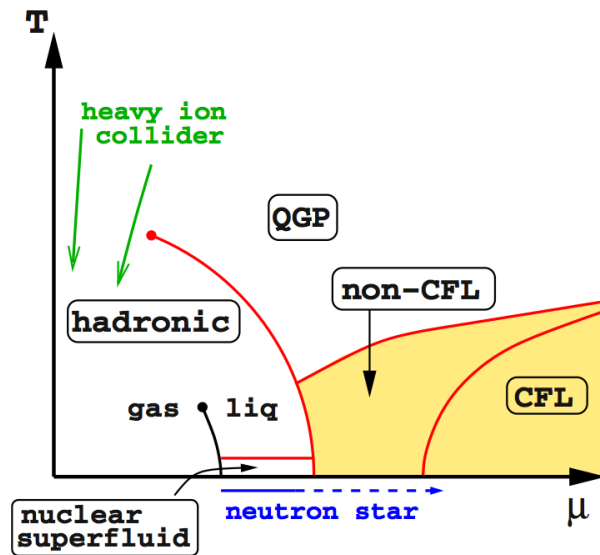


Figure 1.8: Diagram of QCD phases as represented by temperature vs. baryon density from [22]. The low- μ region is accessible at collider energies, while the higher- μ region may contain a perturbatively calculable color-flavor locked (CFL) phase.

1.4 Heavy-ion collisions

There are strong indications that energy densities well in excess of $1 \text{ GeV}/\text{fm}^3$ can be generated in the lab by colliding large nuclei at highly relativistic energies. The next chapter describes in detail the Relativistic Heavy Ion Collider (RHIC), which was

designed specifically for this purpose. At RHIC, Au nuclei ($A = 197$) are collided head-on at center-of-mass energies of 200 GeV per nucleon. At the point of a fully-overlapping collision, a total energy of $2\gamma m_{Au} \approx 39$ TeV is localized in a region of a few fm^3 . Since the relevant energy density is that associated with thermalization, a figure such as $\epsilon = 2\gamma\rho_0^2 \approx 3$ TeV/ fm^3 does not provide a realistic estimate of the available energy density. Instead, the energy involved in local thermal equilibrium processes can be estimated from the transverse energy density of produced particles. For example, the PHOBOS experiment at RHIC has measured the multiplicity of charged particles as distributed in pseudorapidity $\eta \equiv -\ln[\tan(\theta/2)]$, an angular coordinate used with particles when $p \gg m$ for its convenient transformation under Lorentz boosts and its simple mapping to the polar emission angle. The data is shown in figure 1.9 for a variety of centrality categories. Centrality describes the impact parameter of collisions on a statistical basis such that low percentiles correspond to central or head-on collisions. In order to select particles with comparable energies (thus more closely representing a thermalized system), a range of $\eta \pm 1$ is used, corresponding to roughly transverse emission. The mean per-particle energy is estimated from the spectra to be $E_{part} \approx 600$ MeV and the total energy can be estimated as

$$E_{tot} = 2E_{part} \left. \frac{dN_{ch}}{d\eta} \right|_{\eta \leq 1} f_{neut} f_{4\pi} \quad (1.13)$$

The data gives $dN_{ch}/d\eta = 655 \pm 35$ in the midrapidity window for the 6% most central collisions. Applying the correction factors for missing neutral particles and limited acceptance ($f_{neut} = 1.6$, $f_{4\pi} = 1.3$), it is found that about 1.6 TeV is carried away by final-state particles, about 4% of the total energy in the collision region. Allowing a time of 1 fm/c for the particles to interact, the longitudinal extent of the collision region is about 2 fm. Taking a transverse area of 150 fm^2 , the energy density is then estimated to be $\epsilon \approx 5$ GeV/ fm^3 , well above the calculated threshold for QGP formation.

Given the crossing timescale of order 1 fm/c ($\sim 10^{-22}$ s) and the dynamics of

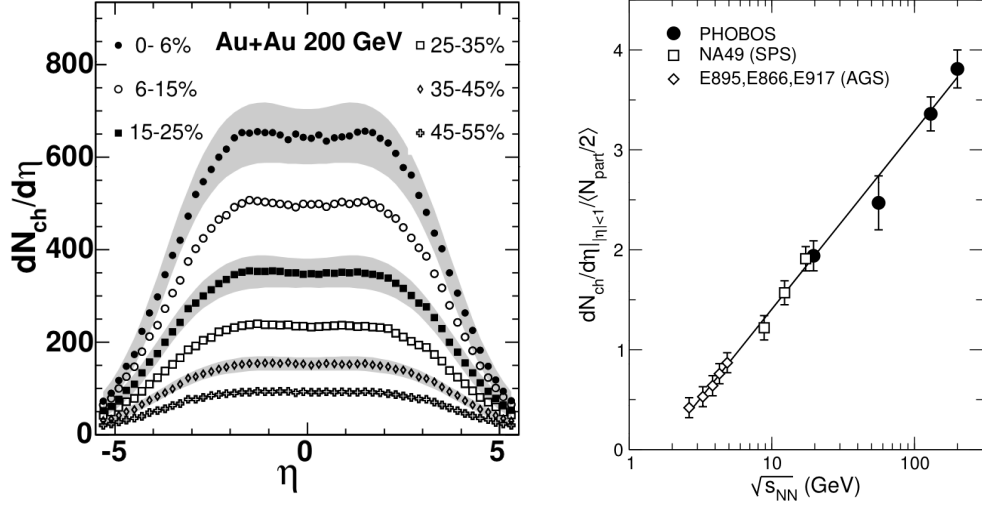


Figure 1.9: Charged particle yields from the PHOBOS experiment [28]. Left: η distribution of charged particles. Right: integrated yield for $|\eta| < 1$ vs. center of mass energy, with lower-energy data added from other experiments. This data can be used to estimate the energy density of a thermalized fireball produced in $Au+Au$ collisions.

expansion and cooling at relativistic rates, it is reasonable to question whether the roughly elliptical collision region, depicted schematically in figure 1.10, contains a truly thermalized system of partonic matter. However, a strong line of experimental evidence has emerged suggesting that the hot nuclear matter (HNM)⁴ achieves a state of strong collective behavior soon after the collision.

1.4.1 Anisotropic flow

As discussed in section 1.3, ϵ and pressure are closely related, and if the eccentric collision region contains a thermalized medium at the estimated densities, pressure gradients of order $\sim 1 \text{ GeV}/\text{fm}^4$ should be produced which are stronger in the reaction plane than normal to it (the event or reaction plane is defined by the beamline and the impact parameter line.) Consequently, a higher density of energetic particles are expected near the reaction plane. Although the HNM cools into hadrons measurable in

⁴ To avoid presumption that the QGP is definitively created in heavy ion collisions, the pre-hadronized medium existing in the final state will simply be referred to as hot nuclear matter.

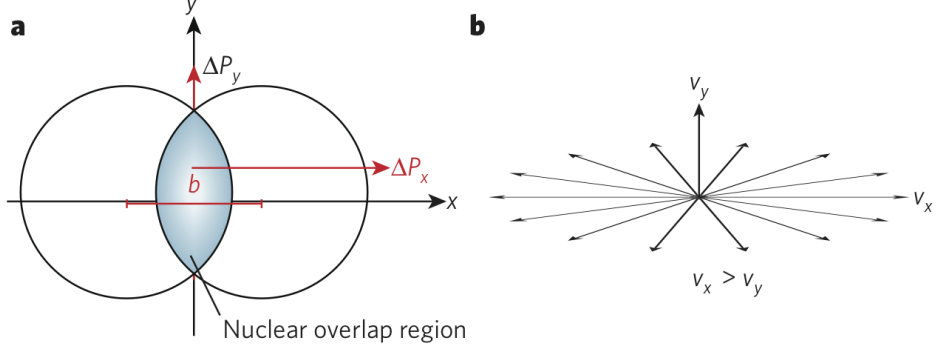


Figure 1.10: Diagram of heavy ions colliding at impact parameter b from a beamline perspective [34]. Pressure gradients within the elliptical overlap region in position space (a) drive anisotropic azimuthal expansion in velocity space (b).

a detector, momentum conservation dictates that the initial momentum anisotropy is preserved. The distribution of outgoing particles can be measured experimentally with high precision. It is commonly parametrized as an azimuthal Fourier series where the second coefficient, v_2 , is by far the largest. Neglecting the other terms,

$$\frac{d^2N}{d\phi dp_T} = N_0 [1 + 2v_2(p_T) \cos 2(\phi - \Phi_{RP})] \quad (1.14)$$

Experimentally, v_2 is measured as

$$v_2 = \frac{\langle \cos 2(\phi - \Phi_{EP}) \rangle}{\langle \cos 2(\Phi_{EP} - \Phi_{RP}) \rangle} \quad (1.15)$$

where the denominator represents the reaction plane resolution. Φ_{EP} , the event plane angle, represents the measured RP value, while Φ_{RP} is the true value. Recent v_2 results are shown in figure 1.11 for charged hadrons near midrapidity for a variety of centrality percentile bins. Specifically, nonviscous models with thermalization times of 0.6 - 1.0 fm/c have been successful, indicating that the viscosity of the thermalized medium is very low. The early time is required because the pre-thermalized eccentricity is reduced with time as the particles stream freely outward, so if hydro “waits” too long to begin, there is not enough spatial eccentricity to drive the strong anisotropic flow that is observed. Although not obvious from the figure, the anisotropic flow is quite

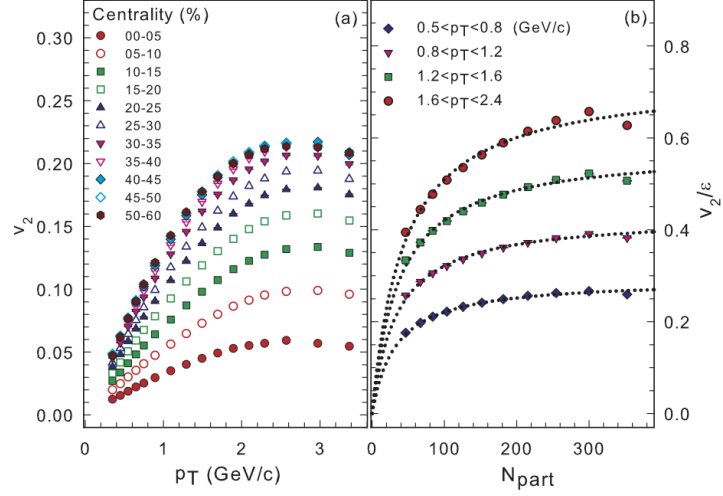


Figure 1.11: Charged hadron v_2 vs. p_T and scaled by eccentricity vs. N_{part} . [8].

large. Calculations based on relativistic hydrodynamic models have successfully reproduced the v_2 measurements below $p_T = 2$ GeV when using ideal assumptions and early thermalizations as input (figure 1.12).

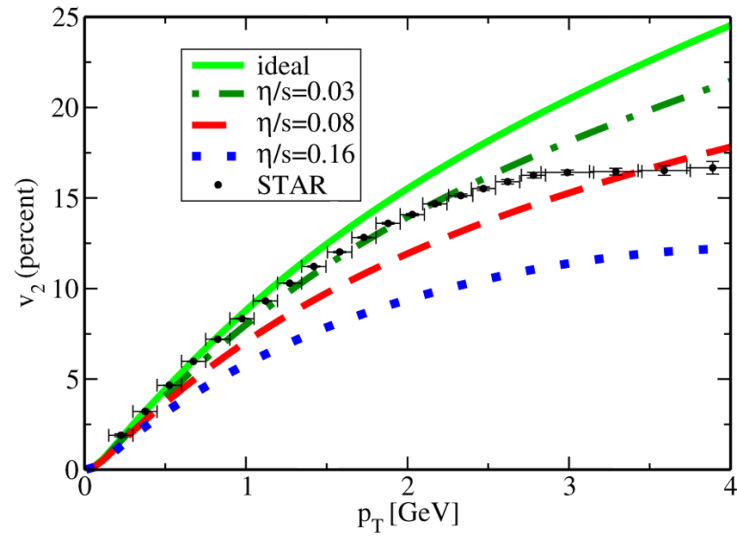


Figure 1.12: Hydronic predictions of v_2 vs. p_T for several ratios of shear viscosity / entropy density and charged hadron data from the STAR experiment. Figure from [64].

The strength of interaction among the particles dictates the degree of mapping

between the initial spatial eccentricity and the momentum eccentricity of the observed final-state particles. The right hand panel shows v_2 normalized by the spatial eccentricity, which is determined from a Glauber Monte Carlo simulation using Woods-Saxon nuclear density profiles [58]. The eccentricity is calculated from the mean over particle positions within a simulated event, denoted by angle brackets, as

$$\epsilon_s = \frac{\langle y^2 \rangle - \langle x^2 \rangle}{\langle y^2 \rangle + \langle x^2 \rangle}. \quad (1.16)$$

At low p_T , v_2/ϵ_s over a large range in the number of collision participants. This scaling behavior shows that for different eccentricities and system sizes, the momentum anisotropy tracks closely with initial eccentricity, indicating a large degree of coupling amongst the particles. As p_T rises, the scaling does not hold as strongly, presumably because an increasing component of the particles are associated with pointlike hard scattering rather than the soft physics of thermalized collective flow.

Although elliptic flow has been introduced here as a phenomenon supporting the existence of a transition into the QGP phase, it is currently an area of intense theoretical and experimental interest in its own right.

1.4.2 Hard scattering and jets

While elliptic flow observables convey information from the soft physics processes of collective motion in the “bulk” of the final-state particles, a small minority of particles produced in partonic scatterings with large momentum transfer afford valuable opportunities to tomographically⁵ image the HNM. These particles carry a large p_T , mass, or both, where “large” means $p_T, m \gtrsim 1$ GeV. Such hard scattering phenomena have served as a critical tool to quantify effects of the nuclear medium, since the high momentum transfer Q^2 is associated with very short timescales ($\tau \sim 1/p_T$) and sub-hadronic lengths. Consequently, perturbative QCD techniques have repeatedly been

⁵ From the Greek word *tomos*, meaning ‘slice’ or ‘section’.

used to accurately describe the data in this kinematic regime. In fact, the leading-order cross section for the hard partonic process $a + b \rightarrow c + d$ in $p + p$ reactions is very similar to the e^+e^- case included in equation 1.3, with the addition of the parton distribution functions $f_{a,b}(x_{1,2})$ [67]:

$$\frac{d^2\sigma}{dx_1 dx_2 d\cos\theta^*} = \frac{1}{s} \sum_{a,b} f_a(x_1) f_b(x_2) \frac{\pi\alpha_s^2(Q^2)}{2x_1 x_2} \sum^{ab}(\cos\theta^*) \quad (1.17)$$

θ^* is the scattering angle in the parton CM frame, and $\sqrt{s} = E_{CM}$. As mentioned in section 1.2.3, the universality of fragmentation functions allows their inclusion from e^+e^- data into a $2 \rightarrow 2$ cross section like eq. 1.17 to predict the spectrum of hadrons. Thus the cross section for hadronic production in $p + p$ is a composition of pointlike partonic interactions, and the $A + A$ cross section can in turn be considered as a composition of independent $N + N$ reactions as a reference.

In $p + A$ or $A + A$ collisions, the number of pointlike $N + N$ binary collisions, N_{coll} , is typically described in the framework of a Glauber model [58] which provides a simple description of the geometry of a nuclear collision. In a Monte Carlo Glauber model, N_{part} and the collision participant multiplicity, N_{coll} , are assigned well-defined mean values over many simulated events for a given nuclear impact parameter.

In absence from effects due to the additional matter, it is expected that the cross section is proportional to $\langle N_{\text{coll}} \rangle$, the proportionality being A for $p + A$ collisions or AB for $A + B$. This simple pointlike geometric dependence is called $\langle N_{\text{coll}} \rangle$ or binary scaling, and it is used to produce a reference for actual $A + B$ yields. The relation between the binary-scaled reference and the $A + B$ data is the nuclear modification factor R_{AB} :

$$R_{AB} = \frac{dN_{AB}}{\langle T_{AB} \rangle d\sigma_{NN}} = \frac{dN_{AB}}{\langle N_{\text{coll}} \rangle dN_{NN}} \quad (1.18)$$

Thus $R_{AB} = 1$ if pointlike binary scaling holds, which is tantamount to demonstrating that the presence of the additional nuclear matter (in either the initial or final state) has no influence on the particle production. For example, photons produced directly

from hard scattering processes such as $qg \rightarrow q\gamma$ interact only electromagnetically with the final-state medium, and even in the RHIC hard scattering regime, $\alpha_{EM} \ll \alpha_s$ so photonic interactions are feeble relative to those experienced by color charges. Direct photons thus suffer essentially no significant modification at RHIC energies at $p_T < \sim 14$ GeV/c, demonstrating that they closely follow binary scaling relations in this range⁶. This phenomenon, shown in figure 1.13, carries at least three highly nontrivial implications: First, the geometric description of pointlike binary scaling from Glauber models are validated by direct observation, serving as an important reference or control for strongly-interacting particles. Furthermore, factorization and universality are applicable calculational tools at these energies⁷. Finally, the modification of nuclear parton distribution functions (relative to nucleon PDFs) is not a large effect at midrapidity.

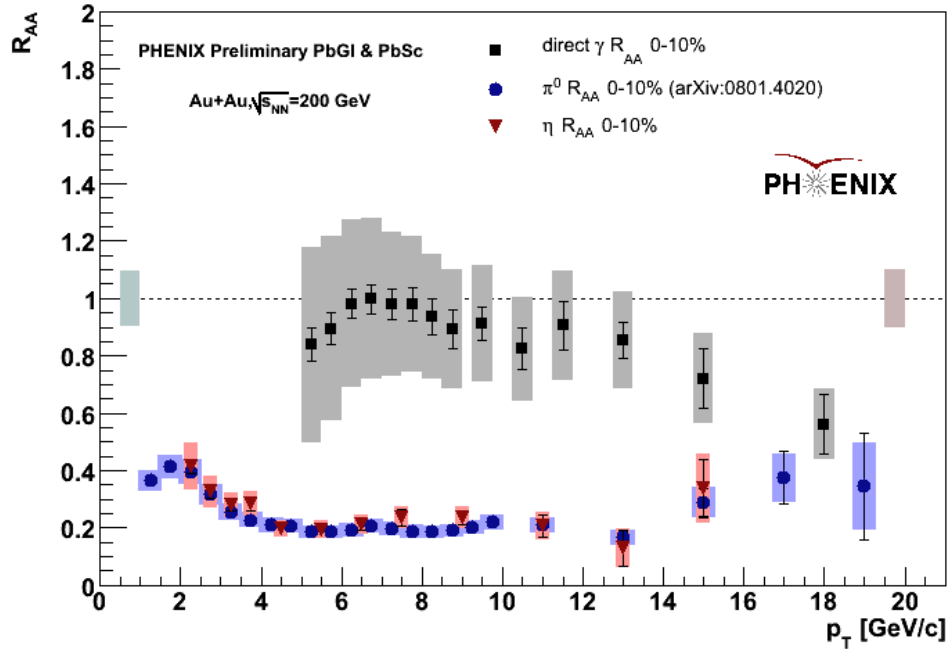


Figure 1.13: π^0 , η , and prompt γ R_{AA} near midrapidity at $\sqrt{s_{NN}} = 200$ GeV. While photons closely follow pointlike geometric scaling, the fragments from quark and gluon jets suffer strong suppression due to the hot nuclear final state.

⁶ The suppression at higher p_T has been explained via nuclear isospin effects (get ref.) which are not related to the hot nuclear final state in any direct way.

⁷ Qualification: the universality of fragmentation functions is not tested in the case of prompt photons.

In contrast to the case of direct photons, binary scaling is strongly violated in central Au+Au collisions for π^0 and η mesons. Above a few GeV, yields are suppressed by a factor of roughly five relative to the N_{coll} -scaled $p+p$ reference. This phenomenon, known as “jet quenching” [39] has been widely observed in the hadronic fragments of fast partons in nuclear collisions. Although not shown here, the suppression has been found to increase as $\langle N_{\text{part}} \rangle$, i.e. the size of the final state, increases according to a scaling relation such that, for example, the same R_{AA} is observed in central Cu+Cu collisions versus mid-central Au+Au data.

It is not immediately clear whether the suppression is due to a downward shift in the $A+A$ spectrum from stopping or absorption of some fraction of the partons, a leftward shift due to loss of partonic energy by most or all outgoing particles, or some combination of the two. In any event, the effect is well described by many theoretical models incorporating energy loss due to radiative and collisional energy loss.

Figure 1.13 does not contain enough information to determine whether the features in R_{AA} are due only to the final-state HNM. However, data from $p+A$ and $d+A$ collisions, which do not represent a hot thermalized system, have shown that nuclear modification indeed occurs, but that it is of a very different nature than that observed in $A+A$. Such so-called cold nuclear matter (CNM) effects are due to the initial state of the collisions and include Cronin enhancement, shadowing, and the EMC effect [56, 53]. Based on the control data, these effects are incapable of accounting for the large suppression observed in $A+A$ data, and in some cases lead to an enhancement in yields relative to binary scaling. These effects must be somehow accounted for when attempts are made to interpret R_{AA} results, although such an accounting is not necessarily straightforward.

1.4.3 Energy loss

The jet quenching effects which are so pronounced in the data have been closely reproduced by a number of models describing energy loss by fast partons traversing a

dense medium of color charges. These models differ significantly in the physical description of the medium, the coupling of the parton to the medium, and the assumptions made, but all have in common that they employ a factorized approach in which the energy loss is expressed as a modification of the fragmentation function. Although the energy loss information is contained in this rescaling of $D(z)$, the final hadronization of the parton occurs in vacuum after the parton has experienced energy loss.

A surprisingly large amount of information about the medium and its coupling to the hard parton can be extracted from a detailed knowledge of the energy loss. In a general way [39], the energy loss ΔE depends on the energy, mass, and charge(s) of the particle, as well as the parton-medium coupling, temperature, and path-length. Other common parameters include the mean free path, defined in terms of the medium density and the interaction cross section as $\lambda = 1/\rho\sigma$; the opacity, expressed as the number of scatterings through a thickness L as $N = L/\lambda$; and the Debye or “thermal” mass of the plasma constituents, which is the inverse of the screening length: $m_D = \langle q^2 \rangle \sim gT$, where $g = 4\pi\alpha_s$.

One of the most widely used energy loss parameters is the transport coefficient \hat{q} [29, 30], which succinctly describes the momentum \mathbf{q} scattered into the medium by the parton as

$$\hat{q} \equiv m_D^2/\lambda = \rho \int dq^2 q^2 \frac{d\sigma}{dq^2}. \quad (1.19)$$

The two general mechanisms considered in parton-medium interaction are collisional and radiative energy loss. The former is an elastic process which is important at low momentum and for lighter quarks, while the latter is an inelastic photon or gluon bremsstrahlung process more dominant at higher momenta. For a single scattering, the radiated energy is given by the integrated spectrum of radiated quanta,

$$\Delta E_{rad} = \int^E \omega \frac{dI}{d\omega} d\omega, \quad (1.20)$$

and a multiplication by the opacity N is sufficient to describe the energy lost by multiple

incoherent scatterings. In close analogy with electrodynamic energy losses due to photon bremsstrahlung, two separate cases are distinguished. The first, called the Bethe-Heitler domain, applies to thin media ($L \ll \lambda$) so that only a single scattering occurs at most on average. The opposite limit, $L \gg \lambda$, is called the Landau-Pomeranchuk-Migdal regime, and the number of scatterings is dictated by the opacity N . This thick-medium case must further distinguish between soft and hard regions of the radiated spectrum because of the so-called LPM effect, named for its discoverers [55, 57]. The LPM effect is a characteristic suppression of low-energy photons (or gluons, in the QCD analog) due to the uncertainty principle. Because the low-energy radiated quanta correspond to longer length scales, they “wash over” the positions of many scattering centers and emerge coherently in reduced intensities. Here “low-energy” resides below a scale ω_c characterizing the average medium-induced energy loss, $\omega_c \approx 2\langle\Delta E\rangle/C_R\alpha_s$. The Casimir factors C_R of the $SU(N_C = 3)$ gauge group include the color factor $C_A = N_C = 3$ and the flavor factor $C_F = (N_C^2 - 1)/2N_C = 4/3$ to differentiate the properties of quarks and gluons.

The probability to radiate gluons in QCD is given by the DGLAP⁸ splitting functions, which are modified from their vacuum representation to account for the presence of the medium. Although the current energy loss calculations differ in various ways, they essentially all predict the following dependence on the medium parameters listed above [39]:

- Bethe-Heitler ($L \ll \lambda$):

$$\omega \frac{dI_{rad}}{d\omega} \approx \alpha_s \hat{q} L^2 / \omega \quad \implies \quad \Delta E_{rad}^{BH} \approx \alpha_s \hat{q} L^2 \ln \frac{E}{(m_D^2 L)} \quad (1.21)$$

⁸ The Dokshitzer-Gribov-Lipatov-Altarelli-Parisi equations describe a modification of nuclear structure beyond a naive valence-quark picture as momentum transfer is increased to resolve gluon contributions from the “sea”. Specifically, the DGLAP evolution equations account for strong increases in the nuclear structure functions F_2 for low- x partons [32]. Such scale-violating behavior has been used to map the running of α_s with Q^2 (see, for example, figure 1.3).

- LPM ($L \gg \lambda$):

$$\omega \frac{dI_{rad}}{d\omega} \approx \alpha_s \begin{cases} \sqrt{\hat{q}L^2/\omega} \\ \hat{q}L^2/\omega \end{cases} \implies \Delta E_{rad}^{LPM} \approx \alpha_s \begin{cases} \hat{q}L^2, & \omega < \omega_c \\ \hat{q}L^2 \ln \frac{E}{\hat{q}^2 L^2}, & \omega > \omega_c \end{cases} \quad (1.22)$$

Equations 1.21 and 1.22 are calculated in the approximation of a static medium of uniform density and composition, leading to a quadratic path length dependence, which is a feature shared with QED energy loss. This strong dependence has been indicated to diminish for rapidly expanding media, however. The infrared suppression is evident from a comparison of the two cases in eq. 1.22, a feature which is also shared with electrodynamic radiative energy loss. The primary distinctiveness of QCD energy loss is marked by the presence of \hat{q} , which quantitatively distinguishes q and g energy loss by implicitly including color factors such that the mean number of radiated gluons is $C_A/C_F = 9/4$ times higher for gluons than quarks. Therefore, since $\Delta E \propto \hat{q}$, gluons lose over twice the energy of quarks at comparable energies.

The flatness of R_{AA} with p_T in large collision systems can thus be explained by a cancellation from competing effects included in equation 1.22 that is essentially coincidental: while the radiative energy loss increases logarithmically with parton energy, it is compensated by (a) an effective hardening of the radiated spectrum due to the LPM effect, and (b) a stronger energy loss in the gluon-dominated low- x region, as described by nuclear PDFs and the linear \hat{q} dependence of ΔE .

A variety of different models are able to reproduce the magnitude of R_{AA} as well as this observed flatness, as shown in figure 1.14. While the agreement is encouraging in one respect, the similarity between the various results also indicates that R_{AA} suffers from an inherent insensitivity in discriminating between calculations that describe distinct physical scenarios. The following section discusses coincidences of multiple jet-related particles and the information they provide in aiding understand of the hot nuclear matter through its interactions with fast partons.

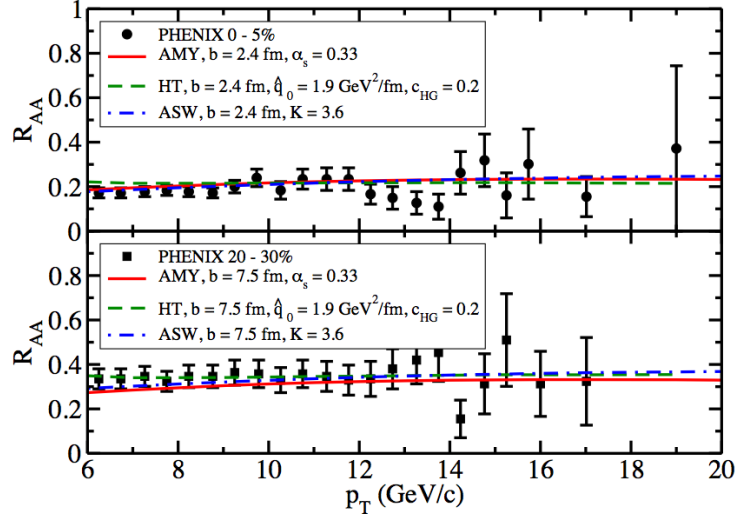


Figure 1.14: Neutral pion R_{AA} in PHENIX data at two different centralities with curves from several different energy loss models. Figure taken from [31]

1.5 Two-particle correlations

Correlated yields of hadrons from jets offer the prospect of gaining significantly more detailed information on energy loss and its deposition in the medium through the evolution of jet shapes and yields with p_T . In this section two-particle correlations are introduced as a means of accessing the physics of energy loss, its deposition into the medium, and other processes.

Quantifying correlations is a common task in physics, but the mathematical implementation varies. The mathematical definition of a correlation function and its relation to a conditional pair multiplicity are described for this context in appendix A. In terms specific to this analysis, particles of type A and type B are measured. Each is produced at some azimuthal angle, and their relative azimuthal angle $\Delta\phi = \phi_A - \phi_B$ is recorded. A is the leading or trigger particle, and B is the associated particle. It is not required that they are different species or in different kinematic categories. A correlation function is a ratio of the distribution of AB pairs produced together (in the same event) to

those produced independently (in different events). If the production of A and B are completely unrelated event-by-event, then the correlation function $C(\Delta\phi) = 1$.

More often, conditional pair yields are shown as the measured result, since they describe the pair production given the existence of a trigger particle. The relationship between the two is derived in the appendix. Selecting a high-momentum type A particle enhances the probability that the event involves a hard scattering interaction resulting in a jet. It is not difficult to imagine by looking at an event like the one in figure 1.4 that the selection of an energetic particle as the trigger, and binning the distribution of $\Delta\phi$ angles formed with its partners in the event, that a characteristic back-to-back jet signature would develop. The trigger is probably aligned with the jet axis, and its angles to the neighboring particles form the “near side” distribution. The opposing jet is on the “away side” at $\Delta\phi \approx \pi$.

If heavy ion events were as clean as this e^+e^- collision, the correlation technique would be unnecessary, since more detailed information about the fragmented parton could be accessed through a complete reconstruction process using tracking and calorimetry. However, the multiplicity of outgoing particles is much higher in a central heavy ion collision at RHIC energies, as demonstrated, for example, by figure 1.9. A correlation function extracts jet signals in busy environments by dividing out the uncorrelated background, and while event-by-event jet information is not preserved, it serves as a powerful statistical method to deal with high-multiplicity backgrounds of uncorrelated particles.

1.6 Recent measurements and model predictions

Recent experimental efforts at RHIC and elsewhere have revealed striking results from correlations of hadron pairs. Figure 1.15 provides a recent and prominent example of such work. In the figure, unidentified charged hadron pairs (primarily pions, kaons, and protons) from central Au+Au collisions are compared directly with those from p+p

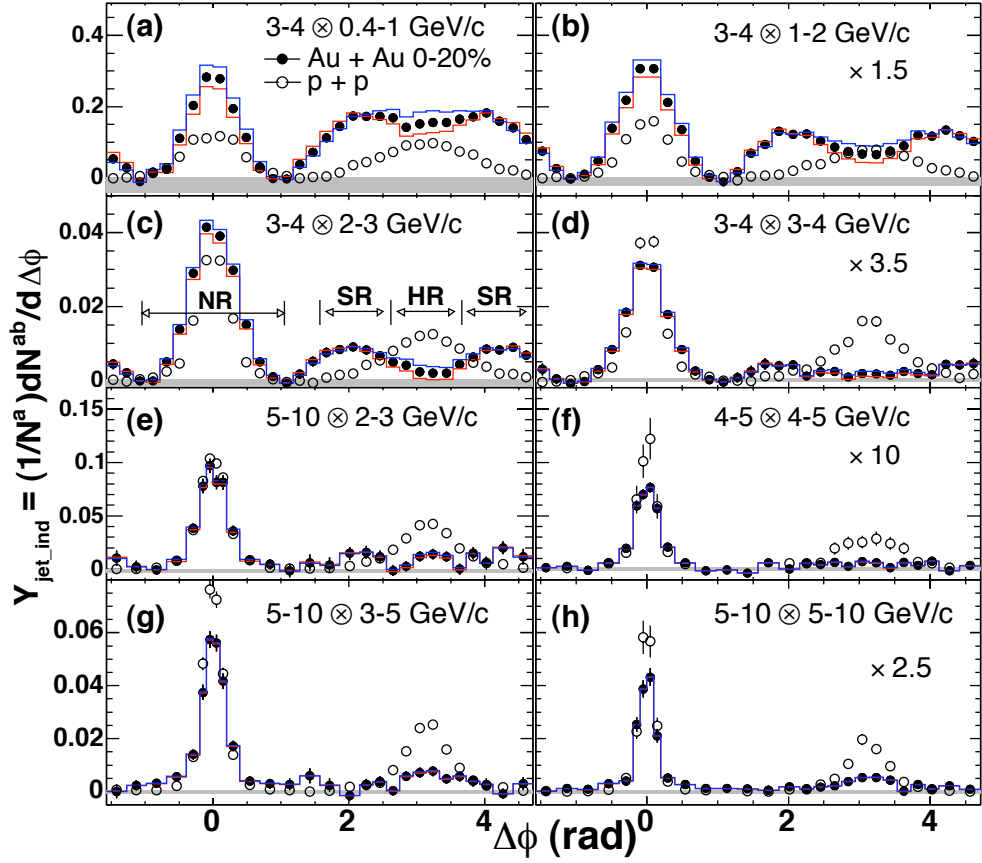


Figure 1.15: Evolution of dihadron correlations with p_T from [7].

collisions at the same beam energy for an assortment of trigger \otimes partner p_T intervals. A striking feature is the presence of the away-side double-peaked structure in the low p_T range, which gives way to a deeply suppressed peak that finally evolves towards a single reduced peak of comparable width to p+p. This shape has become a subject of considerable interest since its discovery, and has invited a variety of detailed speculations as to the mechanism of its origin. Several of these explanations are listed here:

- It has been expected for some time that “gluonsstrahlung” enhanced at large angles due to the interference of forward radiation produces a broadening effect ??, but it has been calculated that under the right conditions, a more extreme bimodal distribution of fragments associated with the radiation can develop [63].

- The excitation of collective sound modes is familiar from less exotic media, and is manifested in Mach shock waves, which have an opening angle in the relativistic case given by [36]

$$\cos \theta_M = \frac{c_s}{\beta} \quad (1.23)$$

where c_s is the speed of sound in the medium.

- Cherenkov radiation is a similar mechanism involving a coherent medium response, but involves optical rather than mechanical modes. The Cherenkov opening angle⁹ is

$$\cos \theta_c = \frac{1}{\beta n} \quad (1.24)$$

where n is the refraction index for gluon radiation, related to the QCD dielectric constant through $n^2 = \epsilon_r$.

- Other structures have been proposed to develop in response to an energetic parton plowing through the dense matter. For example, string theory calculations exploiting the anti-de-Sitter space/conformal field theory correspondence have generated conical bow shocks or diffusion wakes by producing disturbances in the energy-momentum tensor of a supersymmetric plasma [44].
- It has been suggested that fluctuations or three-jet events can produce small anisotropies resembling the double-peak structure. In [27], an event shape analysis was conducted using simulated p+p events to demonstrate that the selection of a certain category of events can produce such a structure in p+p, and that the correlation method may conceivably mimic this selection process.
- Other explanations include the non-negligible presence of a v_3 flow component, deflected jet topologies, and a combined surface bias + flow effect.

⁹ Also see section 2.5.5 for discussion in an experimental context.

- Finally, experimental considerations have not been ruled out, but this topic will be more fully addressed in chapter 6.

In the case of collective modes as a medium response, the Mach and Cherenkov pictures differ in an important way. Since the sound speed c_s is roughly fixed (at least for a given configuration of the medium, corresponding to a specific stage in its evolution), θ_M is not strongly dependent on parton energy. However, dispersion effects ($n = n(\omega)$) in the Cherenkov case impart a gluon energy dependence on θ_c . Small changes in β can correspond to large differences in ω in the relativistic limit, so that θ_c is expected to have a significant dependence on hadron p_T in the correlations.

1.6.1 Di-jet quenching and enhancement

A variable commonly used to quantify the type of yield modification shown in figure 1.15 is I_{AA} , the ratio of conditional jet pair yield in A+A to that in p+p:

$$I_{AA}(p_T^{\text{trig}}, p_T^{\text{assoc}}) = \frac{\left[\frac{1}{N^{\text{trig}}} \frac{dN^{\text{pair}}}{d(\Delta\phi)} \right]_{A+A}}{\left[\frac{1}{N^{\text{trig}}} \frac{dN^{\text{pair}}}{d(\Delta\phi)} \right]_{p+p}} \quad (1.25)$$

Because this observable is derived from quantities with different geometric features than single-particle suppression, it serves as an important complement to R_{AA} so that the requirement that energy loss models match both provides a sharper constraint. For example, I_{AA} has been measured as a function of z_T ,

$$z_T = \frac{p_T^{\text{assoc}}}{p_T^{\text{trig}}} \quad (1.26)$$

which is used as proxy for the fragmentation variable $z = p^{\text{hadron}}/p^{\text{parton}}$ because of its experimental accessibility¹⁰. In figure 1.16, a recent analysis was performed [25] in which the single-particle and pair suppression were fit concurrently to a leading-parton jet quenching calculation that includes a hydrodynamic profile of the medium. The

¹⁰ Care is required in the interpretation of results measured vs. z_T , since it includes effects from fragmentation in both jets, as well as initial state momentum-imbalance effects.

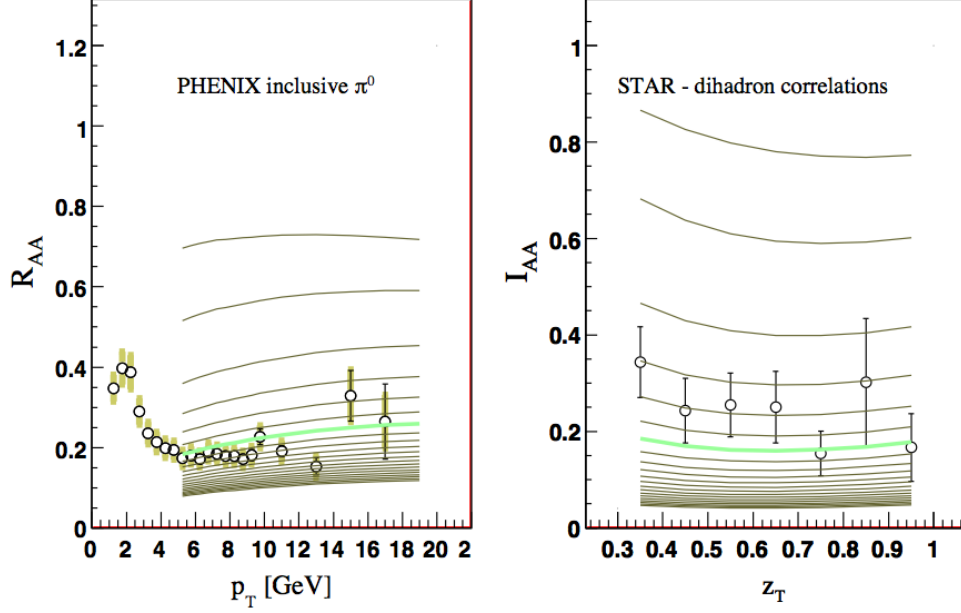


Figure 1.16: Fitting analysis from [25] in which recent measurements of both R_{AA} and I_{AA} are fit to a hydro + E-loss model to extract transport properties of the medium.

calculation models straight-line trajectories through the medium and parametrizes the transport at a point ξ along the path as $\hat{q}(\xi) = K\hat{q}_{QGP}(\xi) \simeq 2K\epsilon^{3/4}(\xi)$, where ϵ is the energy density from a hydrodynamic input and K is the fit parameter. It was found that $K = 4.1 \pm 0.6$, which is a more tightly constrained value than would be obtained through a fit to R_{AA} only.

Such improvements in the constraints on energy loss models are of great importance for improving understanding of sQGP density, coupling behavior, and transport properties through its interaction with energetic partons.

1.7 Scope and purpose of this analysis

Angular correlations from RHIC experiments have already provided critical information about energy loss and medium response, but have introduced several questions as well. Among these questions are:

- At low hadron p_T , what is the observed double-humped structure and its mechanism of formation?
- What role does recombination play as a hadronization mechanism in comparison to jet fragmentation, and what are its effects on the correlations?
- At higher hadron p_T , what are the specific reasons for large reductions in particle yield? If the suppression is due to radiation and scattering in a highly opaque medium, what does this tell us about its density, coupling strength, speed of sound, equation of state, and viscosity?
- What is the specific connection between the behavior at low and high momenta? Where does the onset of vacuum-like fragmentation occur, and how sharp is this transition?
- What is the picture that simultaneously explains the large suppression and an unmodified jet shape? Can the data discern between competing explanations?

Addressing these questions by examining the most energetic (thus rarest) hadrons in event-wise coincidence is challenging due to statistical limitations and other experimental difficulties. The existing data on correlations at high trigger p_T from RHIC experiments have included wide p_T bins to enhance statistical precision, with the consequence of averaging over potentially interesting regions of jet evolution. Moreover, most existing results make use of unidentified charged hadrons as trigger particles, whose relative composition has been measured to vary drastically with p_T . This potentially influences the correlations data due to (a) kinematic effects from hadron mass differences, and (b) jet flavor dependence, since the fragmentation from q vs. g to different hadron states can vary substantially.

In the RHIC 2007 running period, an unprecedented volume of Au+Au collision data (over 4 billion events) was collected with the PHENIX detector, enabling a push

to higher p_T at finer intervals. The PHENIX detector allows statistical reconstruction of neutral pions for use as triggers, and in contrast to charged hadrons measured with PHENIX tracking instruments, their identification *improves* with increasing p_T such that the current upper momentum limits near midrapidity remain statistical.

The use of an identified hadron as the trigger particle thus side-steps complications arising from the baryon anomaly, and this analysis is performed on the largest and most recent Au+Au dataset available. Several experimental improvements have been implemented related to the normalization of background contributions to the correlations and corrections for detector effects, resulting in reduced and carefully-quantified systematic uncertainties. With these implementations, two particle correlations are produced over a wide combined momentum range, providing a new level of detail in mapping the transition with p_T of jet shapes and yields from medium-response dominated features to suppressed and vacuum-like punch-through phenomena which are amenable to perturbative QCD calculations, providing new opportunities to constrain energy loss scenarios in this region.

Chapter 2

The PHENIX experiment at RHIC

2.1 The Relativistic Heavy Ion Collider

The relativistic heavy ion collider (RHIC) [48, 46] at Brookhaven National Laboratory is a synchrotron storage ring 3.8 km in circumference capable of accelerating particles ranging from protons ($A=1$) to Au ions ($A=197$) up to energies 100 GeV/n for Au and 250 GeV for protons. The RHIC consists of two concentric collider rings which intersect at 6 interaction points, each with an independent lattice of superconducting magnets to control acceleration, storage, and collision. Original design luminosities were $2 \times 10^{26} \text{ cm}^{-2} \text{ s}^{-1}$ for Au averaged over a 10 hour storage period (with a fourfold increase in Run 7), with typical bunch populations of 1×10^9 ions. Luminosities are considerably higher for proton beams, reaching $1 \times 10^{31} \text{ cm}^{-2} \text{ s}^{-1}$ with bunch densities 2 orders of magnitude higher. The major parameters of the RHIC runs are shown in table 2.1.

Pre-existing facilities are used for the initial stages of acceleration of Au ions before injection into RHIC at an energy of 8.86 GeV/u. The acceleration process begins at the Tandem Van de Graaff accelerator with a gas of Au^{-1} ions emitted from a pulsed sputter source at ground, which are accelerated to a +14 MeV potential terminal containing a stripping foil. The ions acquire a positive charge q , and continue to accelerate as they are repelled with an energy of $14q$ MeV. A magnetic field selects $q = +12$ ions at 1 GeV/u, which continue through another stripping and selection process upon exiting

	Year	Species	\sqrt{s} [GeV]	$\int Ldt$	$N_{tot(\text{sampled})}$	Data Size
Run1	2000	Au - Au	130	1 b ⁻¹	10 M	3 TB
Run2	2001/02	Au - Au	200	24 b ⁻¹	170 M	10 TB
		Au - Au	19		< 1 M	
		p - p	200	0.15 pb ⁻¹	3.7 B	20 TB
Run3	2002/03	d - Au	200	2.74 nb ⁻¹	5.5 B	46 TB
		p - p	200	0.35 pb ⁻¹	6.6 B	35 TB
Run4	2003/04	Au - Au	200	241 b ⁻¹	1.5 B	270 TB
		Au - Au	62.4	9 b ⁻¹	58 M	10 TB
Run5	2005	Cu - Cu	200	3 nb ⁻¹	8.6 B	173 TB
		Cu - Cu	62.4	0.19 nb ⁻¹	0.4 B	48 TB
		Cu - Cu	22.4	2.7 b ⁻¹	9 M	1 TB
		p - p	200	3.8 pb ⁻¹	85 B	262 TB
Run-6	2006	p - p	200	10.7 pb ⁻¹	233 B	310 TB
		p - p	62.4	0.1 pb ⁻¹	28 B	25 TB
Run-7	2007	Au - Au	200	813 b ⁻¹	5.1 B	650 TB
Run-8	2007/08	d - Au	200	80 nb ⁻¹	160 B	437 TB
		p - p	200	5.2 pb ⁻¹	115 B	118 TB
		Au - Au	9.2		few k	

Table 2.1: Collision species, beam energies, integrated luminosities, and data volumes for Runs 1-8.

the Tandem to produce a beam of Au^{+32} ions.

The beams traverse the 850 m heavy ion transfer line and are injected into the booster synchrotron, where they are collected into six bunches and accelerated to 95 MeV/u. A stripping foil at the booster exit removes all but two of the remaining electrons, and the Au^{+77} ions undergo bunching manipulation upon entrance to the alternating gradient synchrotron (AGS) such that there are 4 bunches with densities of one billion ions/bunch. The Au ions are accelerated to 8.86 GeV/u, and are stripped of their two remaining electrons at the AGS exit.

Injection to RHIC is carried out in the AGS-to-RHIC transfer line in cycles of up to 28 repetitions to give 111 total bunches per ring (one bunch is left empty as an abort gap). The bunches are captured by the RHIC RF acceleration system, which operates at 28.25 MHz, and acceleration from injection energy up to 100 GeV/u is achieved in about 2 minutes. When full beam energy is attained, the beams are transferred to

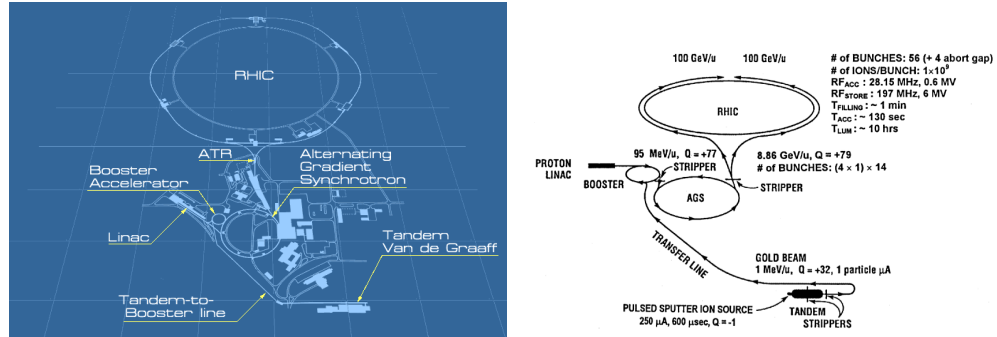


Figure 2.1: Schematic of the RHIC complex.

the RF storage system with an operating frequency of 197 Hz. The storage system is designed to maintain the bunch lengths at or below 30 cm by reducing the effects of scattering within the beams. Finally, the beams are synchronized in preparation for collisions. In the Run 7 111×111 bunch configuration, the bunch spacing is about 34 m or 113 ns, giving a bunch crossing rate of about 8.85 MHz. Even at these Au+Au crossing rates, the PHENIX data acquisition system was fast enough during the 2007 running period to record every event satisfying the minimum bias trigger requirements.

Just outside of each interaction point, the counter-rotating beams are steered into closer proximity by dipole (DX) magnets and the beampipes are merged into a single 8 cm pipe. In the PHENIX interaction region, the beampipe is made of Beryllium, whose low atomic weight reduces conversion background produced by interactions of the outgoing particles with the material.

2.2 Overview of the PHENIX detector

PHENIX [9], the Pioneering High Energy Nuclear Interaction eXperiment, is a tightly integrated collection of close to 20 separate subsystems with hundreds of thousands of detector channels that are digitized and assembled to provide detailed tracking, calorimetry, and particle identification information in the high multiplicity environment of nuclear collisions. The various subsystems employ a variety of technologies and phys-

ical principles to study different aspects of heavy-ion physics, and thus contain built-in cross checks due to their differing sources of systematic uncertainty.

In broad strokes, the PHENIX detector is composed of four spectrometer arms, each covering about one steradian in acceptance. The two central arm spectrometers are positioned near midrapidity on the east and west side of the beampipe, while the northern and southern spectrometers designed for muon tracking and identification surround the beampipe at forward and backward rapidity. In addition, the global detectors serve in the triggering system and characterize timing, vertex position, and multiplicity of events, as well as the orientation of the reaction plane and centrality. The configuration

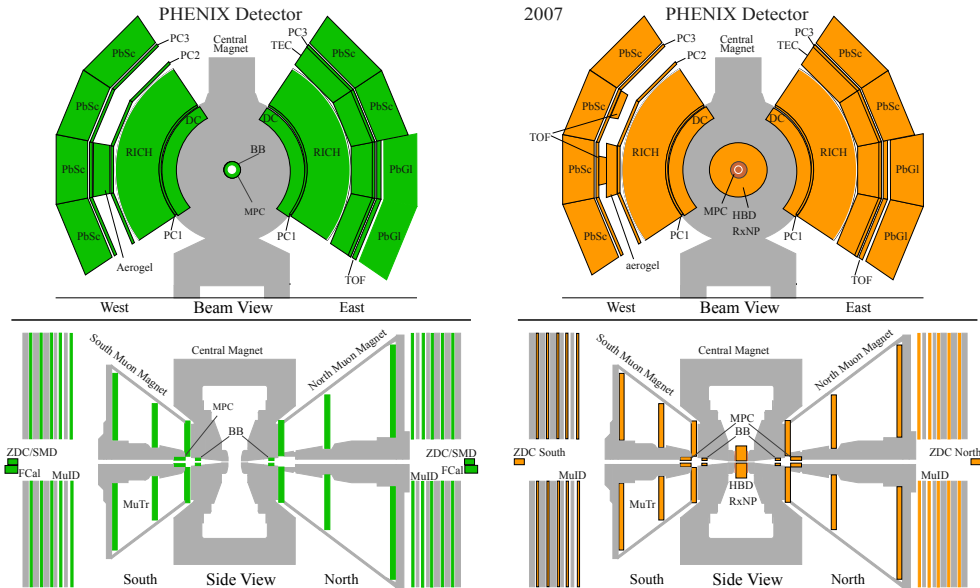


Figure 2.2: Configuration of the PHENIX detector for the 2006 (left) and 2007 (right) running periods.

of the subsystems within PHENIX for Runs 6 and 7 is shown in figure 2.2. The central arms cover a pseudorapidity range of $|\eta| < 0.35$ units and have an azimuthal coverage of about 90° each. They are designed for detecting photons, electrons, and charged hadrons with good position and momentum resolution.

The muon arms have full azimuthal coverage at forward rapidity and are used

for identification and tracking of dimuons and single muons from heavy quarkonia decays, especially J/ψ s. Their rapidity acceptance makes them particularly suitable for studying cold nuclear matter and low- x physics in asymmetric collision species such as $d+Au$. The north and south muon trackers each consist of three stations of multi-plane drift chambers enveloped in a radial magnetic field, followed by the muon identifiers, which are alternating panels of thick steel to absorb hadronic contamination and Iarocci streamer tubes for coarse position determination. The muon subsystems were not used in this analysis, so no further description will be provided here.

The acceptance of each subsystem is listed in table 2.2. The major subsystems used in this analysis will be described in the following sections.

Element	$\Delta\eta$	$\Delta\phi$	Purpose and Special Features
Central Magnet	± 0.35	360°	Up to 1.15 T·m
South Muon Magnet	-1.1 to -2.2	360°	0.75 T·m for $\eta = 2$
North Muon Magnet	1.1 to 2.4	360°	0.75 T·m for $\eta = 2$
Beam-beam (BBC)	$\pm(3.1 \text{ to } 3.9)$	360°	Start timing, fast vertex.
ZDC	$\pm 2 \text{ mrad}$	360°	Minimum bias trigger.
Drift chambers (DC)	± 0.35	$90^\circ \times 2$	Good p , m resolution, $\Delta m/m = 0.4\%$ at $m = 1 \text{ GeV}$.
Pad chambers (PC)	± 0.35	$90^\circ \times 2$	Pattern recognition, tracking in nonbend direction.
TEC	± 0.35	90°	Pattern recognition, dE/dx .
Hadron-blind (HBD)	lookup		
RICH	± 0.35	$90^\circ \times 2$	Electron identification.
ToF	± 0.35	45°	Good h^\pm ID, $\sigma < 100 \text{ ps}$.
PbSc EMCAL	± 0.35	$90^\circ + 45^\circ$	γ and e^\pm detection.
PbGl EMCAL	± 0.35	45°	Good e^\pm/π^\pm separation at $p > 1$ ($p < 1$) GeV/c by EM shower (ToF). K^\pm/π^\pm separation up to $1 \text{ GeV}/c$ by ToF.
μ tracker (south)	-1.15 to 2.25	360°	Tracking for muons.
μ tracker (north)	1.15 to 2.44	360°	Tracking for muons.
μ identifier (south)	-1.15 to -2.25	360°	Steel absorbers and Iarocci tubes
μ identifier (north)	1.15 to 2.44	360°	for μ^\pm/h^\pm separation.

Table 2.2: Basic coverage and description of the PHENIX subsystems that were installed for at least portions of Run 6 and 7. Updated from [9].

2.3 Triggering and data acquisition

The PHENIX data acquisition (DAQ) system [18, 19] is one of its most impressive features. In terms of data throughput capabilities, it has maintained a notable status as the fastest data acquisition of any experiment at RHIC, and is likely to be the fastest of any high-energy collider experiment prior to the startup of the LHC. In many physics analyses, this high-rate capability has compensated for PHENIX’s lack of full geometric acceptance.

In addition to the extremely fast DAQ, PHENIX has a two-level triggering/filtering system with the capability to reject empty bunch crossings and “uninteresting” events. The electronics in the PHENIX DAQ/trigger system are synchronized to the RHIC master clock (~ 10 MHz) and have the ability to select and process event data within about 100 ns, the timescale of one bunch crossing. The layout of the DAQ system is

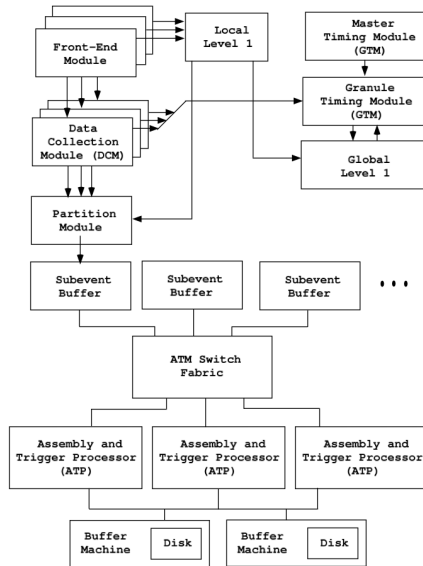


Figure 2.3: Schematic layout of the DAQ system, showing the interplay between the FEMs, the timing system, the DCMs, the event builder, and the data buffers. Upon receipt of an accept signal from the Level 1 trigger, the data flow from the FEMs continues through the DCMs to the event builder nodes in a highly distributed process. The PHENIX Run Control system integrates the components of the DAQ front end and orchestrates their operation.

shown in figure 2.3. Schematically, the data flow proceeds from raw detector subsystem signals to the front end electronics (FEE) modules, where they are processed as analog signals. The signals are fanned to the Level 1 trigger before being fully digitized to save time, and if the trigger accepts the event, the signals are digitized and sent

via fiber to an array of data collection modules (DCMs). The signals are processed in parallel groups called granules, which involves error checking, data compression, and reformatting. The processed streams are sent, again in parallel, to the event builder system, which assembles the granules and serves as the framework for a level-2 software trigger/filter system, which can be implemented for the benefit of particular physics analyses.

The assembled events are checked for quality by the online monitoring system, and buffered in high-capacity disks until they are archived to long-term tape storage at the RHIC computing facility, where the data can undergo production into a properly reconstructed and calibrated data set for physics analysis.

2.4 Global event characterization

Experimentally, the most fundamental properties of heavy ion collisions are the timing, position within the detector, reaction plane orientation, and centrality. The latter parameter is a statistical categorization used as a proxy for the impact parameter. The beam-beam counter [23] and zero-degree calorimeter [12] serve the critical roles of measuring these event properties, in addition to their roles in event counting and minimum bias triggering.

2.4.1 BBC and ZDC

Both the BBC and ZDC consist of separate north and south components fully surrounding the beampipe and provide position, multiplicity, and timing information that is redundant yet complementary, since they measure different types of particles over different rapidity ranges. The BBC detectors (figure 2.4) cover a range of $3.1 < |\eta| < 3.9$ while the ZDCs are positioned 18 m from the interaction point at a very small polar angle (hence the name). The BBC is designed to count and time charged particles, while the ZDC is measures collision spectators (primarily neutrons) which have not been swept

away from the beam by the DX steering magnets. Until the 2004 run, information from both subsystems was used to determine centrality, but since that time it was decided to use the BBC only since essentially equivalent precision can be obtained without the use of the ZDC. The north and south BBC each reside 144 cm from the interaction

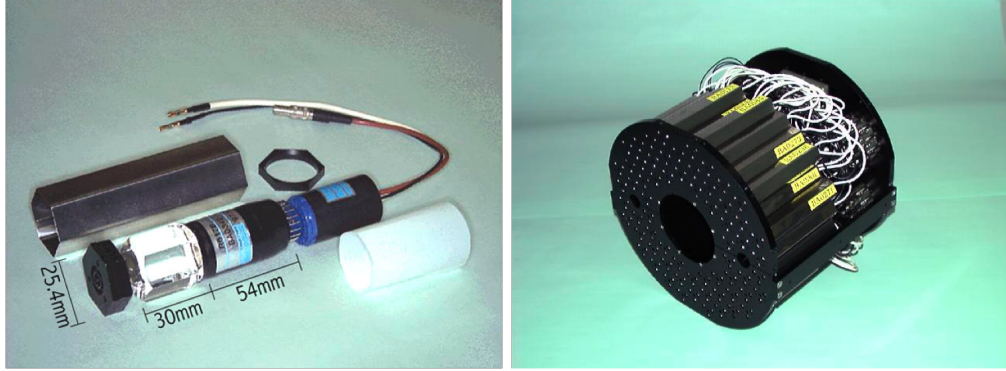


Figure 2.4: The beam-beam counter consists of 64 PMTs with quartz radiators in a honeycomb configuration.

point and consist of an array of 64 3 cm quartz Cherenkov radiators with mesh-dynode photomultiplier tube readout. This design has successfully met the stringent design requirements of handling multiplicities ranging into the thousands for central Au + Au collisions in the midst of an environment with high radiation and a 0.3 T magnetic field. In addition, the BBCs are mounted in a tightly confined region and require air cooling to maintain a suitable operating temperature for the readout electronics.

The BBC has an exceptional single-element timing resolution of 52 ± 4 ps. The time for all elements receiving hits is averaged to give T_N and T_S , which are used to establish the collision time for time-of-flight and other particle identification measurements. Given that $\beta = 1$ and $L = 144.35$ cm, the start time is defined as

$$T_0 = \frac{T_S + T_N - 2L/c}{2} \quad (2.1)$$

while the z-vertex of the collision is calculated as

$$z_{BBC} = c \frac{T_S - T_N}{2}. \quad (2.2)$$

The BBC sends the vertex information to the Level 1 trigger, which requires that the collision take place within a range of ± 30 cm from the center of the interaction region, and that both N and S BBCs register a hit in at least one phototube.

The reaction plane angle, Ψ , is defined by the direction of the impact parameter vector and can be inferred from measured by the BBC charge distribution. It is advantageous to measure the reaction plane in a rapidity range that is separated as far as possible from the region under study to avoid contamination from other sources of azimuthal anisotropy such as jets. Thus the BBC provides an important reference for elliptic flow measurements in the central arms. The n^{th} harmonic of the angular particle distribution is determined from the BBCs by using the ADC counts and the angle ϕ summed over the BBC elements:

$$\tan n\Psi = \frac{\sum_i^{64} ADC_i \sin n\phi_i}{\sum_i^{64} ADC_i \cos n\phi_i} \quad (2.3)$$

2.5 Central Arm Spectrometers

The full central arm acceptance is covered by drift chambers and pad chambers used to track charged particles, with the addition of a ring-imaging cherenkov detector for identifying electrons and time-of-flight (TOF) detectors for distinguishing pions, kaons, and protons. The outermost subsystem is the electromagnetic calorimeter (EM-Cal) which is positioned at 5 m from the beampipe. Although the azimuthal coverage is 90° for each arm, they are not positioned symmetrically in ϕ ; instead, they are rotated upwards by about 5° each, which improves the geometric acceptance for particle pairs at right angles.

2.5.1 Central Arm Magnets

The central arm magnet system [26] is used for momentum determination of charged particles and consists of separate outer and inner cylindrical copper coils embedded in iron yokes. The coils are positioned to provide a uniform field concentrated in the region surrounding the drift chambers and can be operated in constructive or opposite polarities. When the inner magnet polarity is reversed, the field closest to the beampipe is effectively canceled, which is necessary for the operation of the hadron-blind detector used in Run 7. The field configurations used in Runs 6 and 7 are shown in figure 2.5. In the same-polarity configuration, the central magnets produce an axial

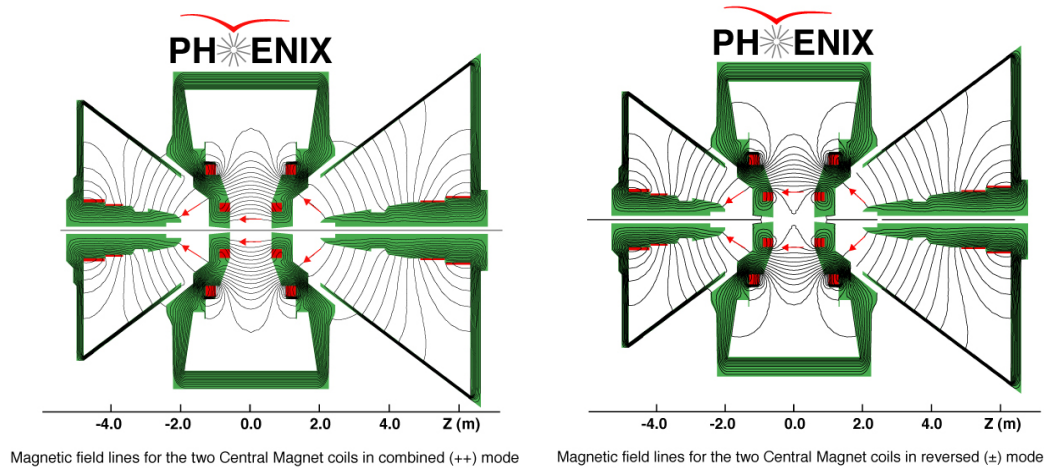


Figure 2.5: Central arm magnetic field configurations as viewed from the side. Left: the “++” configuration, used in Run 6 (double-check). Right: “+-” configuration, used for most of Run 7. The red boxes represent the outer and inner coils.

field of approximately 0.5 T within a 1 m radial region of the beam, corresponding to a $\int B \cdot dl$ of $\sim 0.8 T \cdot m$. The field drops rapidly to less than $0.01 T \cdot m$ outside the drift chamber (a design requirement) to minimize smearing of light rings from low momentum electrons in the RICH. The field strength was chosen to be sufficient to resolve momenta beyond 10 GeV, but weak enough to allow charged particles to maintain trajectories into the drift chamber down to $\sim 150 - 200 \text{ MeV}/c$ before curling up in the field.

2.5.2 Electromagnetic Calorimeters

The lead-scintillator (PbSc) and lead-glass (PbGl) calorimeter subsystems are one of the strongest features of the PHENIX experimental program. They provide excellent position and energy resolution for photons and electrons, and to a lesser extent charged and neutral hadrons. In addition, the timing resolution is adequate to identify pions, kaons, and protons with transverse momenta up to about 2-2.5 GeV/c. The energy resolution of the PbSc and PbGl were measured in test beams to be $8.1\%/\sqrt{E} \oplus 2.1\%$ and $5.9\%/\sqrt{E} \oplus 0.8\%$, while the timing resolutions are 100 ps and 200-400 ps, respectively.

Both calorimeter types exploit the principle of electromagnetic showering, which involves chained combinations of photon and electron production via two processes. The first is bremsstrahlung by energetic electrons interacting with nuclei in a (typically high-Z) material, and the second is e^+e^- pair production from a hard photon scattering against a softer photon that is typically associated with the EM field of a large nucleus. Since the photons and electrons of interest enter the calorimeter with at least several hundred MeV of energy, the two processes occur several times in succession, leading to an exponential growth in the number of photons and electrons with depth, until the energy of the particles approaches ionization energies.

This pattern produces a statistically well determined profile of the shower. The shower shape can be (and is) used to distinguish photons from electrons, as well as reject hadrons, which are most likely to deposit a relatively small amount of energy by ionizing atoms within the calorimeter material. The fine segmentation of the calorimeter additionally allows position resolutions on the order of 2-10 mm, depending on energy.

The EMCal is divided into 8 segments covering equal azimuthal areas. Four PbSc sectors cover the west arm, with two more on the upper half of the east arm, while two PbGl sectors are installed in the lower half. Although the detection principles differ between the two subsystems, the fundamental element of both subsystems is a single-

channel tower, shown in figure 2.6. Each PbSc (PbGl) sector contains 36×72 (48×96)

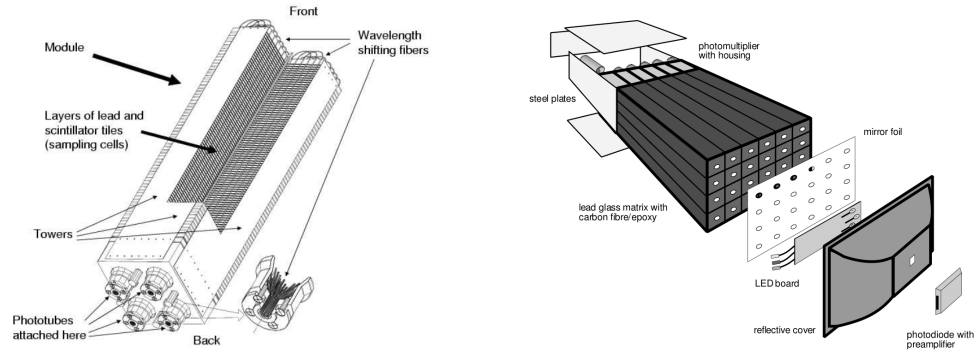


Figure 2.6: Elements of the two EMCal subsystems. Left: PbSc module containing four towers. Right: PbGl supermodule containing 24 towers.

towers, for a total count of 24,768 individual channels.

Each PbSc tower is constructed from alternating tiles of lead and plastic scintillator material stacked in a shashlik (Russian: skewer) configuration. There are 66 such Pb-scintillator sampling cells, each 0.56 cm thick, stacked in a single tower. Each tower is optically isolated from its neighbors with an external Aluminum plating. The towers have an active depth of 37.5 cm, corresponding to 18 radiation lengths, and present a square lateral segmentation of slightly over 5.5 cm on a side. The plastic tiles are Polystyrene containing an organic scintillator (POPOP) and the fluorescent additive p-Terphenyl, which leads to a large light yield (~ 12500 photons/GeV/tower). The scintillation light is read out through 36 wavelength-shifting fibers to a photomultiplier tube. Towers are grouped in 2×2 modules, which are further grouped into 3×3 module units called supermodules that are read out by a single front-end electronics unit.

The PbGl calorimeter towers are monolithic 4 cm x 4 cm x 40 cm glass blocks containing 51% PbO which are individually wrapped in aluminized mylar for light isolation and bundled into 6×4 tower supermodules. The finer segmentation corresponds to improved position and energy resolution compared to the PbSc, but the timing resolution is larger due to complications arising from hadronic response. The dense glass

serves as both an absorber (14.3 radiation lengths) and a Cherenkov radiator ($n = 1.65$) whose light is read out by photomultiplier tubes.

Photons are reconstructed in the EMCal as clusters of towers. The size of a shower in the calorimeter is parametrized by the Moliere radius, which defines a cylinder containing 90% of the shower energy. Empirically, $R_M = 0.0265X_0(Z + 1.2)$, which corresponds to shower sizes of 3-4 cm in the PbSc and PbGl. This means that showers typically span several towers (towers are only optically isolated for the low-energy scintillation or Cherenkov light read out by the PMTs; shower constituents are not reflected). The clusters are reconstructed by offline software and correct for effects such as incidence angle and energy dependence.

2.5.3 Drift chambers

The east and west drift chambers (DC) [11] are multiwire proportional chambers forming the core of the PHENIX central arm tracking system, and have proven to be capable in providing precise tracking information for charged particles even within the high occupancy environment of Au+Au collisions. Apart from the running period including the hadron-blind detector, the drift chambers were the innermost detectors in Runs 6 and 7, enveloping a radial distance of roughly 2-2.5 m and extending 1.8 m in z . They consist of a total of 6500 anode wires immersed in a 50/50 Ar-ethane drift gas mixture and separated by potential wires as well as gate and back wires to shape the field for optimum resolution. A photo of one DC panel is shown in figure 2.7. The DCs are each azimuthally segmented into 20 equal 4.5° sectors, sometimes called keystones, which contain six radial multiplane wire groupings, or modules. A side- and top-view schematic of one keystone is shown on the right hand side of figure 2.7. The X modules contain wires oriented parallel to the beamline for r - ϕ tracking, while the U and V modules are angled at $\sim 6^\circ$ in a stereo configuration to provide out-of-bend position information along the z coordinate. This angling of the U and V modules

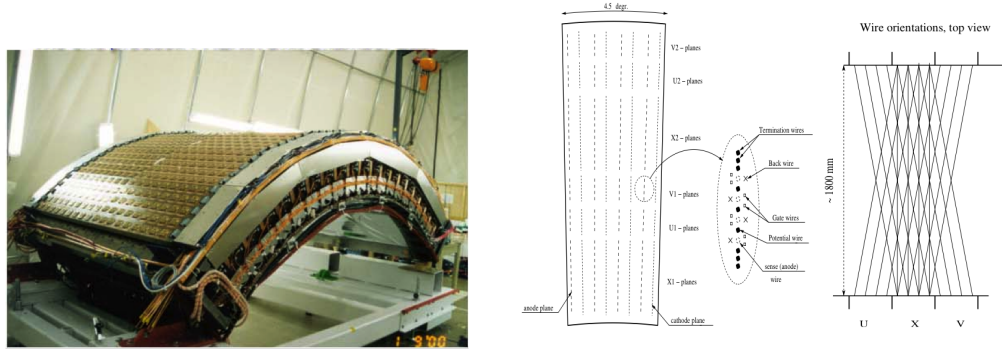


Figure 2.7: Left: a drift chamber panel showing the titanium frame enclosed in mylar front and back windows, and the segmentation into keystones. Right: side and top view of the wire layout within one keystone, schematically showing the 40 wire planes (12 for each X plane, 4 for each U, V plane.)

causes the wires to cross into adjacent sectors. The drift spacing is 2 - 2.5 cm in the azimuthal direction. Although not shown in the figure, the wires are bisected at $z = 0$ and electrically isolated with a $100 \mu\text{m}$ thick kapton support, and each half is read out separately, doubling the total channel count to 13000.

The reconstruction efficiency is better than 99% due to the low ambiguity provided by the precise manipulation of the electric field, the redundancy of the wire planes, and the fine spatial segmentation of the anode and sense wires. The r - ϕ single-wire resolution is $150 \mu\text{m}$, while the z spatial resolution is considerably larger at 2 mm. In practice, the tracking resolution can be improved by including three-dimensional position from the pad chambers, described next.

2.5.4 Pad chambers

The pad chambers (PCs) [10, 59] are multiwire proportional chambers with a single wire plane positioned between two cathode planes. One plane serves as a read-out via copper pixels grouped into pads. In high-multiplicity collisions, the position information from the drift chambers alone contains combinatorial ambiguities in the pattern recognition. The pad chambers provide a nonprojective three-dimensional po-

sition coordinate which can significantly improve the tracking accuracy when used in conjunction with the other central arm detectors. The PC layout (figure 2.8) consists

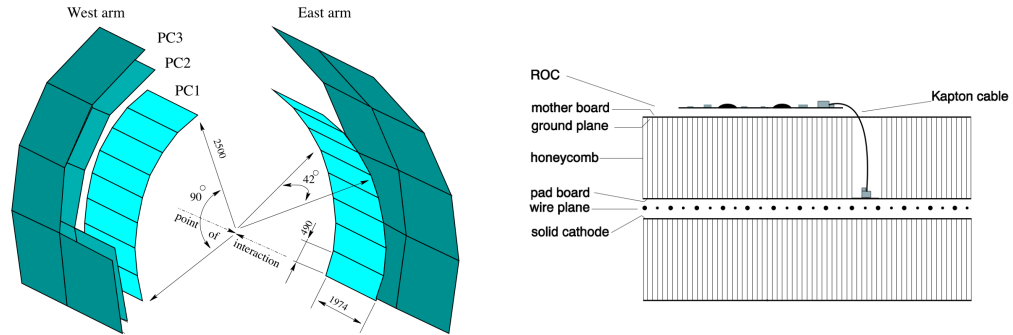


Figure 2.8: Left: Layout of PC subsystems with several PC panels and all other detectors removed for clarity. Figure from [59]. Right: cross-section of a pad chamber panel.

of three separate radial panels, although the middle panel, PC2, is only present in the west arm. PC1 is the innermost chamber and provides the z coordinate for particles exiting the DC before they enter the RICH. This provides critical information in reconstructing the momentum vector in the pattern recognition process. The PC3 (and PC2) can serve the important role of aiding in rejection of random background from decays and conversions when a minimum proximity cut (a.k.a. a match) is required between the projected track position and the nearest PC cluster. The readout pixel sizing

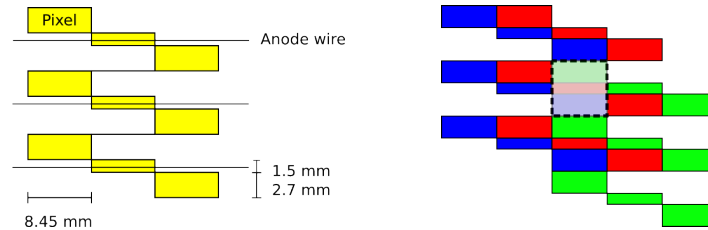


Figure 2.9: Left: an individual readout pad consists of nine pixels ganged together in a staggered configuration. Dimensions are shown for PC1; the outer PCs maintain comparable angular resolution with larger pixel sizes. Right: pads are arranged in an interlocking pattern such that three vertically adjacent pixels form a cell, which serves as the fundamental component of a PC cluster. Two of three pads within a cell must record a hit in order for the cell to participate in a cluster.

was chosen to be large enough to provide an optimum balance of high reconstruction

efficiency and reliability, while maintaining a spatial resolution of a few mm. Because there are five separate PCs each covering the full central arm acceptance, minimizing the channel count is an important design consideration. To this end, a clever design using interlocking pads (figure 2.9) was developed so that the readout from adjacent pads is grouped into geometrically contiguous 3-pixel cells. In PC1, each cell is a square 8.4 mm on a side. This overlapping configuration provides a factor of three gain in the area that can be covered with the same number of channels versus using square pads of the cell's dimensions, and a factor of nine compared to using one channel per pixel. Even with this optimization, the high channel density leads to a channel count of 172,800 for the total PC system. The pad readout is discriminated to reduce the output to a binary state, and each cell requires two of its three pixels to register a hit in order to be considered for inclusion into a cluster. The offline clustering algorithm then combines cells into PC clusters, assigning a size and position. Large clusters may be split if they demonstrate indications of merging, or rejected if their size is unacceptably large.

2.5.5 Ring imaging Cherenkov detector

The RICH is a focusing threshold cherenkov detector designed to distinguish electrons from the more abundant pions and other charged hadrons produced in hadronic collisions. Cherenkov light is produced by any charged particle traversing a dielectric material when it has a superluminal speed $\beta > 1/n$, where n is the index of refraction. The dielectric material, also known as the radiator, emits light in the short visible and near UV range at a characteristic angle to the particle trajectory given by

$$\cos \theta_c = 1/\beta n \tag{2.4}$$

due to the coherent disturbance of the electric field in the medium by the particle. At a molecular level, the material is polarized as dipoles in the material are distorted or rotated by the fast charged particle, and each dipole emits a weak pulse of radiation

upon returning to its initial state. At particle speeds below c/n , such pulses interfere and do not survive at macroscopic distances, but above the threshold, a constructive pattern develops in a manner analogous to acoustic Mach cones.

In principle, it is possible for a cherenkov detector to determine the velocity of a particle via equation 2.4, but a threshold cherenkov detector simply determines whether or not a particle carries a velocity large enough to produce cherenkov light by measuring the amount of light at the expected position. In conjunction with an independent momentum measurement, threshold Cherenkov detectors are thus used for particle identification by distinguishing particles with velocities above and below the threshold.

The threshold condition, $\beta > 1/n$, dictates that reducing n towards unity increases the threshold velocity. In PHENIX, the radiator gas is chosen in order to separate electrons and heavier charged particles over the broadest possible momentum range, which requires that n should be as small as possible in order to raise the threshold for pions, the next-lightest particles. The threshold is raised for electrons as well, but it is only a few tens of MeV, well below the minimum momentum that can be tracked in the magnetic field.

The RICH in each central arm contains a CO₂ radiator gas with $n = 1.000410$ ($\gamma_{th} = 35$), so that electrons radiate above $p_{th} = m\gamma_{th}/n = 0.02$ GeV/ c , while pions radiate above 4.7 GeV/ c . CO₂ is chosen over ethane despite its lower light yield because the pion threshold is about 1 GeV higher. The gas volume is large, 40 m³ in each arm, to give a long path length and thus an adequate light yield for high efficiency.

The RICH uses a focusing design, in which a spherical mirror reflects the light emitted along the full track to a PMT array, and the geometry of the mirror collects all light from a track into a ring whose radius is independent of the emission position along the track. This design could be contrasted with a proximity-focusing RICH, in which light from a thinner, high light-yield radiator volume is collected in a ring whose

radius depends on the particle velocity. To minimize conversions within the RICH, the

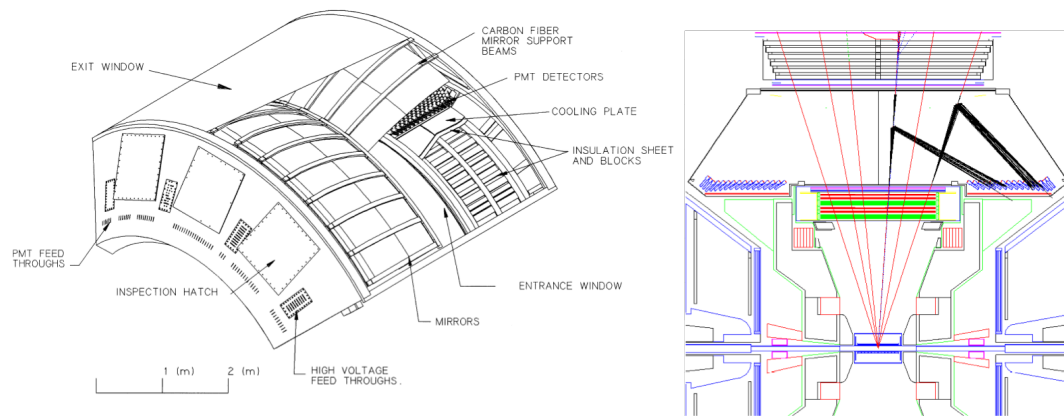


Figure 2.10: Left: outer perspective of the RICH detector. Right: cutaway drawing showing cherenkov light rays being reflected into the PMT array by the spherical mirror, which is omitted for clarity.

materials and radiator gas have been designed to be extremely thin and are less than 2% of a radiation length in total. The light is reflected away from the active volume as shown in figure 2.10, where the light ring can be reconstructed from information collected by the 2560 PMTs. Typical ring sizes are about 12 cm.

In this analysis, the RICH is not used specifically to identify electrons, but rather to reject particles that have deposited light below $4.7 \text{ GeV}/c$ in the RICH, which are assumed to be background electrons from conversions and decays contaminating the charged hadron sample. The criterion that no PMTs record a hit is used to veto electrons.

2.5.6 Tracking in the central arms

Tracking and reconstruction of momentum in the central arms requires integration of information from many of the subsystems described in this chapter. The process is described in detail in [37] and [60], but will be outlined here.

DC track reconstruction The track reconstruction process begins with a

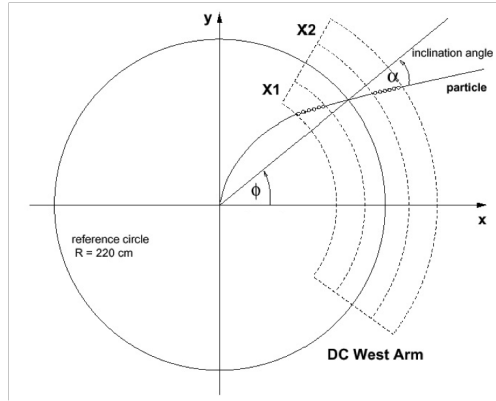


Figure 2.11: Tracking in the r - ϕ plane in the drift chamber. Track candidates are created from hit positions in the 40 radial wire planes and PC1 hits. Because of the nonzero field inside the DC, the particle trajectory is not perfectly straight, but the bend angle is less than 1° so a linear fit to the hits provides sufficient accuracy. α is defined at R_{DC} between this fit line and the line defined by ϕ .

segment containing a BBC z-vertex, DC wire hits, and a PC1 hit, as shown in figure 2.11. In the DC, tracks are reconstructed using a combinatorial Hough transform (CHT), which is an optimized version of a pattern recognition technique originally developed for identifying tracks in bubble chamber photos.

The principle of a Hough transform can be understood with a simple example problem, where the objective is to identify a line from a set of points distributed in the x - y plane. Each point (x_i, y_i) can be transformed to a line in parameter space, also known as feature space. The slope and y-intercept were used as the parameters in the original implementation, but due to the singularity of m for vertical lines, a polar parametrization of the line is preferred: $r(\theta) = x_i \cos \theta + y_i \sin \theta$. Thus a unique sinusoidal curve corresponds to each point if we require $0 \leq \theta < \pi$. Every point on the curve corresponds to a line in the x - y plane passing through (x_i, y_i) .

If a set of points is colinear, i.e. commonly constrained by $y_i = mx_i + b$, then the parametrization is also constrained to be $r(\theta) = x_i \cos \theta + (mx_i + b) \sin \theta$ and there is a point of intersection for the whole family of $r(\theta)$ curves. This is the point where $\cos \theta + m \sin \theta = 0$. If one were to bin each point in r - θ space, a peak would develop at this intersection, uniquely identifying the line.

A combinatorial Hough transform is similar in spirit to this example, but uses pairs of points instead, which reduces the computational overhead and provides more distinct peaks, reducing the number of “ghosts” or spurious tracks. The CHT is used

to reconstruct tracks in the r - ϕ plane, and PC and UV information is then combined with the results to carry out a separate tracking procedure in r - z . In this implementation of the CHT, all pairs of X1 and X2 DC hits are binned in a two-dimensional ϕ - α histogram. It is assumed that tracks are straight within the DC. Because of the hit redundancy provided by the X-planes (typically 6 hits in each module), the CHT provides prominent and distinguishable feature space peaks even in central Au+Au events. All peaks with amplitudes above a particular threshold are designated as track candidates, and after several iterations of hit association to PC1 and track purging, the tracks are reconstructed with high efficiencies and a ghost rate below 1%.

The momentum is reconstructed from the α inclination angle imparted by the magnetic field. Although the momentum reconstruction process is described in detail in the following sections, it is useful to observe that, for tracks emitted perpendicular to the z -axis, the p_T and inclination are roughly related as

$$\alpha \approx \frac{K}{p_T} \quad (2.5)$$

where the effective integrated field K is about 85 mrad GeV/ c .

The track model The central magnets more closely resemble a Helmholtz coil design than that of a solenoid, and consequently the field pattern involves strong non-axial components which lead to a focusing effect resulting in a violation of equation 2.5. Due to the separation in z of the coils, the concentric geometry of the inner and outer coils, and the presence of saturated iron in the magnet poles, the field shape is very complex, particularly at larger $|z|$. Fortunately, the field is at least symmetric in ϕ , a feature which is exploited in the calculation of particle trajectories.

Figure 2.12 shows the projections of charged particle tracks and the associated observables. A traditional approach to tracking of charged particles involves following a particle through a known magnetic field by integrating its equations of motion. However,

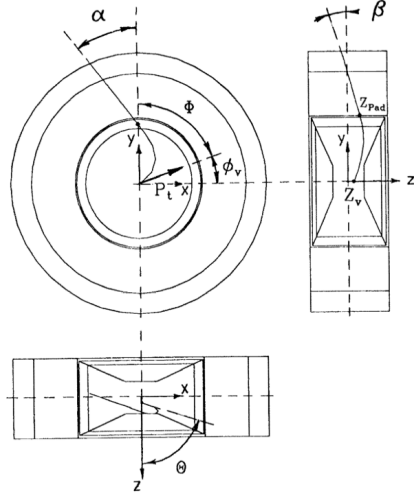


Figure 2.12: Track projections in the inner detectors. The z -coordinate at PC1, z_{pad} , is measured, in addition to three angles: α is the ϕ inclination angle between the DC track and a radial line at a reference position of $R_{DC} = 2.2$ m, the center of the DC. β lies in the plane defined by the z -axis and z_{pad} and is measured at R_{PC1} . Finally, $\phi_{DC} = \phi_v + \Phi$ is measured at R_{DC} .

From z_{pad} , α , β , and ϕ_{DC} , the kinematic parameters p_T , θ , z_v , and ϕ_v can be uniquely determined from the track model as described in the text.

the complexity of the central B-field prevents a precise analytic parametrization that can be used to calculate trajectories, so an alternative procedure has been devised [37].

The method involves conducting a full GEANT-based simulation to traverse charged particles (specifically e^\pm , π^\pm , K^\pm , p , \bar{p}) through the detector acceptance, which includes detailed numerical field maps generated from readings of Hall probes positioned throughout the central region and a full mock-up of the detector material and geometry to account for energy loss effects. The simulation is run for each particle type using a grid of possible initial values of p_T , ϕ , z -vertex position z_v , and polar angle θ . Thus a unique mapping is generated in the simulation between the measured positions and angles shown in figure 2.12, namely (z_{pad} , α , β , and ϕ_{DC}) and the basic kinematic variables (p_T , θ , z_v , and ϕ_v). This mapping is encapsulated in a large lookup table that is referenced and interpolated in the reconstruction process, so in a sense the problem solved by the simulation is worked out in reverse during momentum reconstruction.

The grid-mapping technique is carried out with a fine enough parameter spacing that any error introduced by the interpolation is a factor of ten smaller than the physical resolution of the hit measurements. The method has the advantage of being faster than reconstruction techniques requiring integration, however the initial investment must of

course be made to calculate the field maps and simulations for all relevant detector and magnet configurations. The technique assumes that all tracks originate at $(x, y, z) = (0, 0, z_v)$, so that displaced vertices and finite beam dimensions are neglected.

Reconstruction and inter-detector association The momentum reconstruction process begins with the reconstructed DC/PC1 track segment. For each DC hit, the field integral is estimated from a polynomial interpolation in the track model lookup table grid, and a linear fit is obtained to the field integral and ϕ . The procedure is iterated a few times until a convergence is obtained. At this point a reliable ϕ and momentum value have been calculated, and these inputs are used along with another LUT interpolation to obtain the polar angle information. Finally, the radial coordinate is nailed down with a final LUT interpolation in conjunction with the calculated angular inputs. At the end of the process the path length of each track is known at the position of the outer detectors, which can be used in the association.

The association between detectors relies heavily on a track model object which is generated in offline software from each DC/PC1 track candidate. The tracks are projected outward based on the track model assumption that they are pions, and particle identification procedures are subsequently used to determine the probability that the particle is not a pion. If this probability is determined to be large enough, the updated projection is re-run in order to properly account for energy loss and detector response. A list of hit positions in the outer detectors is also stored as input. The candidate hits are stored for a specific ϕ - z window about the projection of the track object to the outer detectors. The width of the window is dependent on the resolution of the detector and the error of the track projection. Each outer detector is associated independently, and the basic criterion for the association algorithm is to associate the projected track with the hit in closest proximity within the window. Efficiencies for tracking association to the PCs were calculated by a 200 GeV Au+Au HIJING simulation using GEANT for

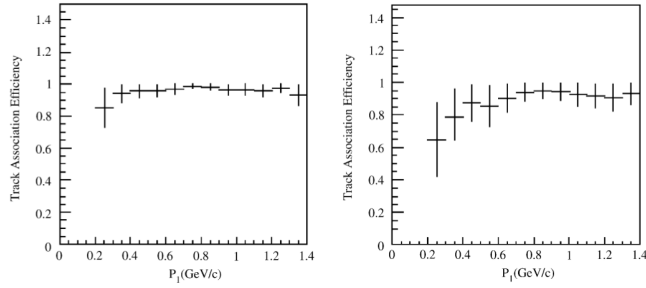


Figure 2.13: Track association efficiency as calculated from a GEANT simulation [60] between DC and PC1 (left) and between DC and PC3 (right).

detector response. Requiring that the original GEANT track be the dominant contributor to the DC hits (as opposed to background tracks from showering, conversion, decay, etc.), high association efficiencies were obtained as shown in figure 2.13.

2.6 The EMCal-RICH trigger

The EMCal-RICH trigger (ERT) is designed to select events where a large deposit of localized energy is identified in the EMCal, or where a strong electron-identification signal is found in the RICH. The former is of interest in this analysis. ERT triggering was employed in the data taking in Run 6 because of its high beam luminosities, whereas only the MB trigger was used in the 2007 Au+Au run.

The ERT trigger works by grouping EMCal towers (in software) into 2×2 groups called trigger tiles, whose summed energy is read out by an application-specific integrated circuit (ASIC). The tiles overlap so that the redundancy of the energy information controls for the effect of splitting energy between tiles. The configuration of the overlap is shown in figure 2.14. As shown in the figure, the tile energies are further combined into 4×4 units. In Run 6, a bit signaling the attainment of threshold energy of 2.1, 2.8, and 1.4 GeV for the $4 \times 4a$, b , and c tile sums was recorded. The decision as to whether the event fired the ERT trigger is based on the information from 12×12 tower supermodules, which are the finest unit recorded. Thus for each event a bit signaling

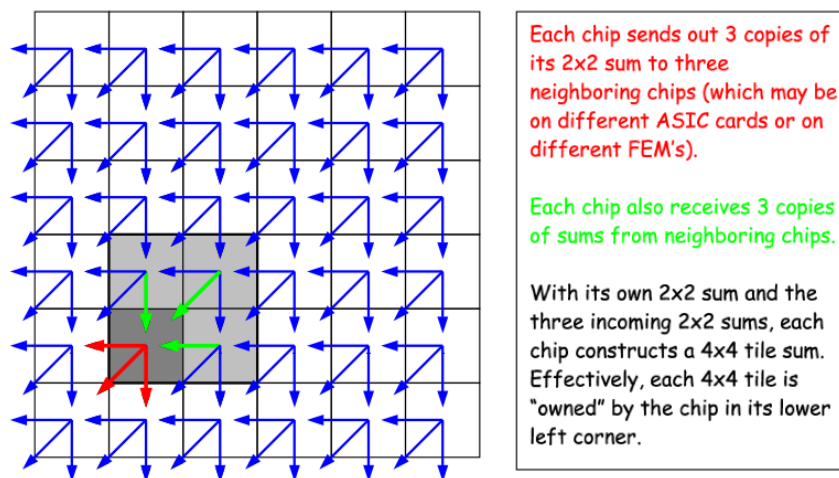


Figure 2.14: Layout of ERT tiles.

the attainment of each threshold energy was recorded as well as the location of the supermodule where it occurred. Run 6 suffered from a large number of noisy ERT tiles in the PbGl, which required the application of strict masks to the noisy channels. The hot tiles caused the lowest threshold ($4 \times 4c$) trigger to be live in only approximately half of the PbGl. In order to regain some of the lost efficiency, either the $4 \times 4a$ or $4 \times 4c$ was required, which recovered the majority of the live-triggered acceptance.

Chapter 3

Data analysis

This chapter describes the determination of event centrality in the PHENIX Run 7 dataset, as well as the procedures used to generate angular correlations between jet-induced π^0-h^\pm pairs, which involves identification of each type of particle, producing correlation functions, establishing and removing the non-jet background component, and applying corrections for detector acceptance, efficiency, and occupancy in order to obtain conditional jet pair yields. From these quantities a number of shape and yield observables can be calculated, and a comparison between the p+p reference and Au+Au can be made.

3.1 Centrality determination

Collision centrality has been determined through a number of different techniques in the history of the PHENIX experiment, most commonly through the “clock method” which involves an empirical correlation between the integrated charge measured in the beam-beam counters and the summed energy in the zero-degree calorimeters. However, the method employed for the Run 7 dataset used in this analysis is the “BBC only” method, which was decided after careful study demonstrated that the model-dependent parameters N_{part} or N_{coll} could be mapped to the BBC charge observables in a more precise way than with the clock method.

The BBC method relies on the assumption that the integrated charge measured

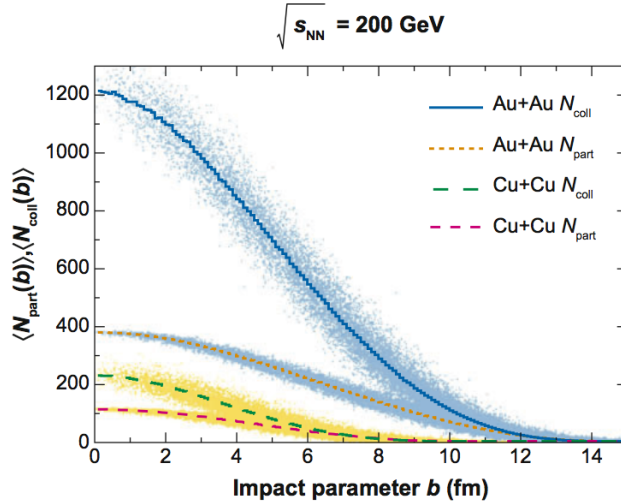


Figure 3.1: Glauber Monte Carlo calculation of N_{part} and N_{coll} as a function of impact parameter for Au+Au and Cu+Cu collisions at a center-of-mass energy of 200 GeV. The lines represent the mean values.

in the BBCs is linearly proportional to the number of collision participants. N_{part} is defined as the number of nucleons suffering at least one inelastic collision, while N_{coll} is the number of binary collisions per event suffered by these nucleons. These quantities are determined by a Glauber Monte Carlo (GMC) simulation [58]. A GMC simulation is used to connect the impact parameter b with these quantities, as shown in figure 3.1. Additionally, the probability for an event to have a given N_{part} or N_{coll} is given by these respective distributions, shown in figure 3.2. Note that because the GMC uses a Woods-Saxon nuclear density profile, which includes a diffuse tail, the geometry dictates that glancing collisions are far more common than low- b collisions.

The linear proportionality between BBC charge and collision multiplicity implies that each collision participant makes an equal contribution to the charge measured in the BBC tubes, one unit of charge per BBC hit on average. The number of BBC hits in each collision is expected to follow a negative binomial distribution (NBD). The NBD is similar to a Poisson distribution, but with a wider variance, and in fact converges to equivalence with a Poisson in the limit of a large number of trials. It is discussed further in appendix B. The linearity assumption mentioned earlier effectively states that the mean of the NBD $\mu \approx N_{\text{part}}$. Additionally, the assumption that the hits are uncorrelated to each other leads to a proportionality between NBD k parameter and

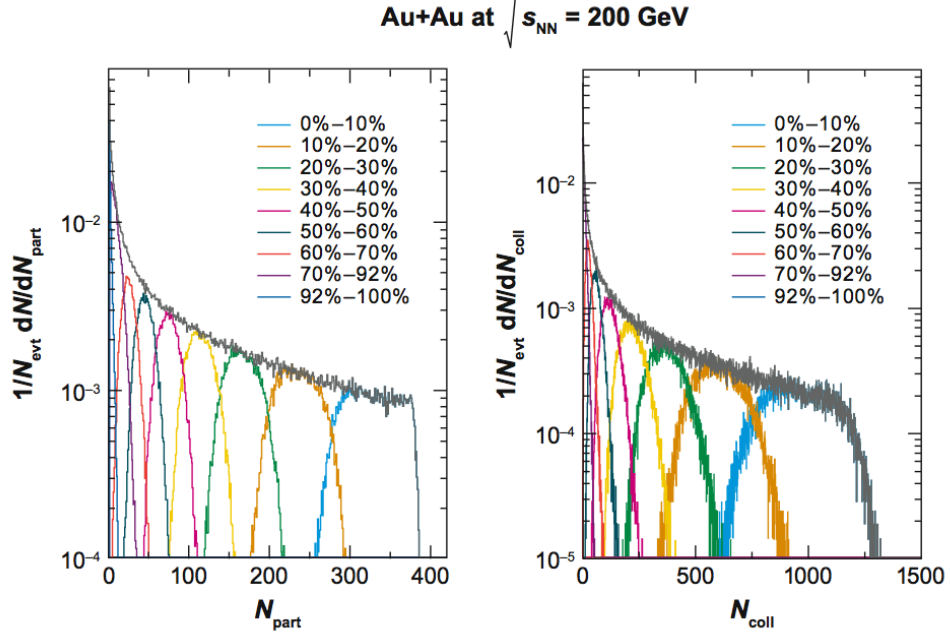


Figure 3.2: N_{part} and N_{coll} distributions from GMC.

N_{part} . The procedure to connect N_{part} ¹ to the number of BBC hits thus proceeds as follows:

- Using the assumptions made above, the NB probability is calculated in the scaled variables μN_{part} and $k N_{part}$ for each N_{part} value taken from a Glauber MC simulation, with the inclusion of a weighting factor $f_{Glauber}(N_{part})$ (see fig. 3.2) to account for the probability for each event to have the given N_{part} .
- The trigger efficiency correction factor $\frac{1}{\epsilon(N_{hit})}$ is taken into account.
- The probability for the BBC to observe N_{hits} in an event with N_{part} is thus given by

$$\frac{1}{\epsilon(N_{hit})} P(N_{hit}) = \sum_{N_{part}} f_{NB}(\mu N_{part}, k N_{part}) f_{Glauber}(N_{part}). \quad (3.1)$$

- This probability is fit directly to the N_{hit} data to extract the parameters μ and k .

¹ The procedure can apply to an N_{coll} parametrization as well.

- The BBC charge is binned in 1-percentile categories, such that each event corresponds to a particular centrality and N_{part} range.

3.2 Two-particle correlation framework

As discussed in section 1.5, two-particle azimuthal correlations are a powerful statistical technique used to study jet signals in hadronic and nuclear collisions. Although direct jet reconstruction algorithms have undergone significant recent progress, the large multiplicities of soft background particles have proven difficult to disentangle from the fragments of energetic particles on event-by-event basis, particularly in a detector with limited acceptance such as PHENIX.

A powerful alternative is offered by the angular correlation method, in which patterns from a very large number of events is examined. In this analysis, π^0-h^\pm pairs that are believed to be correlated through jet-related processes are extracted from a distribution containing not only the signal, but additional background correlations due to combinatoric pairing and soft physics.

The class of trigger particles (A) typically consists of high-momentum particles that are closely aligned with the jet axis. A partner particle may be present in the event at some other position and energy. Since leading-order QCD predicts back-to-back azimuthal jet production, the angle of the partner in reference to the trigger particle, $\Delta\phi = \phi^A - \phi^B$, is expected to peak at $\Delta\phi = 0$ and π . Other factors such as Fermi motion within the initial state hadrons and both initial- and final-state radiation lead to an additional smearing effect. Because of the central limit theorem, these combined effects lead to jet signals in $p+p$ collisions taking on a Gaussian shape, where the angular region opposite to the trigger, known as the away side, exhibits a slightly broader shape than that on the near side.

Because there can be a large imbalance in the fractional momenta between the partons involved in the hard scattering process, momentum conservation dictates that

the jet axes are not back-to-back in rapidity. Moreover, the limited PHENIX acceptance in η typically allows only an incomplete capture of the complete set of jet fragments, leading to a reduction in the number of away-side pairs relative to the near side.

3.2.1 Event mixing and background normalization

The effects of limited acceptance and dead or inefficient areas would significantly distort the pair distribution if it were not properly corrected. Pair acceptance and efficiency effects are accounted for by event mixing. A trigger particle is paired with partners from other events so that the pair distribution maps out precisely the ability of the detector to measure trigger-partner pairs. Event mixing is performed with a pool of events that are temporally close to the real event so that the performance of the detector is as similar as possible to its state during the real event. This distribution serves operationally as the denominator in equation A.1. The ratio of the same-event pair distribution to that of the mixed pairs thus allows a cancellation of pair-acceptance effects, leaving a distribution reflecting only physical correlations. This ratio, when normalized to account for the mixed-event multiplicity enhancement, is the experimentally-defined correlation function $C(\Delta\phi)$:

$$C(\Delta\phi) = \frac{\frac{d\langle n_{same}^{AB} \rangle}{d\Delta\phi}}{\frac{d\langle n_{mix}^{AB} \rangle}{d\Delta\phi}} \frac{\int \frac{d\langle n_{mix}^{AB} \rangle}{d\Delta\phi} d\Delta\phi}{\int \frac{d\langle n_{same}^{AB} \rangle}{d\Delta\phi} d\Delta\phi} \quad (3.2)$$

The lowercase n variables represent per-event pair counts, and the angle brackets denote an averaging of these pair multiplicities over many events within a centrality selection. In practice, the ratio of the two integrals is a weighting applied to the mixed-event distribution effectively equivalent to the inverse of the mixing depth, i.e. if each event was mixed with ten other events, the normalization factor would amount to 1/10. Thus, any excess in the ratio above unity can be interpreted as the presence of pairs resulting from physical correlations.

3.2.2 The two-source model and elliptic flow as a residual correlation

A fundamental problem centers around the disentanglement of AB pairs arising from jets and those that are not directly associated with jets. This problem is addressed in [66] and the following is based on the discussion therein. The simplest assumption is that correlations arise from two independent and separable sources: a jet component and a generically designated “background” component. Although single particles can be produced in principle from either a jet-related or a non-jet related process, background pairs can be formed from particles in which both are from different jets, neither is from a jet, or a jet particle is paired with a non-jet particle. With the jet-background distinction, the azimuthal distribution of pairs is

$$\frac{d\langle n_{same}^{AB} \rangle}{d\Delta\phi} = \frac{d\langle n_{jet}^{AB} \rangle}{d\Delta\phi} + \frac{d\langle n_{bg}^{AB} \rangle}{d\Delta\phi} \quad (3.3)$$

Under this decomposition, the jet signal can be extracted from the correlation function if both the shape and the relative contribution of the background are known. In the p_T ranges of the particles involved in this analysis, the primary quantifiable source of azimuthal anisotropy surviving in the background over a large sample of events is elliptic flow.

The distribution of single particles correlated through elliptic flow was introduced in equation 1.14. This type of correlation can be considered a “residual” correlation². A residual correlation can be defined for these purposes as an A-B correlation through some parameter such that one or more sub-ranges Q in the parameter can be identified where A and B are **uncorrelated**. Within each sub-range Q , the pair distribution factorizes and the correlation function is unity.

To calculate a residual correlation, it is necessary to sum or integrate over each of these subranges (which may be intervals in a continuous parameter or discrete steps). The quantities in the correlation function defined in equation A.1 are represented as

² See footnote in section 1.5.

$N^{A,B,AB}(Q)$, and Q can be treated as a random variable following a probability distribution $P(Q)$. For the continuous case,

$$\frac{1}{N_{evt}} \frac{d^3 N^A}{d^3 \mathbf{p}_A} = \int dQ P(Q) \frac{1}{N_{evt}} \frac{d^3 N^A(Q)}{d^3 \mathbf{p}_A} \quad (\text{same for } A \rightarrow B) \quad (3.4)$$

$$\frac{1}{N_{evt}} \frac{d^6 N^{AB}}{d^3 \mathbf{p}_A d^3 \mathbf{p}_B} = \int dQ P(Q) \frac{1}{N_{evt}} \frac{d^6 N^{AB}(Q)}{d^3 \mathbf{p}_A d^3 \mathbf{p}_B} \quad (3.5)$$

For the discrete case, the integrals would be replaced by summations in the expected way.

Moving to the specific case of elliptic flow at a fixed centrality, and ignoring any other sources of correlation for the moment, it can be seen that the reaction plane angle Φ_{RP} serves as the Q parameter, because the per-event single-particle angular distribution is determined by the reaction plane as given by equation 1.14: a cosine-modulated function whose normalization N_0 is given by the per-event count of particles divided by the full angular range, i.e.

$$\begin{aligned} \frac{1}{N_{evt}} \frac{dN^A(\Phi_{RP})}{d\phi_A} &= \frac{n^A}{2\pi} [1 + 2v_2^A \cos(2(\phi_A - \Phi_{RP}))] \quad (\text{same for } A \rightarrow B) \\ \frac{1}{N_{evt}} \frac{d^2 N^{AB}(\Phi_{RP})}{d\phi_A d\phi_B} &= \frac{n^A n^B}{(2\pi)^2} [1 + 2v_2^A \cos(2(\phi_A - \Phi_{RP}))] [1 + 2v_2^B \cos(2(\phi_B - \Phi_{RP}))] \end{aligned}$$

Using equation 3.6 in equation 3.5 and integrating over $dQ = d\Phi_{RP}$ with the isotropic reaction plane distribution $P(\Phi_{RP}) = 1/2\pi$ gives

$$\frac{1}{N_{evt}} \frac{d^2 N^{AB}}{d\phi_A d\phi_B} = \frac{n^A n^B}{(2\pi)^2} [1 + 2v_2^A v_2^B \cos(2\Delta\phi)]. \quad (3.7)$$

This result is remarkably simple in that it expresses the same functional form for the relative-angle distribution of pairs as for single particles. When placed into equation A.6, this gives

$$C_{\text{flow}}(\Delta\phi) = 1 + 2v_2^A v_2^B \cos(2\Delta\phi). \quad (3.8)$$

Other potential sources of correlation have been proposed in the literature, including ambiguously-labeled “non-flow effects” [68], or perhaps more specifically “minijets” [71] or “clusters” [70]. However, these phenomena, if physically present, remain elusive as

to their shape or level of contribution to angular correlations. As discussed in the introduction, the event anisotropy due to elliptic flow has been measured to be quite strong, and imparts a harmonic modulation to the combinatorically paired background. The two-source model thus suggests an application of the following division into flow and jet components:

$$C(\Delta\phi) = J(\Delta\phi) + b_0 (1 + 2\langle v_2^A v_2^B \rangle \cos(2\Delta\phi)). \quad (3.9)$$

The quadrupole anisotropy coefficients $v_2^{\{A,B\}}$ are taken as inputs from independent measurements of type A and B particles. As noted in section 1.4, higher order terms of the anisotropy expansion are smaller and often neglected. In Eq 3.9, the approximation is made that the background pair anisotropy is equivalent to the product of the single-particle anisotropy coefficients:

$$\langle v_2^A v_2^B \rangle = \langle v_2^A \rangle \langle v_2^B \rangle. \quad (3.10)$$

Given the validity of equation 3.9 and the factorization of the pair flow in 3.10, the only remaining problem is establishing the relative contribution of the background level as parametrized by b_0 . By combining the relations given in equations 3.2, 3.3, and 3.9 and integrating over $\Delta\phi$, the background level is related to the per-event pair multiplicities as

$$b_0 = \frac{\langle n_{bg}^{AB} \rangle}{\langle n_{mix}^{AB} \rangle}. \quad (3.11)$$

Two different approaches have been employed in the determination of b_0 , each with its own physical assumptions: (a) the zero-yield-at-minimum (ZYAM) method [14, 21], and (b) the absolute background subtraction (ABS) method [66].

3.2.3 The ZYAM method

In the ZYAM method, b_0 is set such that some region of the background-subtracted jet function vanishes. In practice, this amounts to scaling the background term so that

it contacts a well-defined point associated with the correlation function. There are a handful of different ZYAM implementations in conventional use, which differ primarily in how the minimum of $J(\Delta\phi)$ in equation 3.9 is defined. As the ZYAM method was being developed, the single lowest point was sometimes used to designate the minimum, but this definition suffers the obvious weakness of susceptibility to statistical fluctuations in the angular region near the minimum. Any downward scatter on a point near the minimum can unnaturally lower the minimum point, thus causing a potential over-estimation of the background-subtracted jet function. An improvement over the use of a single minimum point involves establishing the zero-yield point in a bin-averaged region at right angles to the jet axes, as done in [14]. This definition suffers a similar bias due to statistical fluctuations as the single-bin definition of the minimum, but at a reduced level.

A more rigorous approach involves designating the minimum at the low point of a curve which is fit to the data. Although not immune from the effects of statistical fluctuations, this method generally suffers a smaller bias than the direct determination of a minimum from a small number of points. However, it requires the assumption of a specific functional form for the fit curve, and naturally requires that a satisfactory fit to $C(\Delta\phi)$ can be obtained.

An additional pitfall associated with the ZYAM method arises in the case where one or both of the jet peaks are wide enough that a non-negligible tail component persists into the minimum region. In such a case, the minimum point may reside well above the true background level. If the ZYAM condition is strictly enforced, the jet yield can become significantly underestimated. If the fitting method is used in this case, it must be decided (and clearly documented) whether b_0 is chosen such that the background level truly contacts the minimum point on the fit curve, or whether a gap is allowed to account for what may be a signal yield in the tail region.

The ZYAM method has generally been considered a robust technique for cases

where statistics are adequate to obtain high-quality fits to $C(\Delta\phi)$ and where the near- and away-side peaks are well distinguished. Thus the ZYAM method is used for the $p+p$ reference data in this analysis. Additionally, the alternative ABS technique requires a variation in N_{part} or N_{coll} as described below in order to calculate the background, and such a parametrization has not yet been demonstrated to be possible in $p+p$.

3.2.4 The ABS method

The absolute background subtraction (ABS) method uses the assumptions that (a) the multiplicity of background pairs can be calculated directly from combinatorics, and that (b) the hard QCD processes produce fairly strong angular correlations between the jet-induced particles. The background particles are considered to be auto-correlated³ through event-wide effects such as hydrodynamic flow. Under these assumptions, the mean per-event background pair production rate is equivalent to the product of the mean single-particle production rates:

$$\langle n_{bg}^{AB} \rangle = \langle n^A \rangle \langle n^B \rangle. \quad (3.12)$$

Thus if the background is truly combinatorial in nature, the background level in $C(\Delta\phi)$ is

$$b_0^{ideal} = \frac{\langle n^A \rangle \langle n^B \rangle}{\langle n_{bg}^{AB} \rangle} \quad (3.13)$$

Thus, since $\langle n^A \rangle$ and $\langle n^B \rangle$ are directly measurable in the data, the background level can be calculated directly, if the mixed-event pair multiplicity can be used as a proxy for the true combinatoric background. However, the single-particle per-event multiplicities increase with N_{part} or N_{coll} as collisions become more central. This increase is shown schematically in figure 3.3 and again for real $Au+Au$ data in figure 3.4. When two distributions are not flat, the mean of their product is not generally equivalent to the

³ Here, the term ‘‘auto-correlation’’ refers to a common source of correlation between many particles, such as radial expansion or anisotropic flow, in contrast to a specific correlation source affecting a small number of particles, such as hard scattering and jet fragmentation.

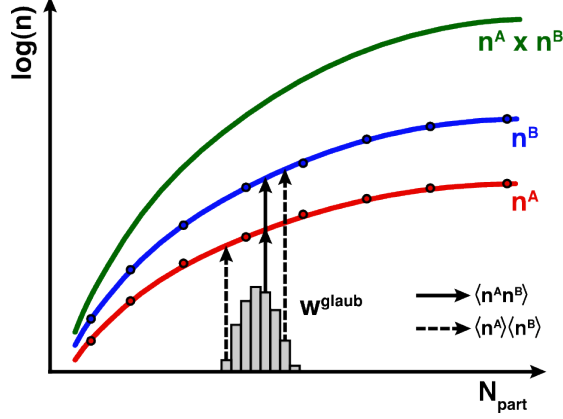


Figure 3.3: Cartoon from [66] of single-particle per-event yields versus N_{part} . The solid arrows represent true combinatoric background pair multiplicity, while dashed arrows represent the approximate background multiplicity obtained through event mixing within a finite centrality category. The difference between the two results is described by the residual multiplicity correction factor ξ .

product of their means. Because event mixing is done in centrality categories that span a finite range in N_{part} or N_{coll} , and $\langle n^A \rangle$ and $\langle n^B \rangle$ depend on these quantities, a multiplicity correlation arises. This residual multiplicity correlation, known as ξ , is a description of the degree to which the ratio in equation 3.13 deviates from unity, and is defined as

$$\xi = \frac{\langle n^A \rangle \langle n^B \rangle}{\langle n^A n^B \rangle}. \quad (3.14)$$

Since the single-particle multiplicities rise as collisions become more central, the mixed-

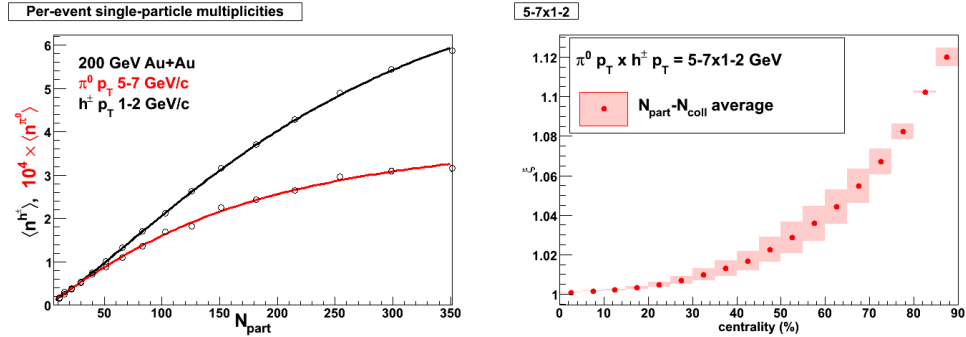


Figure 3.4: Left: per-event multiplicities of pi0's and charged hadrons. Right: ξ factor for 5% centrality bins.

event sample slightly overestimates the background estimate obtained as the simple product of single-particle yields, since it is more likely that higher-multiplicity events are combined than low-multiplicity events. Thus $\langle n_{\text{mix}}^{AB} \rangle > \langle n_{\text{mix}}^{AB} \rangle = \langle n^A \rangle \langle n^B \rangle$, and b_0 is underestimated compared to b_0^{ideal} . It is straightforward to calculate this deviation,

and the residual multiplicity correction factor can be applied to restore the mixed-event sample as a usable proxy for the true background. Since b_0^{ideal} is underestimated by the use of mixed events, it is expected that the correction factor $\xi \geq 1$.

The actual calculation ξ requires that $\langle n^A \rangle$ and $meanb$ are available, as well as the probability $P(N)$ for an event to have a particular multiplicity (N_{part} or N_{coll}) within the centrality range allowed for event mixing. This probability is equivalent to $f_{Glauber}$ described in section 3.1, and shown, for example, as the peaked distributions in figure 3.2 or as $w^{Glauber}$ in figure 3.3. The residual multiplicity correction factor $\xi(N)$ is then calculable by the discrete versions of equations 3.4 and 3.5, using $Q = N_{part}$ or $N_{coll} \equiv N$. ξ serves as a measure of the residual correlation obtained by comparing pair multiplicities from events having the *same* N to that from events with *different* N :

$$\xi(N) = \frac{\sum_N P(N) \langle n^A n^B(N) \rangle}{\sum_N P(N) \langle n^A(N) \rangle \sum_N P(N) \langle n^B(N) \rangle} \quad (3.15)$$

As a simple example, consider a linear form for $\langle n^A \rangle$ and $\langle n^B \rangle$ that vanishes at $N = 0$:

$$\langle n^A \rangle = Na \quad (3.16)$$

$$\langle n^B \rangle = Nb \quad (3.17)$$

$$\langle n^A n^B \rangle = N^2 ab. \quad (3.18)$$

The slopes are independent of N and cancel in the ratio, leaving only the expectations of N and N^2 :

$$\xi(N) = \frac{\sum_N P(N) ab N^2}{\sum_N P(N) a N \sum_N P(N) b N} = \frac{\langle N^2 \rangle}{\langle N \rangle^2} \quad (3.19)$$

Since the variance of P is $\sigma^2 = \langle N^2 \rangle - \langle N \rangle^2$,

$$\xi(N) = 1 + \left(\frac{\sigma(N)}{\langle N \rangle} \right)^2. \quad (3.20)$$

Note that $\xi \geq 1$, and that the correction becomes more significant as the width of P grows relative to the mean. In the Gaussian regime where $\sigma \sim \sqrt{N}$, it is found

that $\xi \approx 1 + 1/N$, and the magnitude of the correction is small. Although the real data does not follow such a simple parametrization, the features observed here are qualitatively general. This is demonstrated by the example in figure 3.4, where the results of equation 3.14 have been shown for type $A = \pi^0$ and $B = h^\pm$ particles in real Au+Au data. It can be seen that ξ remains within 1% of unity for the 30% most central collisions, but rises sharply as the multiplicity drops, which corresponds to a rising degree of variation in multiplicity over a centrality bin. Quantitatively, event mixing provides a good approximation of the combinatorial background for central events, provided that the centrality binning is sufficiently narrow (here they are 5%). The pale boxes are bounded above and below by results from calculating with N_{part} and N_{coll} parametrizations, and the central point is the mean value. The difference between the two parametrizations is taken to be the sole source of systematic uncertainty in the background normalization, and its propagation into the final results will be described in a later section.

$\pi^0 p_T$ (GeV/c)	$\pi^0 - h^\pm \xi$ values, 0-20%				
	$h^\pm p_T$ (GeV/c)				
	0.5-1	1-2	2-3	3-5	5-7
4-5	1.001 \pm 0.004	1.003 \pm 0.005	1.003 \pm 0.004	1.002 \pm 0.004	1.005 \pm 0.004
5-7	1.000 \pm 0.004	1.002 \pm 0.005	1.002 \pm 0.004	1.001 \pm 0.004	1.004 \pm 0.004
7-9	1.001 \pm 0.004	1.003 \pm 0.004	1.003 \pm 0.004	1.001 \pm 0.004	1.004 \pm 0.004
9-12	1.000 \pm 0.004	1.002 \pm 0.005	1.002 \pm 0.004	1.001 \pm 0.004	1.003 \pm 0.004

Table 3.1: 0-20% ξ values.

$\pi^0 p_T$ (GeV/c)	$\pi^0 - h^\pm \xi$ values, 20-60%				
	$h^\pm p_T$ (GeV/c)				
	0.5-1	1-2	2-3	3-5	5-7
4-5	1.012 \pm 0.005	1.011 \pm 0.006	1.013 \pm 0.006	1.010 \pm 0.005	1.013 \pm 0.005
5-7	1.010 \pm 0.005	1.008 \pm 0.005	1.011 \pm 0.005	1.008 \pm 0.004	1.011 \pm 0.005
7-9	1.008 \pm 0.004	1.008 \pm 0.005	1.007 \pm 0.005	1.007 \pm 0.004	1.010 \pm 0.004
9-12	1.009 \pm 0.005	1.008 \pm 0.005	1.010 \pm 0.005	1.008 \pm 0.004	1.010 \pm 0.005

Table 3.2: 20-60% ξ values.

3.3 Event mixing

Event mixing is implemented by maintaining a buffer of events in memory that are in close temporal proximity to the event being processed. Events are always mixed within the same DAQ run in order to avoid calibration drifts, channel trips, or other hardware or electronics problems. Because the mixed-event background in $\Delta\phi$ is used as the reference for acceptance correction, it is important that its statistical uncertainty is very small compared to the same-event distribution. The mixing depth, or event buffer size, is varied according to the centrality of the event in order to optimize statistical precision versus computation time and memory usage. Very peripheral events require a greater mixing depth than central events to accumulate the same statistics in the pair distribution. In the p+p data, a uniform mixing depth of 20 events is used. In Au+Au, the mixing depth ranges from 20 events in the most central collisions to a maximum of 300 events at or above 65% centrality.

An example of the azimuthal distribution of π^0-h^\pm pairs is shown in figure 3.5 for two different trigger \times partner p_T bins. The mixed-event pair distribution, shown in black, captures the shape of the pair acceptance in the central arm spectrometers. It has been normalized by the mixing depth to represent the equivalent sample of events included in the same-event pair distribution. It is clear from the figure that the orientation of the two opposing 90° central arm spectrometers offers a highly nonuniform probability to obtain pairs vs. $\Delta\phi$: back-to-back pairs receive optimal acceptance, while right-angle coincidences are comparatively infrequent. It is evident in the figure that an adequate mixing depth is maintained in order to reduce the uncertainties within this statistically-deprived region.

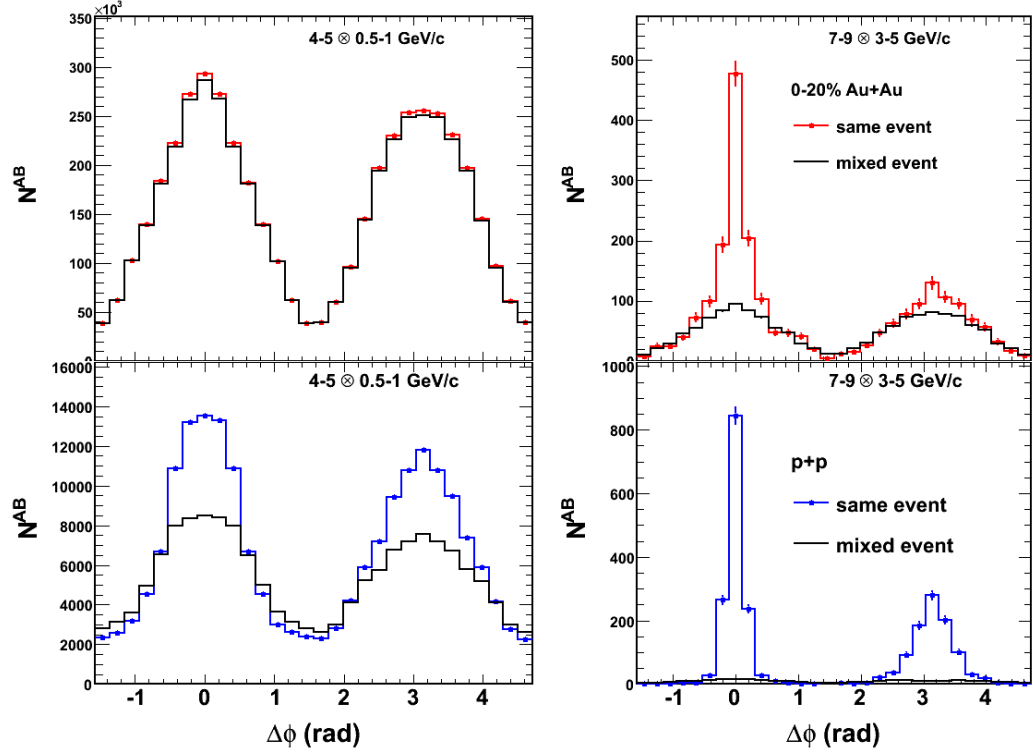


Figure 3.5: Same-event and mixed-event distributions for central Au+Au (top) and p+p (bottom). Two trigger \otimes partner p_T bins are shown as examples, demonstrating the large increase in the correlated signal to background ratio with increasing p_T .

3.4 Data quality

This section focuses on the quality assurance (QA) procedures applied to the Run 6 and Run 7 data.

3.4.1 Event selection

All events in the Au+Au data were required to satisfy the following two criteria

- Trigger requirement:

- * Each event must record a coincidence between the ERT trigger and BB-CLL1 in Run 6.

- * They must satisfy the minimum bias trigger requirement in Run 7, which is BBCLL1(>1 tube).
- The reconstructed BBC z-vertex must reside within ± 30 cm of the center of the interaction point.

3.4.2 DAQ runs and run QA

As described in chapter 2, the data is recorded in blocks called DAQ runs, or simply “runs” (lowercase “r”). The duration of each run typically ranges from a few minutes to an hour or more, and contains information associated with $\mathcal{O}(10^4 - 10^6)$ collisions, depending on a variety of running conditions. The raw data that is initially archived to tape in the PHENIX raw data format (PRDF) contains multitudes of low-level detector information that is used during the production process to calculate a recalibrated version of the data with more physically salient variables stored in data summary tape (DST) format.

Although DSTs are typically condensed by an order of magnitude relative to PRDFs, the full minimum-bias data volumes for entire Runs have remained too large to be maintained in a disk-resident state. Higher levels of data refinement and selection have therefore been devised, resulting in the so-called “nano-DST” format. The nDSTs are produced to be specific to subsystems and analyses; for example, the muon working group or MWG nDSTs contain information specifically intended for tracking and identification in the muon arm subsystems, while the photon working group nDSTs contain detailed calorimeter information for photon and π^0 reconstruction from clusters of EMCal towers.

Despite the large degree of sifting and compression provided by the nDSTs, the data volumes for all RHIC runs remain far too large to fit on disk at the RHIC computing facility. In order to optimize computing resources, the datasets are examined in their

entirety in coordinated passes via the “analysis taxi” framework. Put succinctly, various parties interested in a particular dataset submit their analysis code to a central “taxi driver” who coordinates the temporary staging of nDSTs for that dataset from the tape archive to disk for the execution of the analysis modules on the disk-resident files. Typical timescales to complete a pass of a particular dataset range from a few days to a few weeks, depending on the current availability of the resources relative to the load placed on them.

The final data used in this analysis was generated from the 163rd taxi pass in August 2009, in which 794 ERT-triggered PWG and CNT nDSTs were processed from Run 6, and 870 minimum-bias CWG nDSTs from Run 7.

In the Run 6 p+p dataset, 704 runs were included in the analysis as acceptable. In the Run 7 dataset, 870 runs were passed over by taxi 163. Among these runs were a subset of about 30 experimental runs with reversed polarity in the inner central magnet and/or additional converter material surrounding the beampipe for background studies. In addition, about 30 additional runs were identified as anomalous based on the shape of the mixed-event pair distributions. The distortions come about due to gain problems, partial trips, or other issues occurring in the detector subsystems during a run. The runs were grouped into 7 chronological categories, and the normalized mixed-event distributions for each run are compared with the summed (averaged) reference for their corresponding run group. Those deviating from a uniform distribution with a poor goodness-of-fit measure were considered as candidates for rejection. The ratio of each run’s background distribution to the reference was required to match a flat fit line within $\chi^2/ndf < 3$. In addition, the correlation functions themselves were examined for each run and checked for features that are anomalous beyond statistical deviation, as shown in figure 3.6. Again, runs having a $C(\Delta\phi)$ with $\chi^2/ndf < 3$ and an integrated value more than 5σ from the reference were examined as rejection candidates, leading to a final list of 55 rejected runs. The final good run list includes 840 runs.

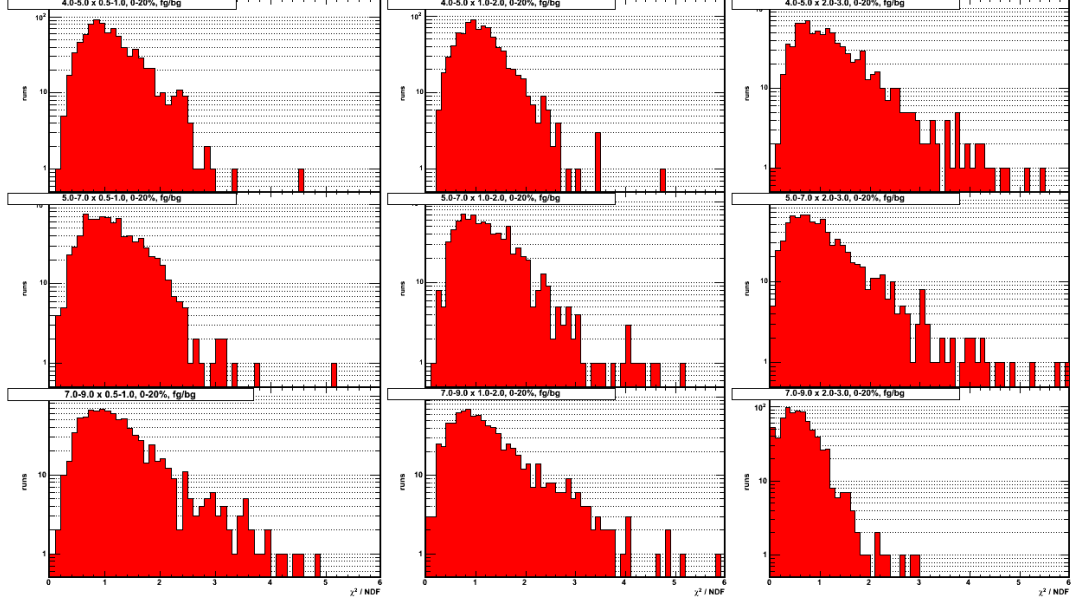


Figure 3.6: χ^2 distributions of $C(\Delta\phi)$ for central Au+Au for the p_T binning used in this analysis.

3.5 π^0 identification

The π^0 lifetime is 10^{-16} s, meaning that they travel 250 nm away from the collision point on average before decaying electromagnetically. The dominant decay channel is $\pi^0 \rightarrow 2\gamma$, occurring 98.8% of the time. The Dalitz decay $\pi^0 \rightarrow e^+e^-\gamma$ accounts for almost the entirety of the remainder. Neutral pions are reconstructed in the PbSc and PbGl calorimeters on a statistical basis by combinatorially pairing all acceptable photons within an event. The criteria for acceptability will be discussed below. The statistical method offers the benefit of naturally rejecting bad photon clusters due to the kinematic requirements involved in identifying a photon pair within a relatively narrow mass range, in particular compared with the identification of single or inclusive photons. The π^0 mass is then computed in terms of the energy and momenta of the decay photons $\gamma_i, \gamma_j, i \neq j$, as

$$m_{ij}^2 = (E_i + E_j)^2 - \mathbf{p}_i \cdot \mathbf{p}_j. \quad (3.21)$$

For photon pairs truly originating from the same parent, $E_i = E_j = p_i = p_j$ and $\mathbf{p}_i = -\mathbf{p}_j$ in the rest frame of the decaying π^0 , making equation 3.21

$$m_{ij}^2 = 2(E_i E_j - \mathbf{p}_i \cdot \mathbf{p}_j) = 2E_i E_j (1 - \cos \theta). \quad (3.22)$$

The opening angle θ is small for the ranges of π^0 momentum in this analysis. Decay angles are always isotropic and back-to-back in the π^0 rest frame, but they depend upon the π^0 momentum and the photon energy in the lab frame. The decay angle distribution is derived in Appendix D and shown in figure 3.7. The $\Delta\phi$ bin width

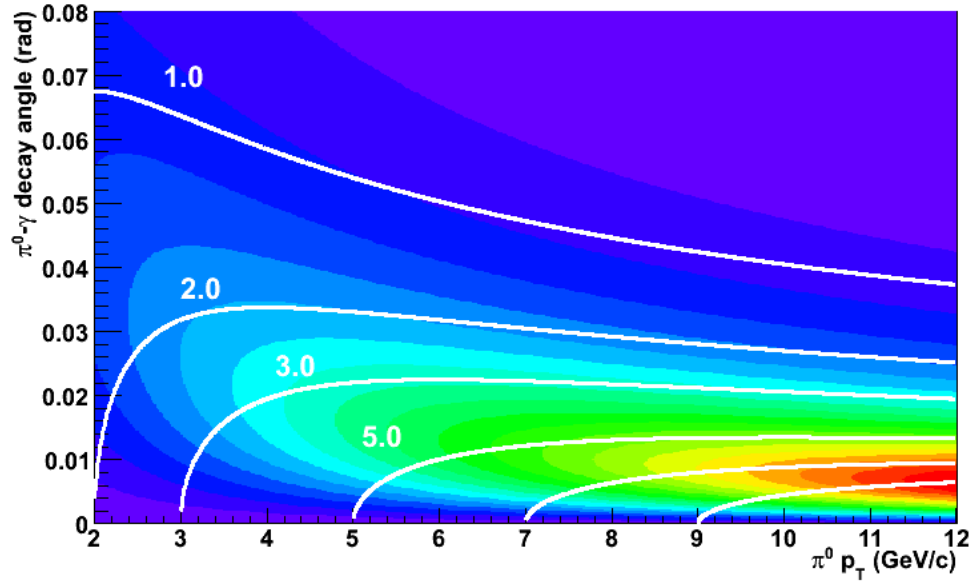


Figure 3.7: Distribution of decay angles between a parent π^0 and its decay photons as a function of $\pi^0 p_T$. The white lines represent kinematic bounds for photons within a given energy range. Smaller angles correspond to higher decay photon energies. For example, photons in the 1-2 GeV range have kinematically allowable decay angles within the two highest white lines.

in the correlations histograms of this study is $2\pi/30 \approx 0.21$ radians. Once the decay angles shown in figure 3.7 are projected into the azimuthal plane, they are typically at least an order of magnitude narrower than the bin width. More importantly, their separation is comparable to the size of the tower segmentation in the EMCal. Because of this small decay angle, it is important to address concerns related to merged EMCal

photon clusters. Typical EMCal clusters are a few tower-widths in extent, leading to angular sizes of roughly $\tan^{-1}(5\text{cm}/5\text{m}) \approx 0.01$ radians. Because the EMCal clustering algorithms are capable of identifying the centroid based on shower profiling, individual photons can be resolved to a much higher precision than given by their characteristic spatial extent. The PbSc has been shown to distinguish the decay photons from π^0 s with $p_T > 12$ GeV/ c , while the finer segmentation of the PbGl enables highly efficient π^0 resolution beyond 15 GeV. Since these momenta lie above the highest π^0 p_T range involved in this analysis, it is concluded that cluster merging is not a problem.

Although the π^0 mass is 134.98 MeV/ c^2 , the mean $m_{\gamma\gamma}$ obtained through calorimetry and reconstruction is closer to 140 MeV due to the smearing of the energy spectrum of the photons from the finite calorimeter resolution. The EMCal energy resolution is discussed in chapter 2. The imperfectly measured photon energies are somewhat higher or lower than the truth, each about half the time. Since the photon energy spectrum naturally drops very steeply with increasing energy, the symmetric energy smearing effect shifts this highly asymmetric distribution rightward to higher energies, since each bin receives more contributions from its left neighbor, on average, than from its right. The π^0 mass distributions for a subset (about 5%) of the Au+Au data are shown in figure 3.8. (The full dataset is not shown due to the long waits and large disk space requirements of full taxi passes.) The ≈ 5 MeV/ c^2 upward shift is evident in the plots. It can also be seen that the higher multiplicities of photons in lower- p_T and more central events lead to a larger combinatorial background rate. A fit consisting of a Gaussian peak and a quadratic background is applied to the mass distributions in order to assess the signal / background ratio. For 4-5 GeV π^0 s, the S/B is measured to be 4:1 within the 125-150 MeV window, meaning that 20% of the photon pairs in that bin are falsely-reconstructed π^0 s. The background photons originate from hadronic decays, most often other π^0 s and η s, as well as a contribution from prompt photons that increases with p_T .

In order to increase the S/B, a number of cuts are applied to the EMC clusters:

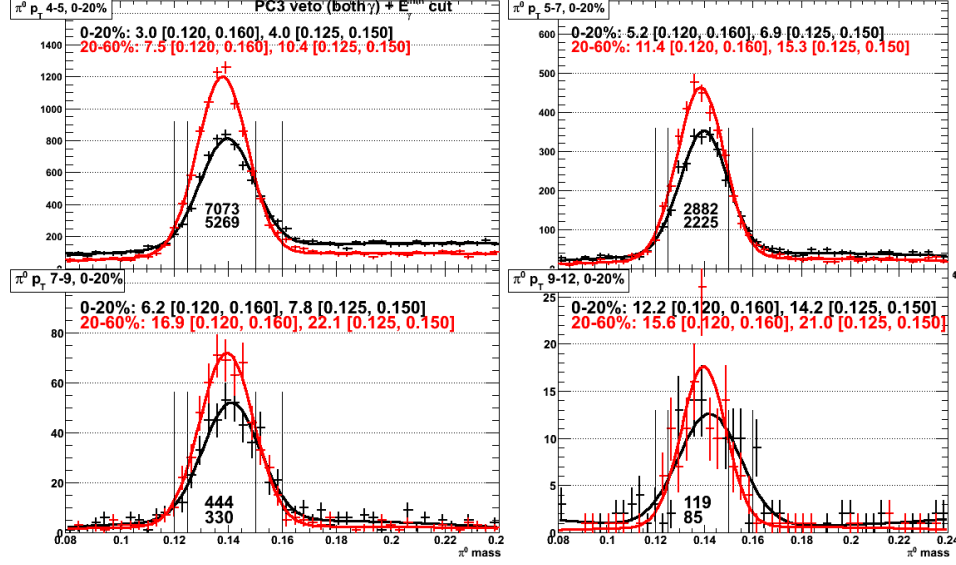


Figure 3.8: π^0 mass plots for Run 7 Au+Au. The vertical lines represent inner and outer mass windows used to determine the S/B ratio, which is printed for each centrality. The numbers inside the peak region represented the integrated yield in this subset of the data, used only to track cut efficiencies.

- EMC shower profile cut: each photon cluster must have a shower shape matching an ideal reference (determined through simulations) with a χ^2 value less than 3.0.
- Minimum photon energy cut. A common technique for improving the S/B in the combinatorial π^0 reconstruction method is to restrict the energy asymmetry of the two decay photons. Often the energy asymmetry parameter $\alpha = |E_i - E_j| / (E_i + E_j)$ is fixed below a certain value in order to reject the ubiquitous low-energy photons that raise chances for random pairing. For instance, applying an $\alpha < 0.8$ cut allows reconstruction from $10\% < E_\gamma < 90\% E_{\pi^0}$. Because the combinatoric background varies strongly with centrality and π^0 energy, a fixed asymmetry cut is not optimal for simultaneously rejecting background and maximizing statistics. In this analysis, a variable minimum photon energy cut

is applied during reconstruction, which has the form

$$E_{\gamma}^{min} = 0.7 + 0.8(1 - c) \exp [0.4(4.0 - p_T)] \quad (3.23)$$

where c is the fractional centrality (i.e. $c = 0.2$ for a 20% central event) and p_T is that of the π^0 . This equation is plotted in figure 3.9. The fixed asymmetry

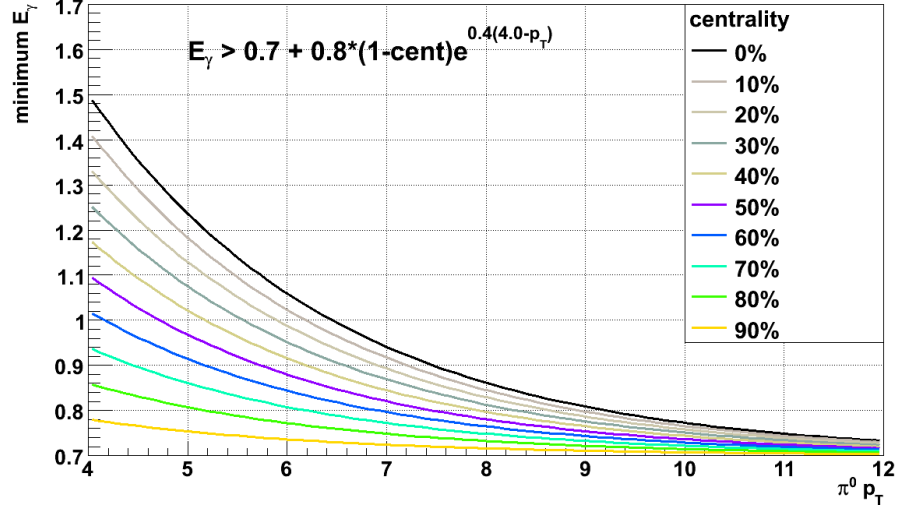


Figure 3.9: Minimum photon energy as a function of p_T and centrality. The cut is tightest where the combinatorial background is highest and the statistics can support stricter cuts.

cut is related to the minimum energy as

$$\alpha \leq \frac{E - 2E_{\gamma}^{min}}{E} \quad (3.24)$$

where E is the π^0 energy.

- The central tower in the cluster may not be designated as “hot”, as described in the following section. Additionally, the central tower of all clusters must not reside adjacent to hot tower, so that the bias in cluster position and energy is reduced.
- Mass cut. For $\pi^0 p_T < 5$ GeV, the mass range is 125-150 MeV, and for $p_T \geq 5$ GeV it is 120-160 MeV.

- Fiducial mask. No cluster may have a central tower on an edge sector, and photons must both hit the same sector to reduce any effects from gain or calibration mismatches between sectors.
- Charged track veto cut. This cut, and its corresponding mixed-event acceptance correction, is discussed in section 3.5.2, and is applied to both photons composing the π^0 .

3.5.1 Rejection of hot EMCal towers

As discussed in chapter 2, each of the six PbSc sectors contains $36 \times 72 = 2592$ towers, and both PbGl sectors each contain $48 \times 96 = 4608$ towers. Apart from multiplicity variation over the pseudorapidity range covered by the EMCal, which is small, the distribution of hits over a certain time period should follow Poisson statistics. However, faulty readout electronics on some towers cause them to send signals at abnormally high rates, and with unrealistic correspondence to true energy deposition, which interfere with reconstruction algorithms and produce spurious clusters. This is more of a problem than “dead” or “cold” towers, whose electronics either have failed completely or produce abnormally weak signals. The towers in these categories contribute to reduced acceptance and efficiency, but these effects are corrected through the process of event mixing.

The towers rejected as hot for the Run 7 data are those which have hit frequencies more than 4 times the mean number of hits per sector for a given energy range. The hit frequency distributions for each sector from a subset of the Run 7 data are shown in figure 3.10. The ranges used were 1-2, 2-5, and 5-20 GeV, where the cluster energy is given by E_{core} , a variable that includes dispersion corrections to the cluster energy. A unique set of 310 towers were rejected by this definition. An additional 3x3 tower mask is applied around each of these towers to avoid participation in nearby clusters.

Finally, the outermost row of towers in each sector is masked off to reduce the number of partial clusters at the edge of the acceptance. There are 1872 towers in this category. After the 3x3 and sector edge masking, there are 3229 rejected from the total count of 24,768. A very similar procedure was conducted in the Run 6 data by K. Boyle for his PhD thesis. A map of the rejected and masked towers is shown in figure 3.11 for Run 7, and the Run 6 hot tower map can be found at [33].

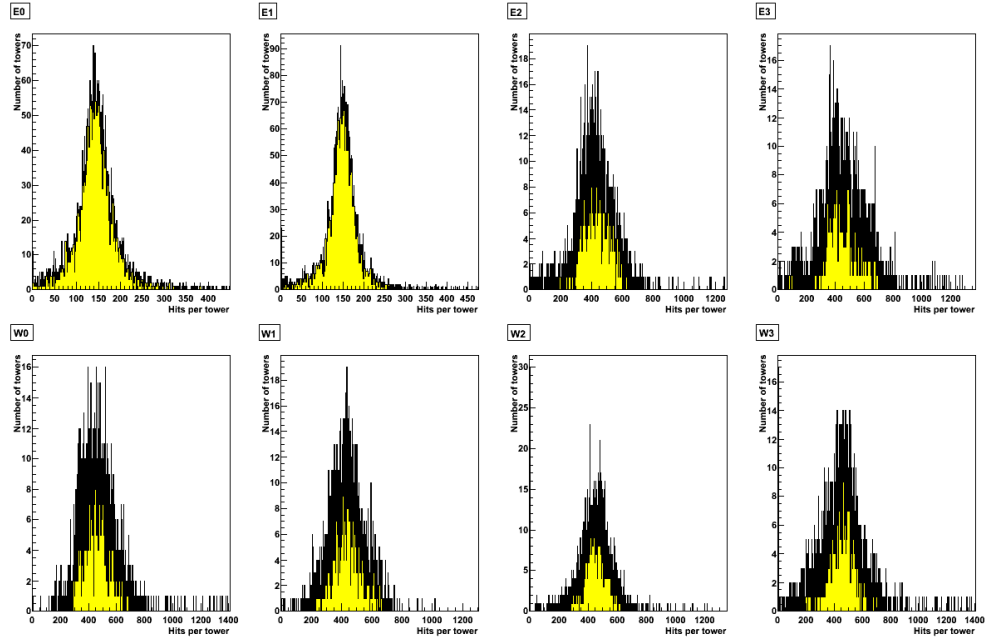


Figure 3.10: Tower hit frequency distribution in Run 7 EMCAL sectors. Towers recording greater than four times the mean number of hits are designated as hot.

The level of run-by-run variation was found to be small, so no runs were rejected solely on the basis of EMCAL quality assurance.

3.5.2 Handling charged track contamination in photon clusters

Although the EMCAL is optimized for measurement of electromagnetic (as opposed to hadronic) energy, the design does not allow for complete blindness to neutrons and charged hadrons. A large fraction of these background sources is rejected with the shower profile (χ^2) cut, but additional background remains. This can be seen in fig-

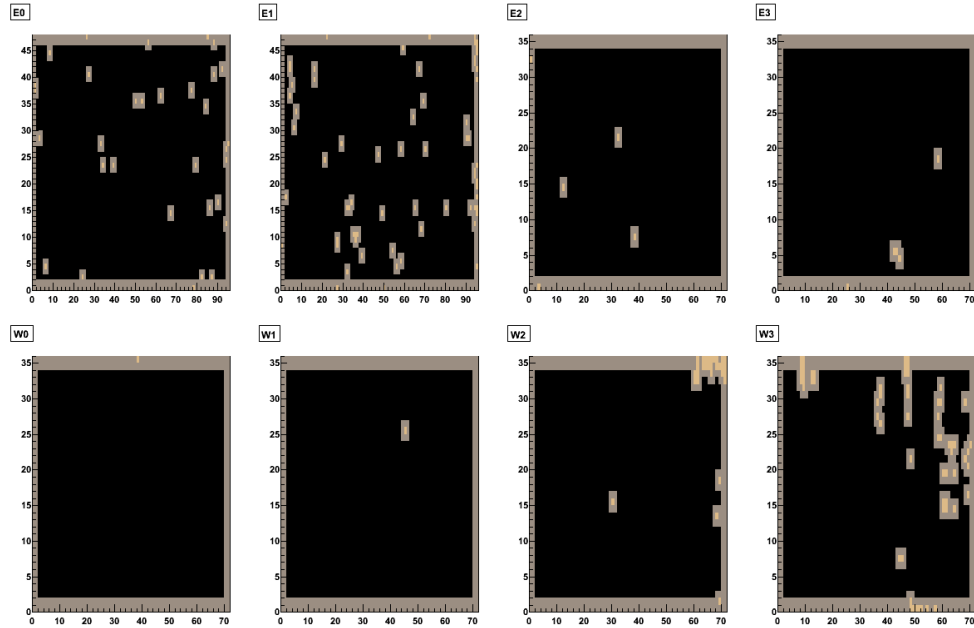


Figure 3.11: Map of hot and masked EMCAL towers in Run 7 as determined by the QA procedures described in the text. The axes represent the tower position within each sector. Sectors E0 and E1 compose the PbG1, and E2-W3 make up the PbSc.

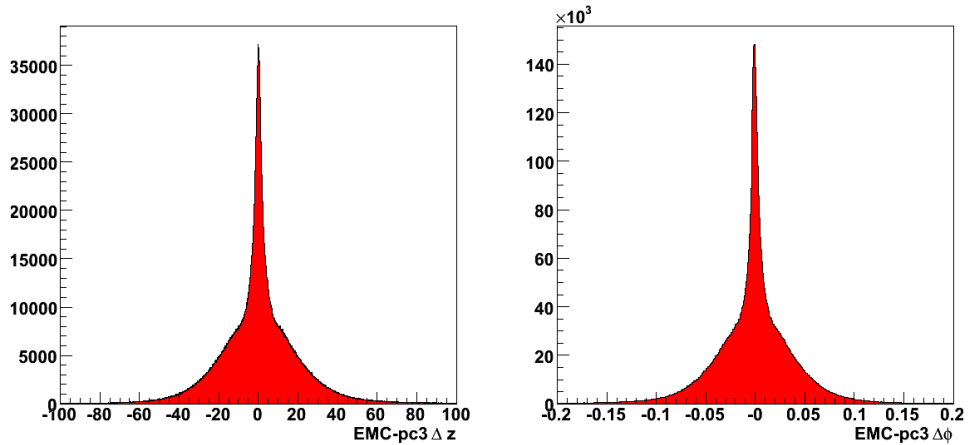


Figure 3.12: charged track contamination

Figure 3.12, which shows distributions of the proximity in ϕ in z between the center of each EMC cluster and the nearest PC3 hit in the event. Since the PC3 resides directly in front of the EMCAL, a sharp peak at close proximity statistically indicates the presence of contamination. Many contaminated clusters are rejected by masking a veto region

in EMC-PC3 $\Delta\phi \times \Delta z$ space. Any clusters that have charged tracks registering a PC3 hit within a small region around the cluster are not included in the analysis. The veto region is bounded by the ellipse

$$\frac{\Delta z^2}{\Delta z_{max}^2} + \frac{\Delta\phi^2}{\Delta\phi_{max}^2} < 1.0 \quad (3.25)$$

where Δz_{max} and $\Delta\phi_{max}$ are 10 cm and 0.02 radians. Since this rejection cuts an elliptical hole into the same-event pair acceptance, a corresponding hole is also removed from the mixed-event acceptance in order to correct for the loss. The same- and mixed-event distributions in $\Delta\phi \times \Delta z$ are shown in figure 3.13. Because there is no information

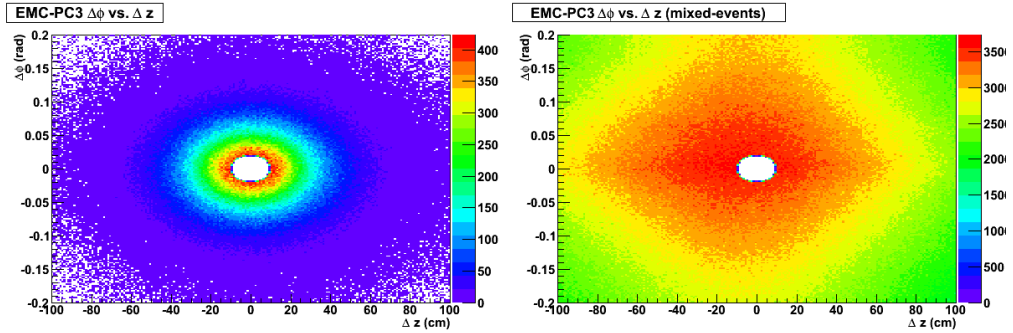


Figure 3.13: charged track veto for same and mixed evts.

stored in the data that lists the distance to tracks in other events for each cluster, the mixed-event PC3 veto correction is instead applied to charged tracks, which has the equivalent effect of removing pairs from the background acceptance.

3.6 Charged hadron track selection and high- p_T background

The charged hadrons in this analysis serve as the partner (type B) particles. This analysis includes a range in transverse momentum from 500 MeV/c to 7 GeV/c. A number of cuts were applied to the data in order to reject the background, which is a particular problem at high momentum. The background problem is discussed first, followed by a discussion of analysis cuts applied to reduce its effects.

3.6.1 Background in charged tracks

Although the DC/PC tracking system works well to identify “good” tracks with high position and momentum resolution, the lack of any tracking information between the collision vertex and the drift chamber allows a non-negligible contamination from background tracks. Almost all of the integrated magnetic field is contained inside the radial position of the initial DC window, so secondary particles originating more than a short distance from the event vertex do not suffer the expected deflection and are assigned incorrect momenta.

In general, the further the origination point from the event vertex, the straighter the track and the larger the reconstructed momentum. The deviation between true and reconstructed momenta can readily be observed in GEANT simulations of the PHENIX detector. Figure 3.14 depicts the fractional momentum difference between the

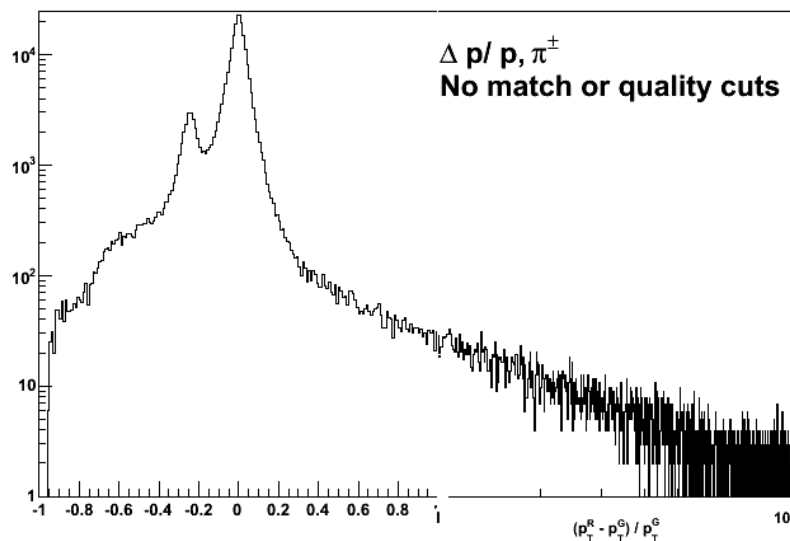


Figure 3.14: PISA simulation of difference between true and reconstructed track momenta. Note that the x -axis is logarithmic above 1.

true GEANT momentum and the momentum assigned in reconstruction. Since most background tracks that survive reconstruction are given momenta far higher than their

correct value, the background is most destructive to the data quality at high track p_T . Moreover, the mechanisms responsible for background production do not strongly depend on p_T , while the spectrum of true charged hadrons plummets steeply with increasing momentum, increasing the background contamination sharply as p_T rises.

The background sources can be distinguished in three categories:

- (1) Electrons from photon conversions. As photons from either hadronic decays (primarily π^0 and η) or from prompt processes interact electromagnetically with nuclei in air or material in the detector, e^+e^- pairs are produced. Based on simulations, the true electron momenta are typically around 0.5 GeV/c. The dominant material source for production of conversion electrons is the metal framing between the DC entrance window and the initial wire planes at about 2 m from the beampipe. Since the beampipe itself is Beryllium in the interaction region, and is close to the event vertex, it is not a large background source.
- (2) Secondary particles from decays. The primary decay sources include
 - Short-lifetime hadrons (primarily $K_s^0, \Lambda, \Sigma, \Xi$). The decay products are mainly muons, pions, and protons with momenta that are mildly smeared from their true value due to the momentum kick from the decay and the small offset of the decay vertex.
 - Longer-lived hadrons (primarily K_L^0, K^\pm) Due to the larger decay vertex offset, the pions and muons from these decays often receive a large kink in their trajectory relative to the parent.
- (3) Random associations from hits belonging to two or more different tracks. This problem is specifically related to matching track model projections from the inner tracking system to the outermost pad chamber, PC3. PC3 matching is discussed in section 3.7. This is an occupancy-dependent effect, and has

been roughly estimated [51] by comparing the size of the matching window to the mean PC3 hit spacing, which is about 25 cm in central Au+Au collisions, and significantly larger in peripheral Au+Au and p+p. Since typical matching widths in r - ϕ and z are each about 0.6 cm, the probability for a track to get a wrongly associated PC3 hit in a $3\sigma \times 3\sigma$ window is roughly

$$p_{RA} \sim (3\sigma)^2 / (25\text{cm})^2 < 1\%. \quad (3.26)$$

The random association background is therefore of less concern than the decay and conversion sources, and is included in the background component of the systematic uncertainty.

Fortunately, the mere presence of an energetic neutral pion trigger improves the signal relative to this background considerably, compared to inclusive events. This can be understood physically by recognizing that the events containing high p_T π^0 s are more strongly associated with hard scattering and jet fragmentation, so the hadron spectrum is harder. Despite this fortuitous effect, the augmented true spectra remain steeply dropping and an intrinsic limitation (apart from running out of statistics) is imposed on the upper reach of the track p_T . For both reasons (statistics and background) this upper limit was determined to be 7 GeV/ c .

3.6.2 Track quality

The reconstructed data for each charged track includes an bit mask that economically encodes information into a single integer about which components of the inner tracking system registered hits, and whether or not the hits are ambiguous. The encoding is shown in table 3.3. The highest possible track quality is 63, in which both X1 and X2 planes are used, and unique PC1 and UV hits have both been identified and associated with the track. As discussed in chapter 2, the PC1 is used as the principal source of z information, which is augmented by position information from the UV stereo

position	meaning
0x01 (2^0)	X1 plane used
0x02 (2^1)	X2 plane used
0x04 (2^2)	UV hit found
0x08 (2^3)	UV hit found and unique
0x10 (2^4)	PC1 hit found
0x20 (2^5)	PC1 hit found and unique

Table 3.3: Track quality bit encoding for the drift chamber and pad chamber 1.

wires. In the case where a PC1 hit is identified, but another is recorded nearby, a unique z -position verification from the UV planes provides the second best quality measure, which is encoded as 31.

Because the X1 and X2 systems each contain 12 wire planes, either system still provides detailed ϕ information, so an “or” of the two least significant bits often is acceptable if z is well constrained. The track quality distribution for the track p_T ranges

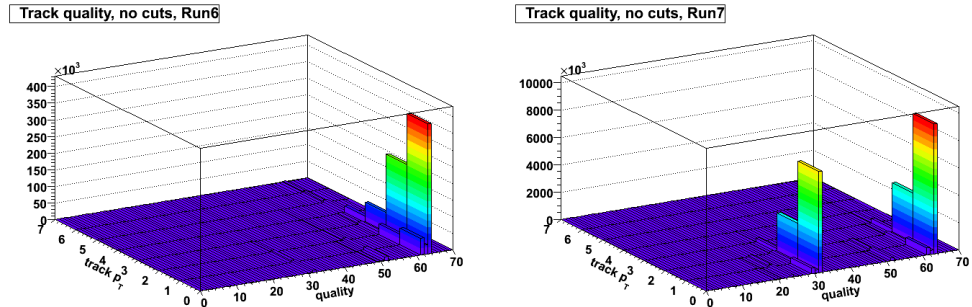


Figure 3.15: Distribution of track quality vs. p_T in Run 6 (left) and Run 7 (right). Even with no background rejection cuts applied, the distributions are dominated by the highest quality tracks (31 and 63).

used in this analysis are shown in figure 3.15. Because of the lower p+p multiplicities, ambiguous PC1 hits are far less common than for Au+Au. However, both distributions remain dominated by 31 or 63 patterns, at least at $p_T < \sim 5$ GeV/c. This provides confidence that reconstruction and ghost rejection algorithms provide tracks that are of generally high quality.

At higher track momenta, the background discussed in section 3.6.1 becomes sig-

nificant, and restrictive track quality requirements are important. A requirement of 31 or 63 is applied for all tracks for improved rejection of background particles from decays and conversions that point to the vertex and thus mimic real high- p_T charged hadrons. Although some efficiency is lost by applying a stringent track quality requirement over the full p_T range (as opposed to only at high p_T where it matters most), a modest loss in statistics is preferable to the potential introduction of spurious discontinuities in the final results due to differential cut efficiencies and their corrections.

3.7 PC3 matching

The outermost pad chamber, PC3, serves a critical role in rejecting background, since the tracks reconstructed in the DC and PC1 are projected outwards by the track model, and benefit greatly from the additional hit information obtained over 2 meters outward from the inner trackers. The resolution in the distance between the projected and recorded PC3 hit positions contains two components: the pointing, vertex, and hit resolution of the detectors, and the deviations occurring from multiple-scattering within the detector material and deflections in the residual field. The total resolution can be approximated as

$$\sigma_{match}^2 = \sigma_{det}^2 + \left(\frac{\sigma_{scatt}}{p\beta} \right)^2. \quad (3.27)$$

The σ_{det} term includes a centrality-dependent resolution contribution from the BBCs. Since p+p and peripheral Au+Au events fire fewer PMTs in the BBCs, the ability to resolve the collision z -vertex is degraded by about a factor of four compared to central Au+Au. This effect is discussed in more detail in chapter 4.

The degree of matching is quantified on a statistical basis in units of $n\sigma$ in the matching distance. Although the shape of the matching distribution more or less follows a compound Gaussian form with the width parameters given in equation 3.27, the means and widths first require recalibration from the measured $\Delta\phi$ and Δz variables so that

the mean of each distribution resides at zero and $\sigma = 1$. The purpose of converting to units of σ is to normalize out effects that depend on charge, momentum, centrality, etc. so that a single matching cut definition has a uniform meaning for all p_T and centrality categories. The recalibration procedure involves applying fit curves to the means and widths of the raw matching variables as a function of p_T , centrality, and position within the spectrometer. Provided that clear trends in these variables exist and good fits can be obtained, the offsets in the mean and width of each matching distribution are then continuously parametrized. The matching distributions are “signalized” using the raw variables and the offsets f_μ and widths f_σ from the fit curves, i.e.

$$\Delta x[n\sigma] = (\Delta x[\text{cm or rad}] - f_\mu)/f_\sigma \quad (3.28)$$

where $x = \phi$ or z . An example of the resulting match distributions for high-quality tracks is shown in figure 3.16. The `n0` variable is the number of RICH phototubes within an annular region around each track. Since their small mass means that electrons have a larger velocity than charged hadrons at a given p_T , they begin to emit cherenkov light well below 1 GeV/c, while pions do not begin radiating until $p_T \approx 4.7$ GeV in the RICH. Therefore some fraction of the background electrons can be vetoed by requiring that no cherenkov light is seen in the RICH below the pion cherenkov momentum threshold.

However, the electron veto cut was not found to be as effective as might be anticipated. The signal enhancement can be seen in figures 3.16 and 3.17 to be only modest, particularly in the conditional data used in this analysis. One reason for this is simply that the RICH does not capture light from all background electrons, but another is that the electron veto cut can only be applied to tracks with momenta below the pion momentum threshold to avoid vetoing the signal itself, and many of the conversion electrons are reconstructed with momenta at or above this value due to their production far from the event vertex. There is also a significant loss of efficiency in the application of the RICH veto cut, since the high multiplicities allow some tracks to be falsely

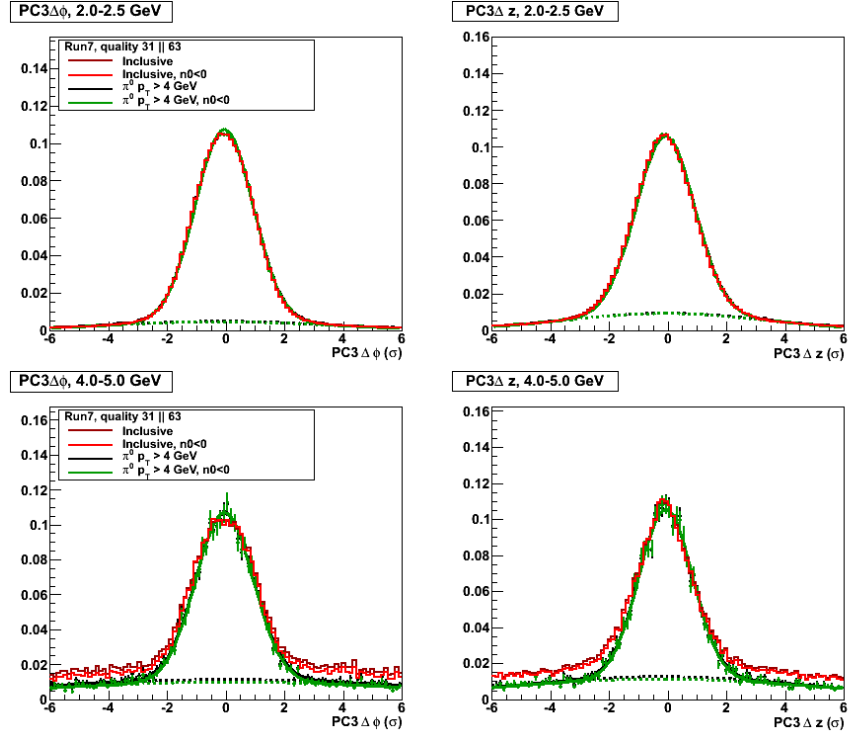


Figure 3.16: Examples of PC3 matching distributions for two different track p_T ranges. In each case the distributions are normalized to match near their maximum value in order to compare the tail components.

associated with the cherenkov light from nearby electrons.

The increased background contribution is discernible in the higher p_T bin at the bottom of figure 3.16, where the tail component is increased relative to the peak. In the 4-5 GeV bin, a slight reduction in the background is discernible, but the normalization does not permit the observation that this modest improvement comes at a cost in the form of a sizable reduction in the peak region as well. As expected, the track sample conditioned on the presence of a high- p_T π^0 maintains a higher S/B ratio.

An additional way to observe the onset of background contamination in the track sample is to compare the p_T distributions between tracks having a tight PC3 match (presumably, therefore being a cleaner sample) and those with a relatively loose matching cut. A rise in the ratio of the more contaminated p_T distribution to the cleaner one therefore signals the onset of contamination. This ratio is shown in figure 3.17,

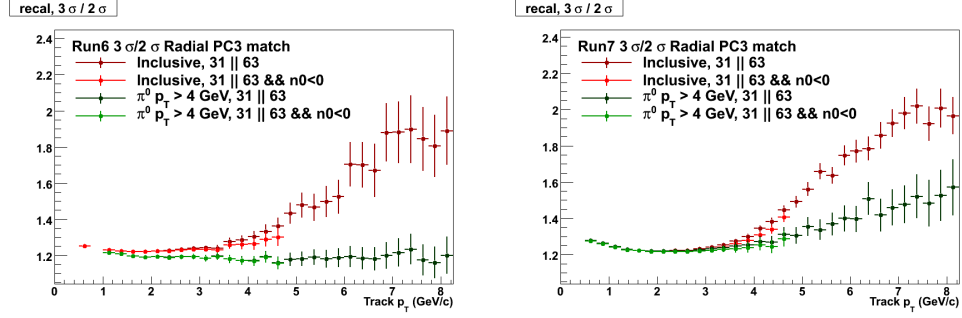


Figure 3.17: Ratios of p_T distributions in Run 6 (left) and Run 7 (right) with loose versus tight PC3 matching requirements.

which suggests the unsurprising trends that the p+p data remains cleaner than the Au+Au tracks at significantly higher momenta, and that the conditional data of this study suffers considerably less from background contamination than inclusive data. In addition, the same modest gain in the application of the RICH electron veto cut can be seen below the pion threshold.

3.8 Summary of track cuts

Based on a detailed study of the background, a fairly tight set of analysis cuts is applied to the track sample, while still taking effort to minimize losses in statistics.

- A radial 2σ PC3 match cut is applied to both Au+Au and p+p below over the full track p_T range.
- A track quality cut requiring unambiguous PC1 or UV hits in addition to an X1 or X2 hit is required over the full momentum range, corresponding to the two highest quality bit patterns (31 or 63).
- Although studied in detail, no RICH electron veto cut is applied, due to its low efficiency relative to the background rejection power. Eschewing this cut also has the benefit of simplifying (and reducing systematic uncertainties associated with) the acceptance, efficiency, and occupancy corrections applied to

the conditional yields, described in chapter 4.

3.9 Elliptic flow measurements and background subtraction

As described in section 3.2.1, the combinatoric background in the azimuthal trigger-partner pair distributions is assumed to follow a harmonic modulation given by equation 3.8. In p+p data, the amplitude of this modulation is taken to be zero, since no anisotropic flow has been observed in p+p collisions. However, the flow component contributes significantly to the anisotropy of the Au+Au pair distributions, particularly when the jet signal is small (of order a few percent) compared to the background level. It is therefore important to obtain a well-constrained measure of this elliptic flow component in Au+Au.

The pair v_2 is the simple product of the single-particle flow v_2 amplitudes, as explained in section 3.2.2. The elliptic flow for π^0 s has been carefully measured in PHENIX, and contamination from non-flow effects has been demonstrated to be small, because the reaction plane has been determined by several different subsystems in PHENIX (BBC, MPC, inner/outer/combined RXNP) and highly consistent results were observed. Moreover, these subsystems are widely separated in pseudorapidity from the central arm spectrometers, where the anisotropy itself is determined. This separation reduces the opportunities for jets or other phenomena to auto-correlate the event plane with the flow, although it has been suggested that long-range correlations associated with ridge physics should not be ruled out as conceivable influences.

The v_2 values from Run 7 PHENIX data are shown in figure 3.18. The data was analyzed using the MPC to determine the reaction plane and the EMCal for the flow measurement itself. A comparison with the 2004 data highlights the threefold increase in statistics, as well as the improved reaction plane resolution available with the newer detector subsystems.

The unidentified charged hadron v_2 measurement has already been shown in the

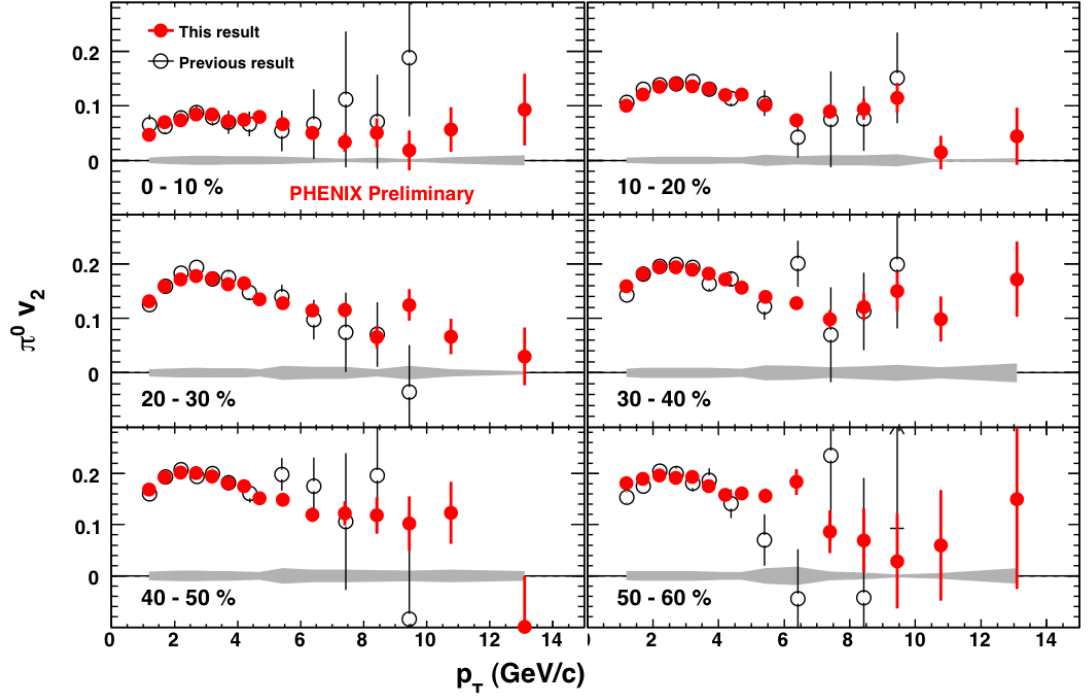


Figure 3.18: Run 7 $\pi^0 v_2$ [72].

introduction (figure 1.11). Because that data is only measured up to about 4 GeV/c, an estimate is provided by extrapolating the value in the 3.5-4 GeV/c range. Although this may appear to be an extremely crude approximation, it contributes only a very small uncertainty, because the flow becomes a practically negligible contribution to the correlations above 4 GeV, where the peak amplitudes in the correlation function rise orders of magnitude above the flow contribution. Even if the charged hadron flow were to be varied by a factor of two, the variation would propagate to the final uncertainty at or below the level of a few percent. Moreover, the flat extrapolation is most likely an over-estimation of the flow, since it is implausible that the magnitude of the charged hadron flow would differ enormously from that of the neutral pions, particularly above the recombination region (5-6 GeV).

The v_2 data are for each component are combined with a weighting provided by the centrality distribution of the particles. The result is shown in figure 3.19. The

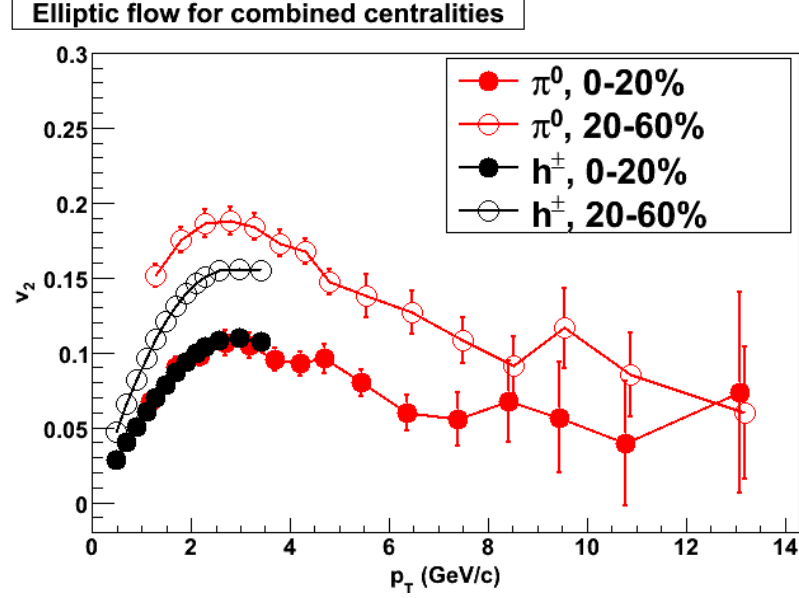


Figure 3.19: Run 7 π^0 and h^\pm v_2 in combined centrality bins. A constant extrapolation is made above the h^\pm data.

product of the two curves, using the aforementioned h^\pm extrapolation, is tabulated below.

π^0 p_T (GeV/c)	π^0-h^\pm pair $v_2 \times 10^{-2}$, 0-20%				
	h^\pm p_T (GeV/c)				
	0.5-1	1-2	2-3	3-5	5-7
4-5	0.38 ± 0.04	0.67 ± 0.06	0.98 ± 0.09	1.01 ± 0.09	1.01 ± 0.09
5-7	0.30 ± 0.04	0.53 ± 0.07	0.78 ± 0.10	0.81 ± 0.10	0.81 ± 0.10
7-9	0.24 ± 0.09	0.42 ± 0.15	0.63 ± 0.22	0.64 ± 0.23	0.64 ± 0.23
9-12	0.20 ± 0.16	0.35 ± 0.28	0.51 ± 0.41	0.53 ± 0.42	0.53 ± 0.42

Table 3.4: 0-20% pair v_2 values

π^0 p_T (GeV/c)	π^0-h^\pm pair $v_2 \times 10^{-2}$, 20-60%				
	h^\pm p_T (GeV/c)				
	0.5-1	1-2	2-3	3-5	5-7
4-5	1.08 ± 0.06	1.81 ± 0.09	2.48 ± 0.13	2.53 ± 0.13	2.53 ± 0.13
5-7	0.90 ± 0.09	1.50 ± 0.16	2.06 ± 0.22	2.11 ± 0.22	2.11 ± 0.22
7-9	0.69 ± 0.11	1.15 ± 0.18	1.58 ± 0.25	1.61 ± 0.25	1.61 ± 0.25
9-12	0.69 ± 0.18	1.15 ± 0.30	1.58 ± 0.41	1.61 ± 0.42	1.61 ± 0.42

Table 3.5: 20-60% pair v_2 values

3.10 Correlation functions

The full set of correlation functions for Au+Au and p+p are given in appendix F.

Chapter 4

Data corrections and systematic uncertainties

For any analysis resulting in measurements of particle yields, a correction is normally required to account for the detector's inability to measure every particle produced in the sample of recorded events, since detectors in high-energy experiments are never perfectly hermetic or efficient. In this analysis, three primary effects that dominate the reduction in particle yields are carefully considered: acceptance, efficiency, and occupancy. The former two are very difficult to disentangle experimentally, and are grouped as a product. A correction for their influence involves a Monte Carlo simulation of randomly-generated single particles interacting in a highly detailed mock-up of the detector. The result is a single-particle correction (SPC) which accounts for dead or inefficient detector areas, in-flight decays, momentum resolution, and reconstruction efficiency. The latter correction accounts for tracking inefficiencies due to occupancy effects that become non-negligible in high-multiplicity environments, and is referred to as the occupancy efficiency correction (OEC).

For this analysis it is assumed that the SPC and OEC factorize, so although there is some overlap in the calculation techniques leading to the corrections, they are treated as mathematically independent. For p+p data, detector occupancies are low enough that only the SPC is required, while Au+Au yields require both corrections.

Two general strategies have been employed to estimate the SPC. The first is to generate simulated tracks and model the response of the PHENIX tracking system

using PISA, the PHENIX Integrated Simulation Application, which use the venerable GEANT [20] libraries to model the detailed processes of energy loss, secondary particle production, and detector response in a model that closely replicates the geometry and materials of PHENIX. The number of reconstructed and original tracks can then be compared within the same ideal angular region to estimate the acceptance \times efficiency.

A second method obtains a correction by comparing the raw single-particle yield from a given analysis with a fully corrected yield, typically from a PHENIX publication. However, this “bootstrap” method is ultimately equivalent to correcting the data back to data that was corrected using the first method at some earlier time, critically relying on the accuracy of the original work. Given that there are precious few benchmarks for gauging whether the efficiency corrections are truly scaling the yield measurements to their true physical values, the merit of the bootstrap method lies in its ability to make contact with mature analyses which have presumably undergone extensive vetting and testing. The attainment of agreement between the simulation and bootstrap methods thus provides a useful consistency check for the more rigorous simulation method.

The occupancy correction attempts to account for the inability of the hardware and the reconstruction to perfectly separate hits which are close in position and time. When such overlaps are numerous, the number of properly reconstructed tracks is significantly reduced. The inefficiency (which is the inverse of the OEC) is estimated by an embedding procedure which attempts to confuse the track reconstruction process in a controlled way and examine the results. In the embedding procedure, Monte Carlo tracks are run through PISA (as for the SPC) and merged with a background of real data detector hits, i.e. after the detector response is recorded, but before the reconstruction and tracking is performed. Since the original MC information is known, the number of reconstructed tracks that originated from primarily MC hits can be recorded and compared with the case in which un-merged MC hits are reconstructed.

4.1 Single-particle acceptance \times efficiency: Monte Carlo method

Schematically, this SPC study involves 4 principal stages:

- (1) Generate simulated particles, one per Monte Carlo “event”.
- (2) Run generated particles through PISA to acquire detector response, conversion and decay background particle information, etc.
- (3) Run the standard PHENIX offline reconstruction routines on the PISA hits.
- (4) Compare the number of reconstructed tracks having passed the analysis cuts to the number original particles put into the simulation to evaluate acceptance \times efficiency.

Each of these steps will be discussed in detail in the following sections.

4.1.1 Generation

A simple hand-written fast monte carlo generator was used to throw single π^\pm , k^\pm , p , \bar{p} particles, about 20 thousand of each type. The particles were generated with uniform pseudorapidity and azimuthal dependence, within $[0, 2\pi]$ and $|\eta| < 0.5$ respectively. The z -vertex of each particle was chosen to identically match that of a corresponding real data event from Run 7 DSTs¹. This is done primarily to make the embedding process more accurate, and secondarily to simulate a realistic z -vertex distribution. All z -vertex values lie within ± 30 cm of $z = 0$, as specified in the real analysis. In order to maintain statistical uniformity across a broad momentum range, the p_T distribution was chosen to be flat from 0-12 GeV. The spectra are later weighted to simulate momentum resolution effects.

¹ See section 3.4.2 for discussion of the PHENIX Data Summary Table format

4.1.2 Simulation and Reconstruction

Separate PISA simulations were carried out for Runs 6 and 7. The dead and inefficient areas in the DCs and PCs have varied over time as the central arm spectrometers have aged and undergone repair and maintenance, so a separate map of dead channels is used for each year. More temporally fine-grained maps are not implemented, but the variation within each running period is not typically large, since any DAQ runs with large-scale channel trips or other failures are rejected from the physics datasets. Additionally, the separate simulations reflect changes in detector configurations as subsystems are installed or removed. In the shutdown prior to the 2007 run, the hadron-blind detector was installed, but its west half was removed after one month (about one third of the physics running period) due to mechanical problems. Since the majority of the data was taken after this period, the simulation was run without the HBD-W included. Due to its fairly low material budget, its contribution to additional conversion background is expected to be modest, and comparisons of trial runs of the simulation in both configurations did not indicate any significant differences in the results.

Once the simulated events are accumulated, the standard PHENIX tracking and reconstruction framework is applied to the data. The primary difference between Runs 6 and 7 lies in occupancy effects and in the difference in the z-vertex resolution of the BBCs. As mentioned earlier, the former is handled in a separate procedure, and is described in section 4.3. The latter depends strongly on the number of BBC phototubes receiving a hit in a given event. In p+p and peripheral A+A collisions, the resolution is approximately 2 cm, which is broader by about a factor of 4 than for central AuAu events. Since the BBC z-vertex position is determined by the hit times registered by BBCN and BBCS,

$$z_{BBC} = \frac{z_N + z_S - c(t_N + t_S)}{2} \quad (4.1)$$

the position resolution of the vertex can be inferred from the timing resolution of the BBCs:

$$\sigma_{z,BBC} = \frac{c}{2} \sqrt{\sigma_{t,N}^2 + \sigma_{t,S}^2}. \quad (4.2)$$

Assuming that the timing resolution of the BBC improves with the number of tubes that fire per event, N , i.e. $\sigma_t = \sigma_t^{\text{sing}}/\sqrt{N}$, the resolution is estimated as

$$\sigma_{z,BBC} = \frac{c\sigma_t^{\text{sing}}}{2} \sqrt{1/N_N + 1/N_S} \quad (4.3)$$

An important feature of this resolution is that its shape contains a tail component such that it is not precisely Gaussian. The offline reconstruction software was modified to account for this multiplicity-dependent effect. In a MC routine, the number of BBC

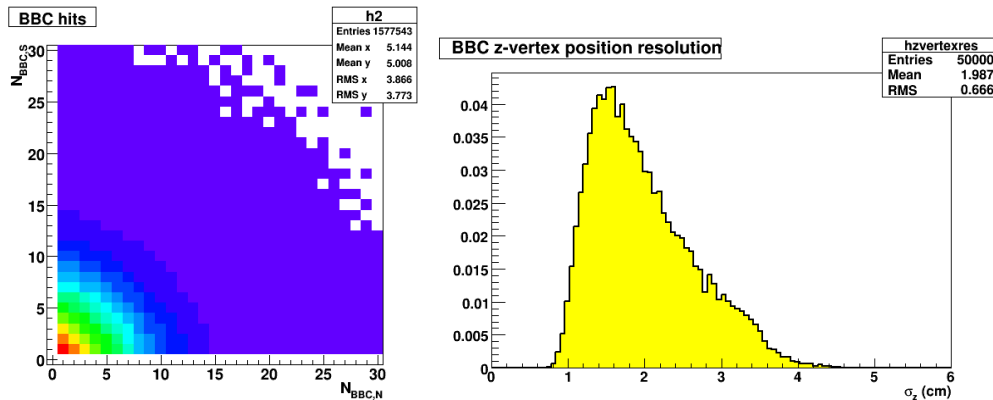


Figure 4.1: Left: Number of tubes registering a hit in BBCS vs. BBCN from Run 6 minimum bias data. Right: BBC z-vertex resolution calculated via eq. 4.3 using the N-S hit distribution.

tube hits is sampled from real Run 6 data as shown in figure 4.1 in order to calculate z_{BBC} , also shown in the figure.²

² The single-tube timing resolution was tuned to 160 ps in order to reproduce the 2 cm resolution typically quoted for p+p. This appears to be a factor of 4 larger than the 40 ps resolution quoted by BBC experts in early PHENIX internal documentation. The BBC experts were consulted on this, but no explanation for the discrepancy has been obtained to date. However, the goal of the method is to cause PC3 matching distributions in low-multiplicity events to match data, which is accomplished in this study, as shown in section 4.1.6

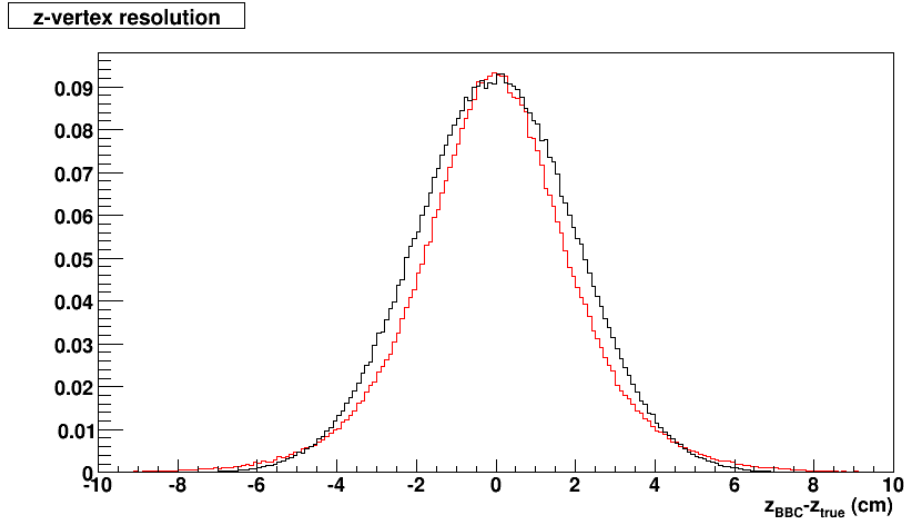


Figure 4.2: Black: simulated z -vertex smearing from a Gaussian with $\sigma = 2$ cm. Red: z -vertex smeared by a Gaussian with a variable width sampled from the right-hand distribution in figure 4.1. The amplitudes are normalized together to demonstrate the distortion introduced by using the multiplicity-dependent σ distribution.

The vertex resolution is compared in figure 4.2, where the non-Gaussian tails can be seen for case (b). The effect is here by a simple monte carlo simulation in which a distribution of z -vertex positions is compared for the case of (a) fixed 2 cm Gaussian smearing, and (b) the tube multiplicity-dependent case described by equation 4.3. For the Run 6 simulation, a private version of VtxSimreco was modified to allow smearing by a variable Gaussian σ sampled from the distribution shown in figure 4.1. This modification resulted in a broadening of the tail component in the PC3 Δz distributions that more accurately matched the data.

For Run 7, there was no smearing (of any kind) applied to the z -vertex in order to preserve a match to the data for embedding study. The measured Au+Au BBC tube multiplicities indicate that, according to equation 4.3, the resolution approaches its optimum value once collision centralities go below about 60%. In other words, the effect is only significant in events whose centralities are more peripheral those involved in this study, so the effect is not relevant here in the Au+Au case. The simulation

results bear this out as well: the shape and width of the MC and data PC3 matching distributions for Au+Au agree closely without the z-vertex smearing applied (see section 4.1.6).

4.1.3 Momentum resolution

The momentum resolution of the central arms is limited by the uncertainty of the drift chamber bend angle α and, at $p_T < 2$ GeV, by multiple scattering. It was determined in Run 2 that $\delta p/p = 0.9 \pm 0.1\% \oplus 1.0 \pm 0.1\% p$ GeV/ c [51]. This effect is preserved in PISA and in this study by weighting the p_T distribution of the reconstructed tracks by a power law shape obtained from a fit to real data. The low- p_T background tracks that become reconstructed as high-momentum tracks tend to cause large spikes in the reconstructed p_T distribution due to this weighting, obscuring the efficiency calculation. To mitigate this problem, a loose cut is applied which requires that the reconstructed momenta agree with the truth within 20%. A distribution of this $\Delta p/p$ variable is shown in figure 4.3. The $\Delta p/p$ cut removes only 1-2% of the tracks, the majority of which originate below $p_T \sim 1$ GeV. The goal is to simulate the acceptance and efficiency of good tracks in this study, so this cut is well motivated as a way to clean up the efficiency curves without significantly affecting the efficiency, since the basic assumption is that the SPC is not making attempts to directly model the background. If such an attempt were to be made, heavier particles would need to be generated in physical proportions and simulated in order to generate decay products, but such a study is outside the scope of this correction.

4.1.4 PC3 matching recalibration

As discussed in chapter 3, the track matching requirements are measured in units of σ as a uniform way to specify the hit-projection agreements. Unfortunately, the reconstruction process for simulated PHENIX data does not currently lead to correctly

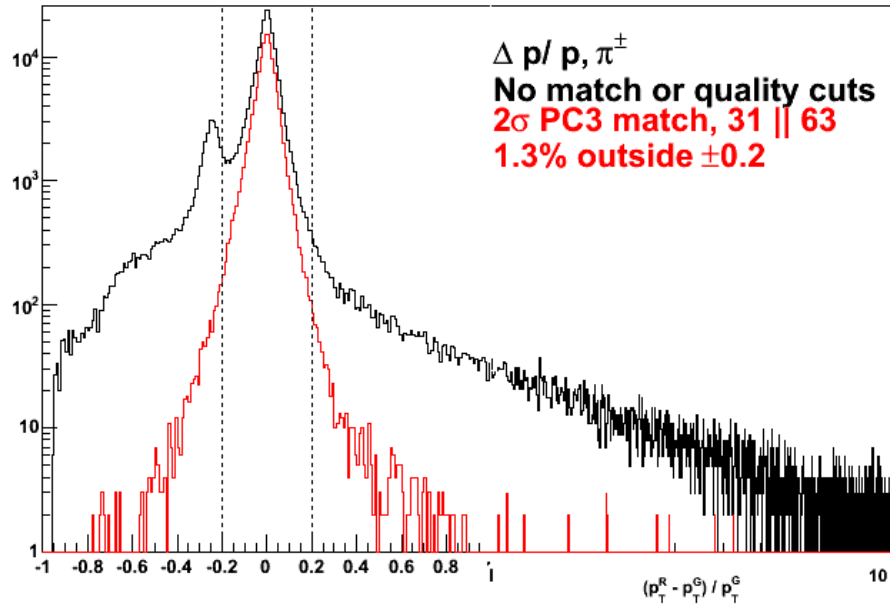


Figure 4.3: Momentum resolution distribution for π^\pm tracks from PISA with and without the analysis cuts applied. The x-axis is logarithmic above $\Delta p/p = 1$. In this study the reconstructed tracks are required to agree with their true counterparts within 20% to remove the worst of the background. The cut removes undesirable fluctuations in the efficiency curves, but has a negligible impact on the efficiency.

calibrated PC3 matching distributions. It was discovered in the course of this study that the overall efficiency value is highly sensitive to the shape of the PC3 match distribution. Thus, considerable attention has been devoted to tuning the match distributions for this analysis. The objective is for both real data and monte carlo to have match distributions within 0.1σ of 0 for mean and 1 for the width.

The recalibration procedure begins by histogramming the raw PC3 $\Delta\phi$ and Δz variables with the following cuts applied:

- quality 31 or 63
- $\Delta p/p < 0.2$
- orthogonal match cut:

* $|\text{PC3 } \Delta\phi| < 0.01 \text{ rad for PC3 } \Delta z$

* $|\text{PC3 } \Delta z| < 10 \text{ cm for PC3 } \Delta\phi$

The distributions are then fit with a compound Gaussian form (narrow + broad components, see equation 3.27), and the means and widths of the signal component are plotted as a function of p_T . They are fit with an exponential function,

$$f(p_T) = Ae^{Bp_T} + C, \quad (4.4)$$

whose slope is permitted to take on positive or negative values such that this single functional form can be used for all Gaussian parameters. The matching distributions are “sigmalized” as explained in section 3.7, and the results are shown in appendix E (figure E.3). It can be seen that precise fits were not required to successfully adjust the means and widths of the recalibrated distributions to their target values.

4.1.5 Acceptance correction

It is not practical to perfectly match the overall acceptance level determined through Monte Carlo to that of the data for two primary reasons. First, run-by-run variation: each simulation is reconstructed using only a single representative DAQ run number at a time to obtain the drift chamber dead channel map. It would be prohibitive in terms of CPU time and disk space to reconstruct the PISA hits with over 1500 separate run numbers to determine the temporal variation. The pad chambers tend to be more stable in terms of dead channels, and there is only a single PC deadmap assigned for each RHIC run. Thus, run-by-run variations are not perfectly simulated in this study. Secondly, and more importantly, the overall efficiency levels for relatively good areas of the detector are not identical between MC and data. Due to these effects, the acceptance difference is one of the dominant sources of systematic uncertainty in the overall efficiency correction.

Two complementary procedures were used to estimate this mismatch, both involving the comparison between MC and data for areas of high (but not anomalously high) track density in the full tracking acceptance (DC + PC1 + PC3)³. These regions are selected as the “good” areas, a distinction which, while carrying some element of subjectivity in their visual identification, is fairly clear and intuitive, given that there are regions where the track density is uniformly high over a reasonable extent of the acceptance.

The first method, denoted here as the 2D method, involves selecting three different rectangular good regions in each quadrant (NE, NW, SE, SW) of the tracking acceptance in both MC and real data (RD). The resulting variation between the trials provides an estimate of the uncertainty associated with selecting the different efficient regions. The track density distributions are shown in figure 4.4. The rectangles are chosen to cover a large enough area to avoid being dominated by fluctuations. In each quadrant, the track densities are normalized to the good regions, then the MC/RD ratio of the overall integrals quantifies the agreement level. This is equivalent to assuming that the good areas are perfect, then comparing MC and RD under this assumption. It can be seen in the figures that the overall acceptance \times efficiency scale is several percent higher in MC than in real data.

The second method, denoted the $\phi \times z$ method, is complementary to the first: it consists of projecting the acceptance to ϕ , picking a good region, then projecting the 2D acceptance to z within that good ϕ window. These projections are shown in figures 4.5 and 4.6.

In both methods, the final correction is evaluated as the mean of the three trials for each sector, and the uncertainty is estimated by the standard deviation. The averages are then combined with a weight corresponding to the relative track density in each

³ The projected PC3 position serves as a proxy for the full central arm acceptance since an entry in this distribution includes DC+PC1 tracks which have survived the quality cut, and the 2σ PC3 match requirement factors in the PC3 acceptance by construction.

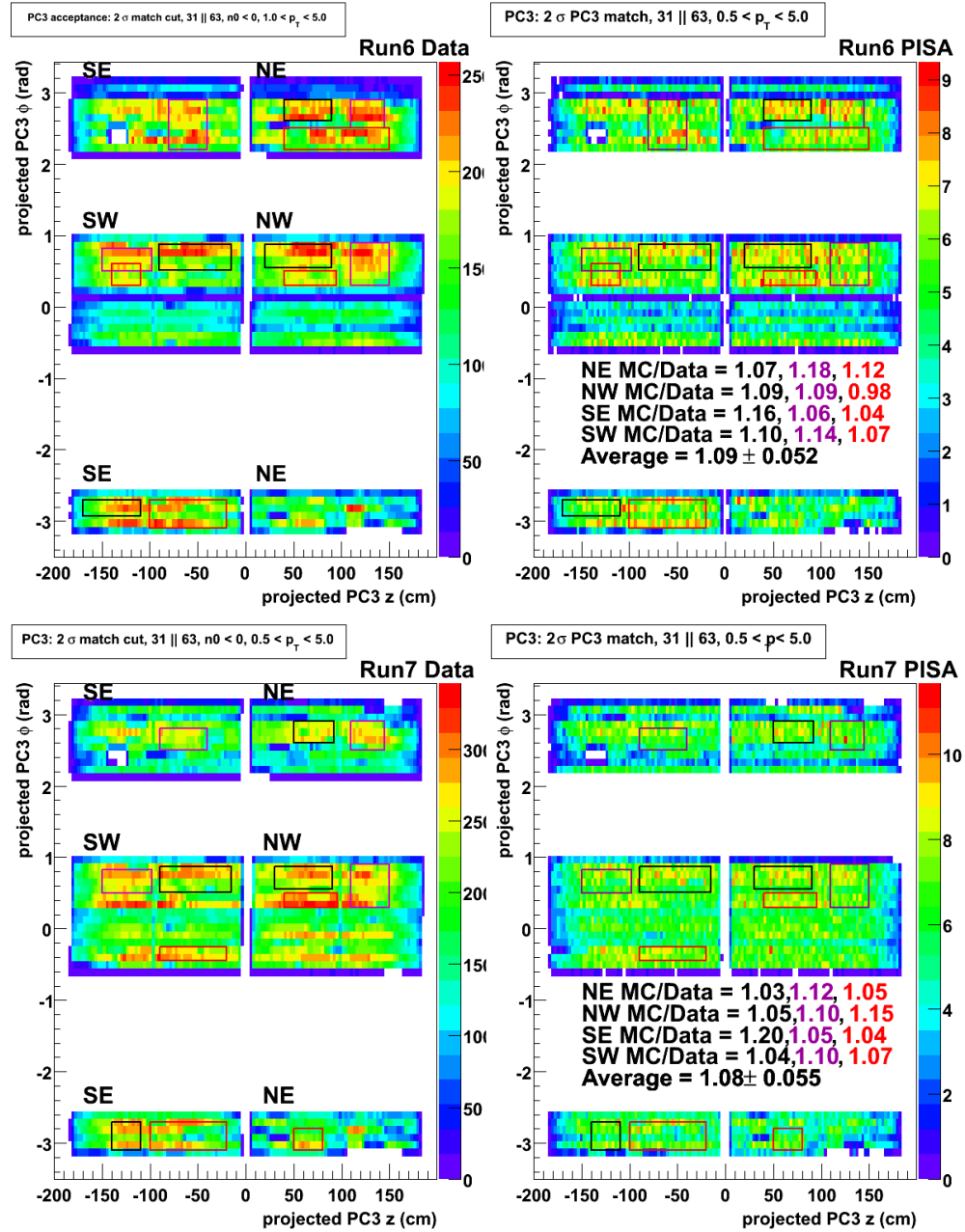


Figure 4.4: Run 6 and Run 7 acceptance for data and MC. The ratios of the boxed regions are used to estimate the acceptance correction and its systematic uncertainty. The correction and its systematic uncertainty were calculated as the mean and standard deviation over the $\times 3$ trials for each sector, then averaged over the sectors.

quadrant, such that the sector with higher track counts is allowed to contribute more (in practice, the weights were nearly equal). The weighted average over the four quadrants gives the final results for both methods, summarized in table 4.1. These numbers are

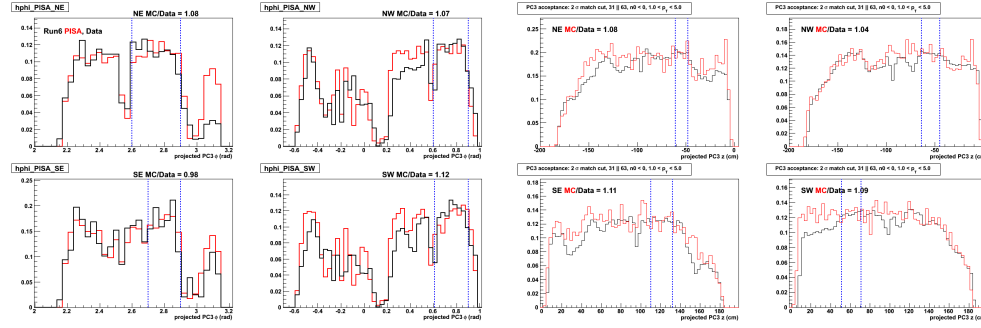


Figure 4.5: Run 6 ϕ (left) and z (right) distributions for data (black) and MC (red). The ratios are used to estimate the acceptance correction and its systematic uncertainty as a complementary cross-check of the 2D method.

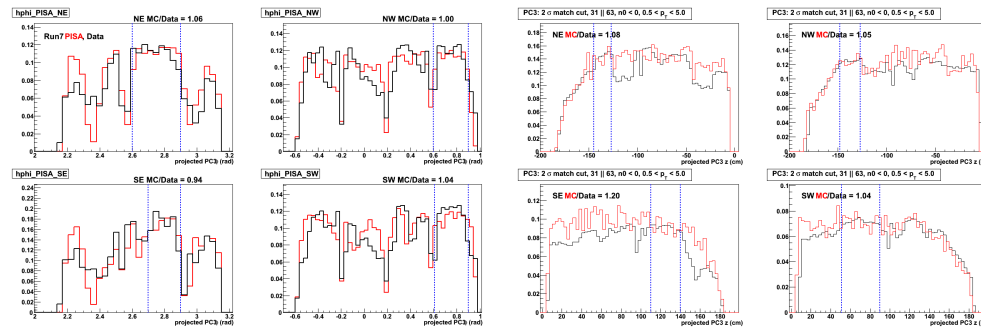


Figure 4.6: Same as figure 4.5, but for Run 7.

	MC/RD acceptance \times efficiency agreement		
	2D	$\phi \times z$	average
Run 6	1.09 ± 0.054	1.137 ± 0.056	1.114 ± 0.055
Run 7	1.08 ± 0.055	1.097 ± 0.043	1.090 ± 0.049

Table 4.1: MC/RD agreement from the 2D and $\phi \times z$ methods and their average. The arithmetic average was used to compute the uncertainty rather than the std. dev. of mean approach, which gives a slightly more conservative estimate. The two methods provide consistent results well within the 1σ level for both Runs.

effectively a correction to a correction, since the Monte Carlo acceptance \times efficiency values are divided by these factors to bring them into agreement with the data.

4.1.6 Evaluation

Once the PISA hits are reconstructed and (n)DSTs are produced, the relevant variables are extracted, and all relevant cuts are applied to the reconstructed tracks. The ratio of the number of reconstructed tracks and those originally generated is evaluated to provide the SPC. The GEANT p_T spectrum is weighted by a power-law shape obtained from a fit to the data in order to simulate p_T -dependent effects such as momentum resolution. The effect of some different analysis cuts on the efficiency can be seen in figure 4.7. The efficiencies are lowest at low momentum, where multiple scattering

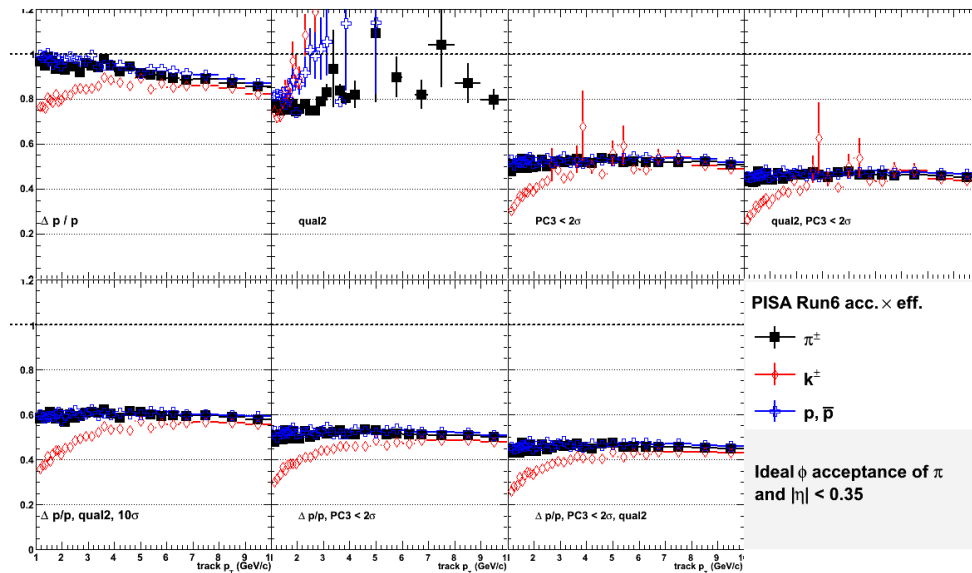


Figure 4.7: Efficiencies of various cuts applied in the analysis for the three particle types in Run 6. The figure shows that the largest contributor to inefficiency is the PC3 match requirement. The result for the Run 7 simulation (not shown) describes very similar features.

causes a significant degradation in the tracking. The trend is enhanced for the kaons at low p_T , due to the high rate of off-vertex decays. The efficiency curves for the three types are combined as described in the next section.

4.1.7 Combining particle species

It is well known that the unidentified charged hadron spectrum is almost completely dominated by pions, kaons, and (anti)protons. Each species does not have identical behavior in the detector; in particular, the k^\pm mesons suffer a significant rate of in-flight decays, leading to a lower efficiency than pions or protons, particularly at low momentum. It is therefore important to simulate each species and combine the result with a weighting representing a realistic contribution of each type. Fortunately these ratios have been measured by PHENIX [15] and others at RHIC. See figure 4.8. The primary influence on the centrality dependence of the particle mix is thought to

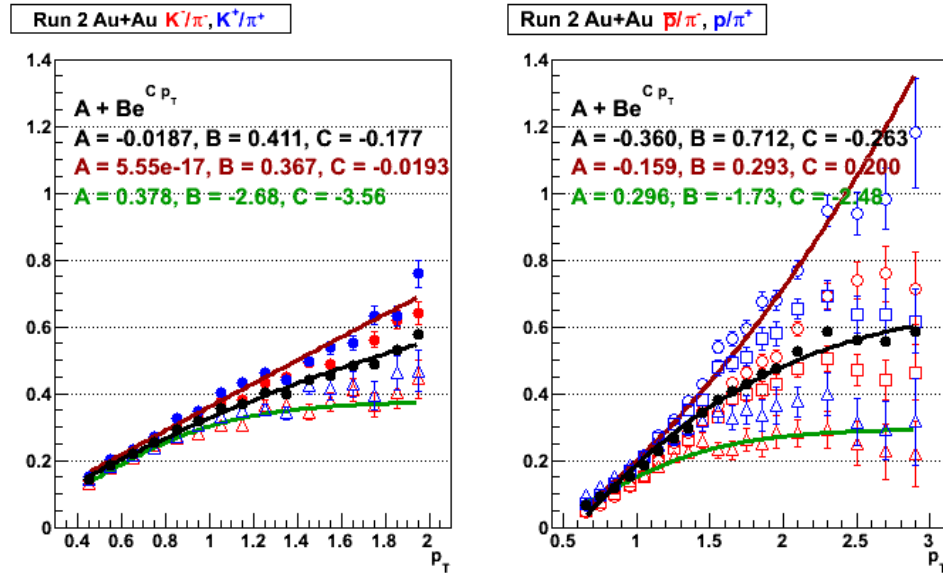


Figure 4.8: Measured kaon/pion and proton/pion ratios measured by PHENIX during the 2002 running period [15]. The black curve is a fit to the average over centrality bins and charges, while the green curve is a fit to the 60-92% bin as a proxy for p+p.

be recombination [49], accounting for the differences in with centrality in figure 4.8. Since no measurement for the p+p data was found over the needed momentum range, Au+Au peripheral data was taken as an estimate. This approximation is factored into the systematic uncertainty applied for the efficiency correction, as explained later in this chapter. Since the particle mix data is limited to low momentum by the time-of-flight

resolution and statistics, the mix ratios must be extrapolated above the data limit of 3 GeV/c.

Since the SPC is intended to represent minimum bias centrality, the centrality spread in the PID mix must be accounted for in the systematic uncertainty. This is done in figure 4.9, where curves are fit to the difference in the particle ratios between different centralities as a function of p_T . Fortunately, the PID dependence of the efficiencies decreases with increasing momentum at a higher rate than the centrality difference increases, so that the uncertainty due to the centrality spread never becomes large. This phenomenon also fortuitously protects against large uncertainties developing from extrapolation of the particle ratios above their measured limit of 3 GeV/c. Above that value, the efficiencies are almost identical for the different particle types, rendering the particle ratios in that region unimportant.

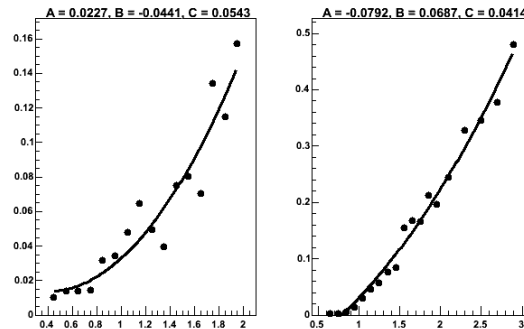


Figure 4.9: Differences between the high (central) and low (peripheral) k/π (left) and p/π ratios (right), **cf.** figure 4.8. The curve is a second-order polynomial fit, whose coefficients are shown on the plots. The curves values are multiplied by the efficiency difference between the species. The efficiency differences decrease with p_T at a similar rate that the PID ratios diverge, such that this uncertainty never exceeds about 3%.

4.1.8 Systematic uncertainties for single-particle efficiency correction

The dominant source of systematic error is currently the uncertainty from the acceptance correction as described in that section. Other sources contribute at a non-

negligible level when combined in quadrature, depending in some cases on p_T . The contributions are summarized in table 4.2.

	SPC systematic uncertainties (%)					
	MC/RD correction	SPC stat. error	Particle ratios	momentum resolution	PC3 match & recalibration	total (maximum)
Run 6	5.5	< 1	< 3	2	3	7.6
Run 7	4.9	< 1	< 3	2	3	7.4

Table 4.2: Breakdown of single-particle acceptance \times efficiency corrections for Runs 6 and 7. The total uncertainty is roughly the quadrature sum of all contributions, but is calculated directly for p_T -dependent quantities. The table entries provide typical values or approximate upper bounds for each contribution.

4.2 The bootstrap method as a cross-check

The so-called bootstrap method is simple in its implementation: a single-particle spectrum is produced from the analysis dataset with all cuts applied, then the acceptance \times efficiency is given by its ratio to a fully-corrected spectrum from another analysis. Provided that the reference spectrum is correct and consistent acceptance definitions are used, this method should yield the same correction value as a Monte Carlo simulation.

Given that this provides a valuable cross-check, the specific implementation is described here for the p+p data, which does not have the additional complication of requiring the occupancy correction and has a smaller background. A published reference spectrum for the p+p data is given by the h^\pm cross-section in [16]. This is proportional to the invariant yield (IY) through the p+p inelastic cross-section at full RHIC energy, 42 mb. The invariant yield is defined as

$$IY = \frac{1}{N_{evt}} \frac{1}{2\pi p_T} \frac{d^2 N}{dp_T d\eta} \quad (4.5)$$

where $N = (h^+ + h^-)/2$. The analysis spectrum is binned in counts ($= N$) per event,

per p_T bin. The efficiency is then calculated as

$$\epsilon = \frac{N/(N_{evt}\Delta p_T)}{1/\epsilon_{trig} \times c_{fd} \times 2\pi p_T \times \int d\eta \times 1/2 \times IY} \quad (4.6)$$

The adjustments required in the denominator are listed as follows:

- The trigger efficiency, 0.69, was applied to IY and must be removed to make the comparison.
- A factor to correct for the feed-down contribution from the decay of heavier hadrons of $c_{fd} = 1/1.07$ was also applied, requiring removal.
- $2\pi p_T$ is the phase space factor required for invariance.
- The η dependence is very nearly constant over the central arm acceptance, so $\int d\eta = 0.7$ for the ideal acceptance.
- Since the ideal azimuthal acceptance was chosen to be π , rather than 2π , for the MC efficiency calculation, the $1/2$ is required for comparison.

This ratio is calculated for inclusive tracks, i.e. those not requiring a trigger particle. Because of this, the high- p_T background seriously contaminates the spectrum, limiting the range usable for comparison to about 3 GeV/c and below. The result of this efficiency, which overlays the MC single-particle efficiency, is shown in figures 4.10 and 4.11 for Runs 6 and 7, respectively.

4.3 Occupancy efficiency

The occupancy efficiency is calculated in a simulation designed to isolate the effects from high-occupancy conditions on the reconstruction. The simulation uses the same single-MC tracks that were generated for the SPC study, but embeds them in a background of hits recorded in real Au+Au data. Merging routines keep track of the

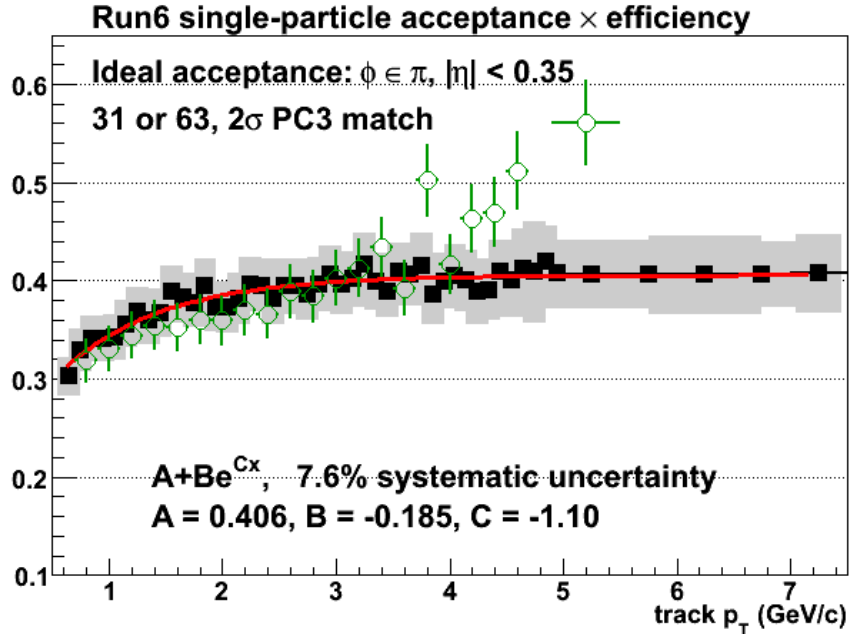


Figure 4.10: Single-particle acceptance \times efficiency curves for Run 6 p+p. The dark points depict the PISA result and the grey band represents the uncertainty whose contributions are listed in table 4.1. The green points represent the efficiency obtained through the bootstrap method. Agreement is found within 5% in the low-background region below 3GeV/c, well within 1σ in the uncertainties.

hits from MC, RD, and the combined set for each subsystem, and the full offline track reconstruction is performed on **both** the single monte carlo **and** the merged hit data.

The specific routine for calculating the occupancy efficiency involves a “principal contributor” analysis using the drift chambers. Since the source of every hit is stored, it can be determined forensically whether a track was reconstructed primarily from real or GEANT hits. Specifically, one source must contribute at least half of the hits that compose the track in order to receive a status as the primary contributor.

At this point it is necessary to distinguish three different categories of tracks:

- Type “G” tracks are the original MC particles initially input into the GEANT simulation that interact with the material, and have well-defined position, momentum, particle ID, ancestry information, etc. They can include secondary

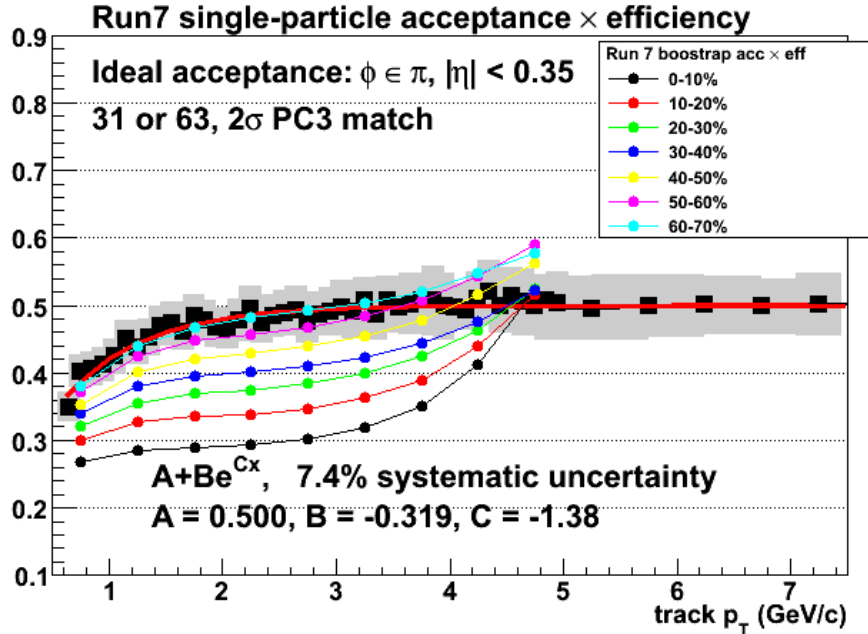


Figure 4.11: Same as figure 4.10, but for Run 7. Again, the bootstrap curves agree closely with the PISA result in the peripheral range, where occupancy effects do not play a role. Such effects are handled in section 4.3.

tracks that were produced by decay or conversion in the detector material during the simulation. They are stored if they are found to be a principal contributor to a reconstructed track.

- Type “S” tracks are the single MC tracks reconstructed in the absence of the real-data background. They are essentially identical to those produced to calculate the SPC. GEANT particles are always the principal contributor to these tracks, because there is no other source.
- Type “R” tracks are the result of reconstructing the MC tracks which have been embedded in real data. The extra hits cause a reduction in track quality due to merged or unassociated hits, and throw off the reconstruction with increasing severity as the background multiplicity rises. Either real or GEANT tracks may be principal contributors to type R tracks.

When a hit produced by a GEANT track (e.g. a particular DC wire) is found to be in the same spatial location as a real data hit, it must be decided whether to attribute the shared hit to RD or MC. In such shared-hit cases, the timing information from the ADC pulses is used. Specifically, the leading times are compared, and the earlier time wins.

4.3.1 Details of the study

The embedding efficiency is evaluated as the ratio of R/S tracks, with all analysis cuts applied to both types of tracks. In this way, the single-particle efficiency effects cancel, isolating the occupancy effects. Each track type has its own set of variables. While S tracks must satisfy S cuts in order to survive in the denominator, both R and S tracks must pass their respective cuts in order for R tracks to contribute to the numerator for a correct accounting of the efficiency. The following cuts were applied:

- The original GEANT source tracks must be first-generation (no decay or conversion products)
- At least two X1 and two X2 hits are required in the DC, with a track quality of 31 or 63.
- 2σ radial PC3 match. The matching distributions require recalibration as for the single-particle case.

The matching distributions were recalibrated in bins of charge, centrality, and momentum for both type S and type R tracks. For each bin, the raw PC3 $\Delta\phi$ and Δz distributions were fit with a single Gaussian function. The parameters and errors were extracted and fit as a function of momentum with the form of eq. 4.4. In appendix E, the raw matching distributions are shown in figures E.1 and E.2 and the p_T dependence of the means and widths is shown in figure E.5.

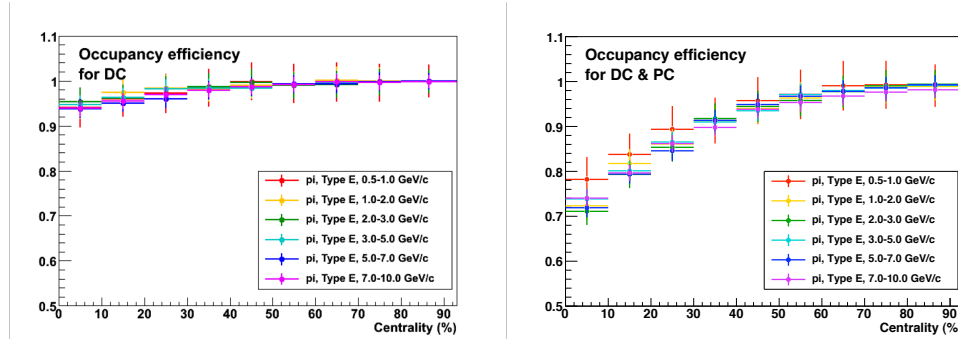


Figure 4.12: Embedding efficiency vs. centrality for the DC only (left) and for the DC with PC3 match requirements (right) for charged pions, demonstrating that the PC3 is the dominant source of occupancy inefficiency.

4.3.2 Run 7 results

The results of the occupancy efficiency are shown in figure 4.12 as a function of centrality for the drift chamber only, and for the DC tracks requiring a PC3 match. This illustrates that the inefficiency is dominated by PC3 occupancy effects. As expected, the efficiency drops with increasing track multiplicities. It was found in the course of the study that while the species dependence is important in the single-particle efficiency, it is smaller than the current statistical uncertainty in the occupancy correction, so the π^\pm results are applicable for all species. Figure 4.13 shows the efficiencies resulting from a centrality-weighted bin combination, and the fits applied to impart a smooth correction to the data. The occupancy efficiency is well approximated as a constant value above 1 GeV/c, but rises in the 0.5-1 GeV/c range. This is due to the fact that a fixed 2σ PC3 matching window corresponds to a larger $\Delta\phi \times \Delta z$ area at low p_T , as can be seen in the matching width recalibration plots in appendix E. Although no points are shown below 500 MeV/c, the track bend increases sharply as p_T drops, resulting in longer tracks and higher hit-merging probabilities, and consequently an expected decrease in occupancy efficiency. Thus the 0.5-1 GeV point is more of a bump than a point in a monotonic rise with decreasing p_T .

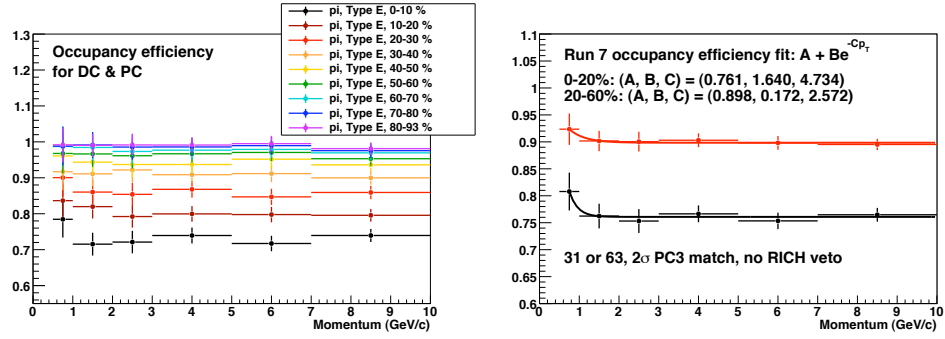


Figure 4.13: Embedding efficiency vs. momentum for 10% centrality bins (left) and for the combined centrality bins used in this analysis (right).

4.3.3 OEC cross-check and systematic uncertainties

As a cross-check of the of the embedding results, the centrality dependence of the inclusive spectra was checked in a manner analogous to the bootstrap method. The goal was to compare whether the centrality dependence of the raw spectra, with the occupancy correction applied, agrees with that of an earlier Au+Au result published in [17]. The result is shown in figure 4.14. Although the centrality dependence is

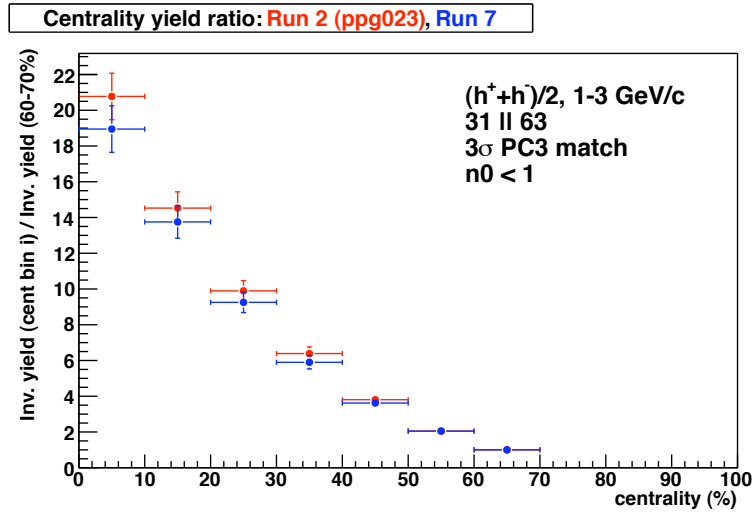


Figure 4.14: Centrality dependence of fully-corrected PHENIX unidentified h^\pm spectra from Run 2 as published in [17] (blue) and raw data from this analysis with the OEC from this study applied (red). The 60-70% centrality category is used as a reference, and the yield in each centrality bin compared to the reference is plotted.

systematically smaller than in the published result, the comparison method is not highly precise, since the peripheral reference carries significant statistical uncertainty and the ratio of the centrality bins is not independent of the normalization of the spectra. However, the agreement is quite reasonable within the uncertainties of the study. The cuts applied in this comparison are different than those of the analysis, but since the cuts are consistent within the study (i.e. the correction matches the raw spectra) the validity of the comparison is not diminished.

The uncertainty of the embedding efficiency correction is estimated to be 5% of the correction value. The primary sources of uncertainty are statistical error, potential misalignments in the simulation geometry between the real-data and GEANT hits, and any propagation of the PC3 matching recalibration uncertainty. The geometry mismatch is known not to be large, and its effect on the occupancy efficiency is probably negligible, since the mere presence of real background hits is by far the important feature compared to their alignment in the precise locations. Most of the uncertainties in table 4.1 cancel, since both type R and S undergo reconstruction through the same framework. The PC3 recalibration uncertainty experiences some degree of partial cancellation, since the embedding efficiency depends on the PC3 matching window size, but on the other hand, both R and S tracks are required to satisfy the match cut. Therefore, given that the SPC errors are about 7% for Au+Au, and are dominated by the MC/RD correction (which has no bearing on the occupancy; moreover, many of the other contributions at least partially cancel), a 5% occupancy efficiency error is judged as appropriately conservative.

Chapter 5

Results and their uncertainties

This chapter describes the conditional jet yields obtained from the correlation functions, as well as the quantities derived from these yields. The following chapter discusses the interpretation and implications of these results.

5.1 Conditional jet pair yields

The conditional jet yields per trigger particle, or per-trigger yields (PTY) are obtained from the correlation functions, which are included in appendix F. The connection between the two was made in chapter 1, and given by equation A.9. In a more explicit form,

$$\frac{1}{N_{\pi^0}} \frac{dN_{pair}}{d\Delta\phi} = \frac{N^{h^\pm}}{2\pi\epsilon^{h^\pm}} \left[\frac{dN_{same}/d\Delta\phi}{dN_{mix}/d\Delta\phi} - \xi \left(1 + 2\langle v_2^{\pi^0} v_2^{h^\pm} \rangle \cos 2\Delta\phi \right) \right]. \quad (5.1)$$

The background level is given by ξ for each bin in tables 3.1 and 3.2. As discussed in 3.2.2, the pair quadrupole anisotropy is assumed to factorize during the subtraction such that $\langle v_2^{\pi^0} v_2^{h^\pm} \rangle \approx \langle v_2^{\pi^0} \rangle \langle v_2^{h^\pm} \rangle$. The pair v_2 values are listed in tables 3.4 and 3.5. The efficiency is given by the single-particle efficiencies calculated from simulations (figures 4.10 and 4.11). For Au+Au, the occupancy efficiency is also included, so that $\epsilon^{h^\pm} = \epsilon^{SP} \epsilon^{occ}$.

The PTYs are shown for all trigger and partner p_T bins in figure 5.1 for p+p, and in figures 5.2 and 5.3 for Au+Au. The statistical precision is very high in the

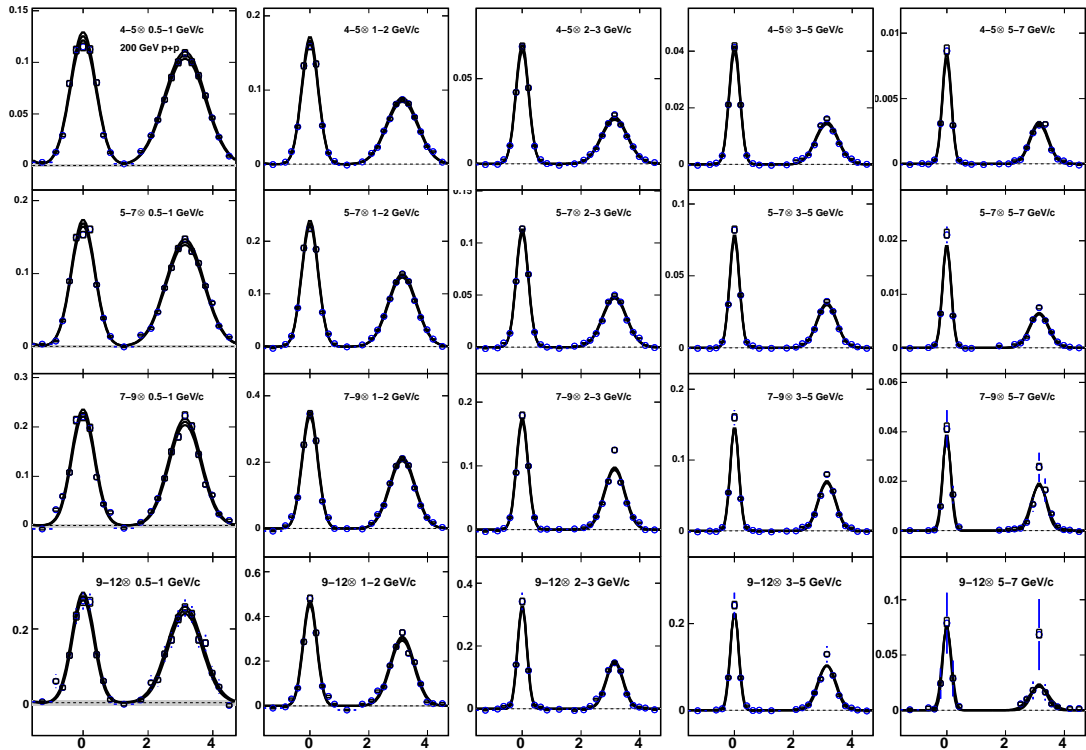


Figure 5.1: p+p conditional jet yields per π^0 trigger particle. The boxes represent all type B uncertainties included described in this section, and the grey band shows the ZYAM uncertainty. There is an additional type C uncertainty of 7.6% from the ϵ^{h^\pm} correction.

p+p data for three primary reasons. First, the high RHIC luminosities for p+p provide many more collisions over the running period than in Au+Au, since its charge to mass ratio is higher; secondly, the ERT triggering employed in Run 6 enabled a very effective enhancement in the selection of hard-scattering events, whereas the luminosities were low enough relative to the DAQ throughput rates in Run 7 to take data without triggering. Finally, the particle multiplicities in p+p events are so much lower than in Au+Au that the correlated jet signal is much more pronounced over the uncorrelated (or weakly-correlated) background in a typical event.

Each plot includes three fits of a form consisting of Gaussian peaks for the near

and away side

$$\begin{aligned}
 f(\Delta\phi) = & A_n \exp[-\Delta\phi^2/2\sigma_n^2] + A_a \exp[-(\Delta\phi - \pi)^2/2\sigma_a^2] + \\
 & A_a \exp[-(\Delta\phi + \pi)^2/2\sigma_a^2] + A_n \exp[-(\Delta\phi - 2\pi)^2/2\sigma_n^2]
 \end{aligned}
 \tag{5.2}$$

where the additional peaks centered at $-\pi$ and 2π are included to maintain periodic continuity. The three fits correspond to the measured value and its 1σ high and low systematic uncertainties, which will be discussed later.

Several features are worth noting in the p+p correlations, which are important to understand, given that they are the reference for the Au+Au data. First, the widths of the jet peaks are, in most cases, well described by a Gaussian form, and become narrower with increasing p_T . The narrowing effect depends more strongly on partner p_T than on trigger p_T . This can be understood by the kinematics of the in-vacuum jet fragmentation: as the parton velocities increase, the momenta of their hadronic fragments in a direction transverse to the jet axis is not significantly altered, but the longitudinal component receives a Lorentz boost that leads to a narrowing of the jet cone.

However, in azimuthal correlations, this transverse momentum from fragmentation is only one effect that contributes to the total width of the jet peaks. Another notable source of broadening is initial-state k_T arising from fermi motion of partons within the colliding protons. When this is included, conservation of momentum in the transverse plane dictates that the outgoing partons in a $2 \rightarrow 2$ hard-scattering process are not back-to-back in general due to the transverse kick. There are indications that the effect is sizable. For example, in order to produce the widths shown in these plots in the PYTHIA generator for RHIC energies, PHENIX pseudorapidity acceptance, etc., it is necessary to tune the mean initial-state parton k_T to 2.5-3 GeV/c [13].

Other higher-order QCD and QED processes may also contribute to the broadening of jets, since any QCD radiation from the partons in either the initial state results in gluons that will ultimately fragment, and these higher-order effects may have

a non-negligible degree of angular correlation with the harder components of the jet. An understanding of the underlying event [3] may provide more information about the nature of these higher order effects and their contribution to jet correlations.

A more trivial feature visible in figure 5.1 is the reduced away-side amplitude in comparison to the near side. This is a pair acceptance effect, combined with the asymmetry in momentum fraction x between the initial partons. When the initial partons have large differences in their longitudinal momenta, the jet axes depart widely from an antiparallel orientation in polar angle. A triggered dihadron coincidence essentially always captures some portion of the near-side jet by construction, but the central-arm pair acceptance in $\Delta\eta$ is limited to roughly ± 0.7 units, so that the longitudinal momentum imbalance leads to a reduced probability for finding the opposing jet (or some substantial portion of it).

Finally, the conditional jet yield per trigger particle is seen to decrease with partner p_T , but this decrease is not nearly as sharp as observed for inclusive particles.

5.2 Systematic uncertainties on conditional yields

The conditional yields carry a systematic uncertainty propagated from several different sources, which are taken to be independent except where noted. The assumption of independence is simpler and more conservative than the alternative of attempting to estimate the degree of correlation between the sources.

The nature of the uncertainties is classified by dividing into three categories, following the terminology used in [6]: Type A systematic uncertainties are uncorrelated from point to point, and can justifiably be combined in quadrature with statistical errors due to their independence (although that is not done here). Type B uncertainties are fully correlated from point to point, but their magnitude is not generally the same among points. Type C uncertainties are fully correlated point-to-point, and are applied to each point as a uniform multiplicative factor.

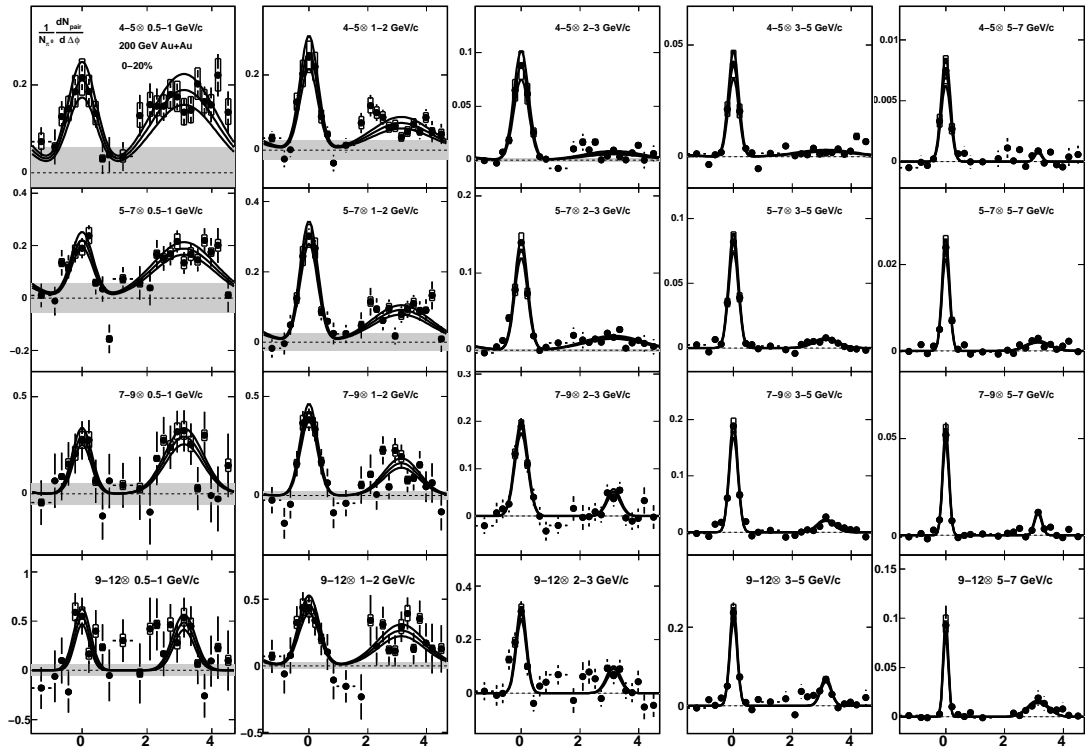


Figure 5.2: Au+Au conditional jet yields per π^0 trigger particle for 0-20% collisions. The boxes represent all type B uncertainties included described in this section, and the grey band shows the ZYAM uncertainty. There is an additional type C uncertainty of 8.85% from the e^{h^\pm} correction.

The A, B, or C classification of each source is not always entirely straightforward, since the behavior of the uncertainties depends not only on the error source but on the measured quantity and the independent variable it is measured against. Given these considerations, the error sources are described here.

5.2.1 π^0 combinatoric background (type B)

A contribution to the PTYs due to falsely reconstructed π^0 s under the mass peak can be estimated as follows: if the measured PTY, Y_m , is a sum of a signal and a background component,

$$Y_m = \frac{s}{s+b}Y_s + \frac{b}{s+b}Y_b \quad (5.3)$$

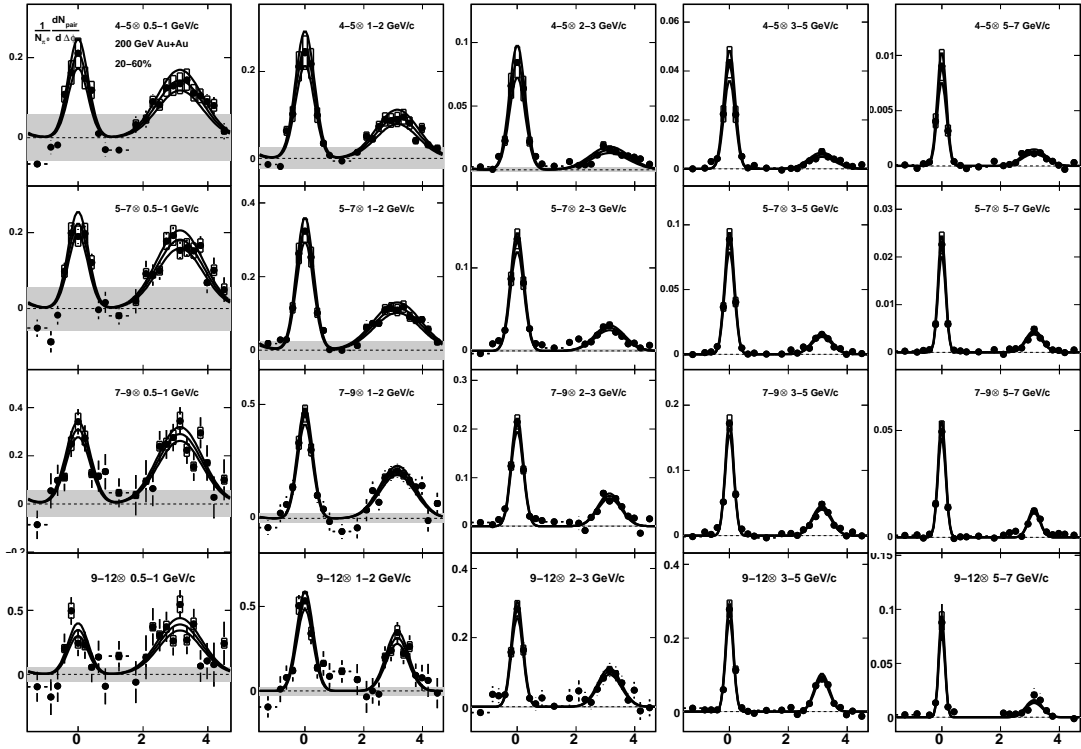


Figure 5.3: Same as figure 5.2, but for 20-60% collisions.

then two relevant limiting cases can be discussed: (a) $Y_b = 0$, and (b) $Y_b = Y_s$. In the first case, the measured result is different by the factor $s/(s+b) = 1/(1+b/s)$, so that a 20% systematic bias results from a s/b of 5:1. In the latter case, the measured yield is identical to the truth, so no systematic error is assigned, no matter how small the signal/background ratio.

By examining invariant mass regions near the π^0 peak, an estimation of Y_b can be made. This is a nontrivial task, however, as the subtraction procedure requires a knowledge of the background elliptic flow, and statistical limitations introduce additional complications in interpreting the result. In the early stages of this analysis, sideband regions (π^0 peak mass $\pm 2.5\sigma$) were examined, but a rigorously quantified result was not obtained. Because the background PTY has not been carefully measured, a systematic error is assigned based on an assumption that the per-trigger yields are

50% of the true yields, giving a relative error of $s/2b$.

There is also an error in the v_2 level due to the combinatoric background, since the v_2 is composed of signal and background components contributing in the same way as in eq. 5.3. Because the results of this analysis are restricted to relatively high trigger p_T , this error is taken to be subsumed by the error already assigned to the $\pi^0 v_2$, since the two uncertainties are likely to be correlated at some level. The uncertainties as they were applied are listed in table 5.1.

π^0 background uncertainty (%)				
$\pi^0 p_T$ (GeV/c)	4-5	5-7	7-9	9-12
p+p	2.8	2.3	2.4	2.5
Au+Au	14.3	8.3	6.4	7.9

Table 5.1: Percentage uncertainties applied to conditional yields for π^0 misidentification. The uncertainties are calculated directly from signal/background ratios determined by Gaussian fits to the invariant mass.

5.2.2 Uncertainty from v_2 measurements (type B)

The pair v_2 uncertainties are listed in tables 3.4 and 3.5. Their effect on the conditional yields is highly p_T -dependent, as is readily seen in the correlation functions. Along with the background normalization, this is a dominant source of uncertainty at low trigger and partner p_T , where the correlation strength is small, and becomes smaller with increasing p_T until it is basically negligible above 3 GeV/c in partner p_T .

5.2.3 Charged hadron background (type B)

The effect of the background on the conditional yields was estimated by comparing correlation functions with loose and strict cuts. A 2σ vs. 3σ PC3 matching cut were compared, where a RICH electron veto cut was also applied in the former case. Below partner $p_T = 3$ GeV/c, no discernible change was observed within statistical uncertainties, but the signal/background level was enhanced with the tighter cuts by

about 4% (8%) for the 3-5 (5-7) GeV/c partner p_T bins in Au+Au and 2% (4%) for the same p_T bins in p+p, so these were the uncertainties applied. This is the only error that increases in magnitude with p_T .

5.2.4 Background normalization (type B)

The ZYAM pedestal subtraction in p+p is very robust due to the excellent statistics available. Since the ZYAM level is established through a fit to $C(\Delta\phi)$, the background normalization error is taken to be the error on the background parameter b_0 from the fit. It therefore carries an uncertainty that is indirectly determined by the statistical uncertainty in the region between the peaks. This can be seen in figure F.1 to be very small even in the worst cases, never more than a few percent of the peak amplitudes. The uncertainty is propagated to the PTYs and shown as a grey band in figure 5.1.

The uncertainties for the ABS method are those propagated from the ξ determination and are given in tables 3.1 and 3.2. The magnitude of the ξ errors, like the v_2 uncertainty, does not vary widely with p_T . However, since the jet signal/background is only a few percent at low p_T and becomes much larger with increasing p_T , its propagated effect varies strongly from bin to bin. This can be seen in the PTY figures, where the grey band directly represents the tabulated background normalization errors.

5.2.5 h^\pm efficiency correction (Type C)

The single-particle and occupancy efficiency correction uncertainties apply globally on the PTY plots and are taken as independent. The combined error for Au+Au is thus the quadrature sum of the SPC and OEC errors: $7.3 \oplus 5.0 = 8.85\%$. For p+p, it is the SPC error only at 7.6%.

The total uncertainty from the type B contributions, with the exception of the background normalization, is evaluated by the following procedure:

- (1) In the Au+Au case, the background subtraction is performed for the measured pair v_2 value as well as its 1σ high and low values. The propagated flow uncertainty is then provided by the variation in the subtracted results.
- (2) The background-subtracted jet function is normalized to become the PTY.
- (3) The π^0 and h^\pm background errors are applied multiplicatively to the high and low values (heretofore equivalent in p+p), such that the high values are scaled upwards and the low values are scaled down. The result is represented by open error boxes to distinguish from statistical errors. The background normalization and efficiency correction errors are handled separately.

The fact that three of the five error sources above monotonically reach their maximal values with decreasing π^0 and $h^\pm p_T$ is clearly visible in the PTY plots. The propagation of these uncertainties to derived quantities will be discussed in the relevant sections.

5.3 Extracting jet shape information from conditional pair yields

A variety of observables have been used to quantify jet peak shapes in correlations data, but one of the most common is the σ value from a Gaussian fit [13, 7, 4]. This tends to work well for quantifying widths in p+p and in some cases A+A, but loses applicability as nuclear effects enter. Although it is a reasonable starting point to assume that the distribution of fragmented hadrons is random about the jet axis and therefore approximately Gaussian, a combination of nontrivial physical effects coupled with the act of projecting into $\Delta\phi$ can easily lead to more complicated shapes. Nevertheless, the intuitive simplicity of using a single, well-defined, versatile variable such as σ from a fit has significant value, particularly given that there are already a small number of results available in the literature for comparison.

Gaussian widths were extracted for both the near and away side from fits applied

to each PTY over the full azimuthal range. The fit form is given by equation 5.2, and the fits are included in the figures. The result is shown in figures 5.4 and 5.5.

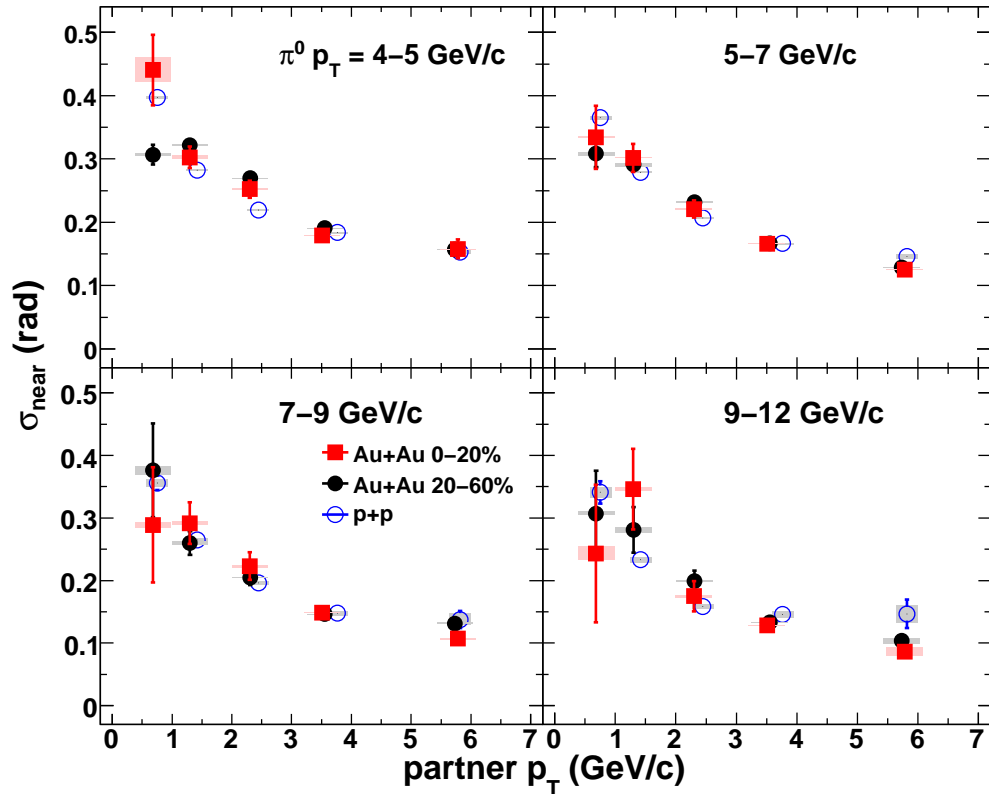


Figure 5.4: Near-side σ fit parameters vs. $h^\pm p_T$.

On the near side, close agreement is found between p+p and both Au+Au centrality categories. In comparable p_T intervals, the values agree with earlier p+p measurements from PHENIX [13, 7]. The falling trend is well-described by a simple exponential form with a constant offset included.

The away-side fits show consistency within uncertainties between Au+Au and p+p at $\pi^0 p_T > 7$ GeV/c for all partner p_T . The STAR collaboration has measured a consistent width in this range for dihadron correlations in 0-5% Au+Au, quoting a Gaussian width of 0.22 ± 0.02 radians in $\Delta\phi$ for 8-15 GeV trigger particles and partner $p_T > 6$ [4].

At lower $\pi^0 \otimes h^\pm p_T$ the fits are not well described by a Gaussian shape, as shown in figure 5.5. The widths were obtained by applying Gaussian fits to the away side with every σ value from 0 to $\pi/2$ in steps of 0.01 radians. The minimum total χ^2 is evaluated from the fitting routine for each step, allowing a determination of the

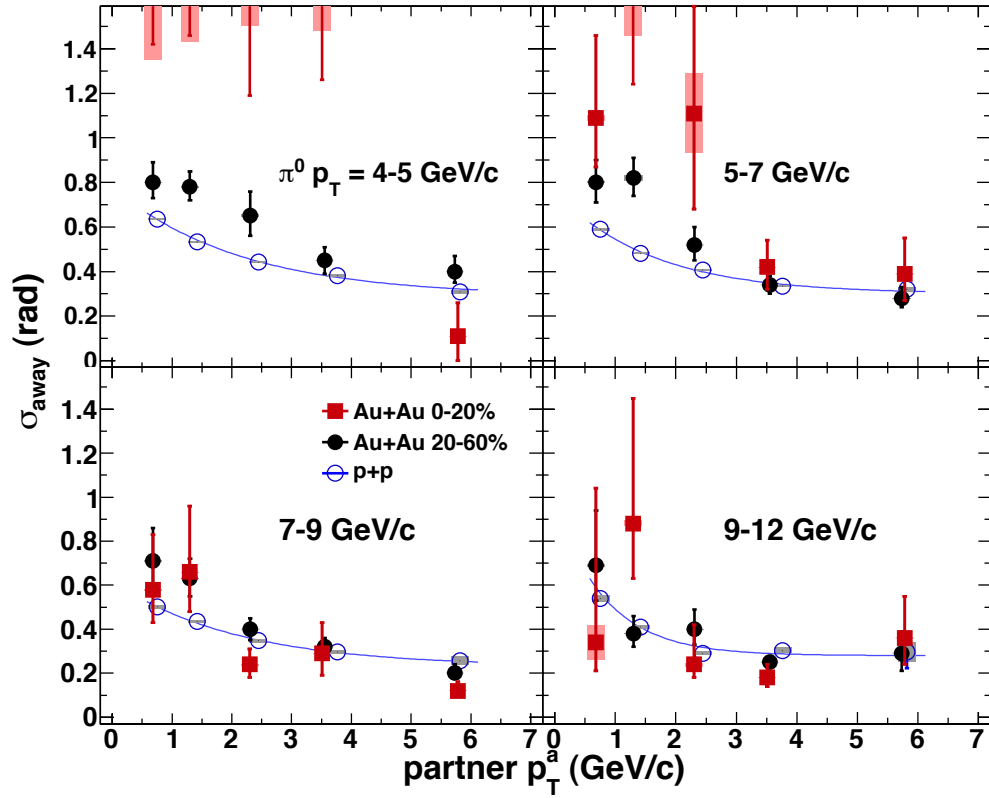


Figure 5.5: Away-side σ fit parameters vs. $h^\pm p_T$. The points at the upper bound in the top panels represent Gaussian fits whose best total χ^2 value corresponds to $\sigma > \pi/2$.

best-fit σ value for each bin. In several bins at low p_T , the minimum χ^2 value continues to fall monotonically with increasing σ beyond the full width of the away side region, reflecting the disagreement between the data the hypothesis of a distinct single peak. As p_T is increased, the data become well-described by a single Gaussian peak whose width steadily decreases.

To quantify this transition further, a study was performed in which the Au+Au PTYs were re-fit using the same form, but the widths were fixed at the p+p values, leaving the normalization as the only free parameter for each peak. This provides a simple hypothesis test to measure how well the Au+Au shapes agree with p+p as a function of p_T . The result is shown in figure 5.6. The test demonstrates that the goodness-of-fit is roughly uniform over the full trigger and partner p_T ranges on the

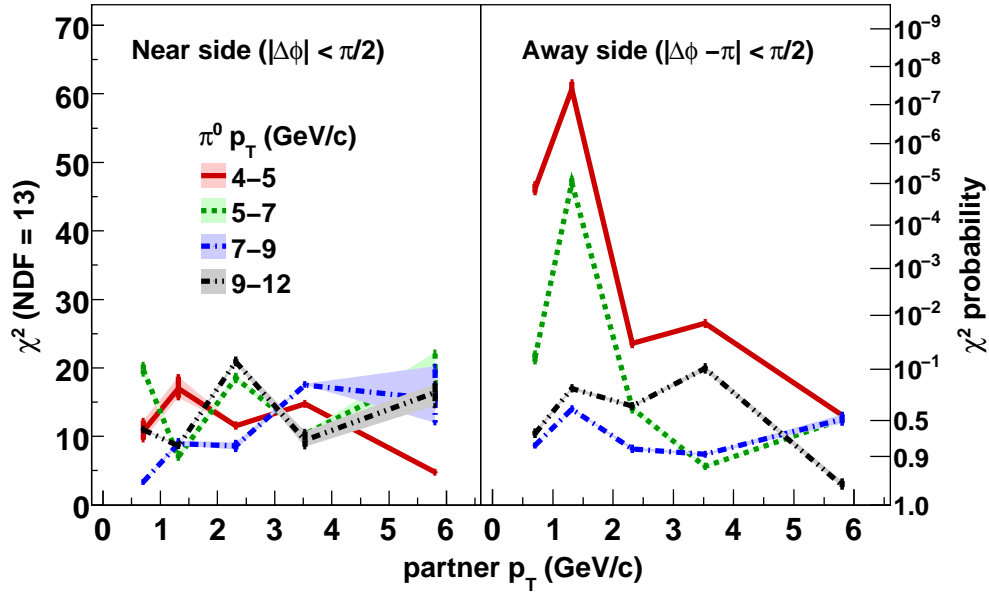


Figure 5.6: χ^2 and their corresponding p -values for Gaussian fits to 0-20% central Au+Au conditional yields. The fits were performed on p+p first, then the widths were extracted for use as a fixed parameter on the Au+Au fits.

near side; no discernable dependence is found. However, the quality of the fits is only mediocre for most bins, with p -values dipping into the 1% range in several cases.

One explanation for this behavior at low p_T is that it is the faint indication of a non-Gaussian shoulder-like component known as “the ridge”, which has been observed in many recent analyses and is particularly prominent in $\Delta\phi \times \Delta\eta$ correlations [1]. The ridge feature becomes obscured in the projection into the azimuthal plane, but given the clear indications of its presence in comparable p_T ranges, it stands to reason that it makes some non-Gaussian contribution to the near-side shape.

At higher p_T , the near side peak takes on a very narrow fragmentation shape, and is not as well approximated by a single Gaussian form. Although not shown here, the goodness of fit values obtained for the p+p data used to set the reference widths have the same problem. A compound-Gaussian form was used as a cross-check of the test, and although it improved the χ^2 values for p+p, the corresponding fits did not improve significantly for Au+Au.

On the away side, the same behavior is observed as for the near side for the two highest trigger p_T bins. For the lower two trigger pt bins, however, the fit quality drops conspicuously at partner $p_T < 2$ Gev. This provides a consistent picture with that described by the width plots; specifically, the jet shapes become highly non-Gaussian below this transition region. Interestingly, in the lowest partner p_T bin, the χ^2 comes back down again. Three explanations can be offered for this behavior: (a) p+p gets broader there too, closer to the Au+Au shape. (b) An inherent feature of the χ^2 test is that distributions with poor statistics give closer agreement in general to hypothesis curves than more well-sampled distributions, and since the jet signal to background ratio decreases sharply with p_T , this effect comes into play. (c) Perhaps most interesting from a physical perspective, note in figure 3.19 that the elliptic flow strength drops steeply with p_T from 2-2.5 GeV/c downward. The smaller subtracted flow component leads to a jet peak that really is more Gaussian. Thus the trend towards a more amplified bimodal shape with decreasing p_T is not monotonic, but in fact reverses at the lowest momenta. In a future analysis with higher statistics, it would be highly desirable to map out this trend in finer partner p_T bins and determine how the non-Gaussian deviations evolve within this interval.

5.3.1 Other shape parametrizations

Additional measures of the jet shape and width were carried out, including the RMS width of the jet peak, defined as

$$\Delta\phi_{RMS} = \sqrt{\frac{1}{\sum_j n_j} \sum_i n_i \left(|x_i - \mu| + \frac{\Delta x}{\sqrt{12}} \right)^2} \quad (5.4)$$

where x_i is the center of $\Delta\phi$ bin i , and n is the conditional yield in each bin.

This parameter has the advantage of being independent of any assumption about the jet shape, providing a uniformly-defined measurement for any distribution. However, the quantity suffers from sensitivity to fluctuations far from the mean, and does not

account for their (lack of) statistical significance. In the PTYs of this analysis, these properties led to systematic disagreements compared widths obtained from the Gaussian fits, with a sensitive dependence on the boundary of the angular region, even when no statistically significant jet signal is present. For these reasons it was decided not to include this measure in the final results.

Another shape variable of potential interest is the ratio of the jet yield in the narrow “head” or punch-through region ($|\Delta\phi - \pi| < \pi/6$ rad) to that in the full away side, excluding the head region. For correlations at lower p_T , this variable is an informative description of deviation from a single-peak structure. However, it is poorly defined for sharp peaks when the “shoulder” region in the denominator is close to zero. The p_T dependence of this quantity was examined, and although it provided some useful quantitative information in the medium-modified regime, it was ultimately excluded from the final results due to its lack of stability through the full partner p_T range, particularly for the statistically-limited 7-9 and 9-12 trigger p_T bins.

These additional methods of quantifying the jet shapes through the full momentum range present essentially the same message as the fit studies communicate, and there is only modest additional quantitative gain from their inclusion in the analysis.

5.4 Integrated yields and I_{AA}

The fully corrected conditional spectra were measured for the near and away side regions, as shown in figures 5.7 and 5.8. The same quantity was also calculated for a narrower punchthrough $\Delta\phi$ window and is not shown. A comparison between Au+Au at the two centralities and p+p is made more explicitly through the I_{AA} variable, defined in equation 1.25. I_{AA} calculations from the ACHNS [25] and ZOWW [74] models are also shown in Figure 5.10. Both calculations include a parton energy loss formalism with a particular modeling of medium geometry. The ACHNS calculation uses a hydrodynamic evolution model of the medium and an energy loss scheme employing

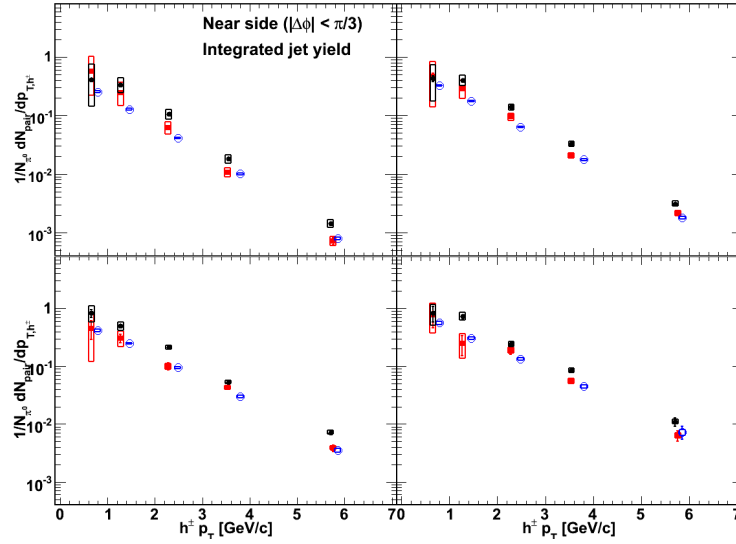


Figure 5.7: Near side integrated conditional yields vs. partner p_T . The blue, red, and black points are p+p, 0-20% central Au+Au, and 20-60% central Au+Au.

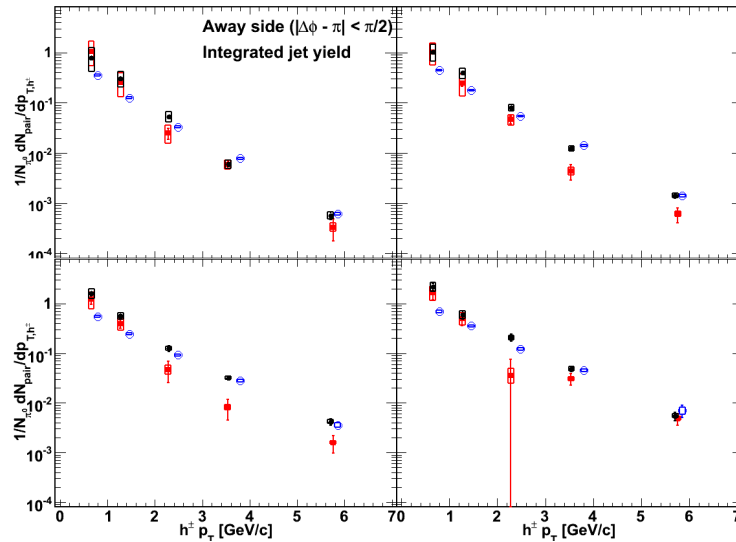


Figure 5.8: Same as figure 5.7, but for away side. The blue, red, and black points are p+p, 0-20% central Au+Au, and 20-60% central Au+Au.

quenching weights obtained through fits to other data as described in [25]. The ZOWW calculation also uses energy loss parameters from fits to other data, but models a static spherical geometry. The unique geometries used makes it difficult to evaluate whether the medium profile or the energy loss mechanism used in each model is responsible for

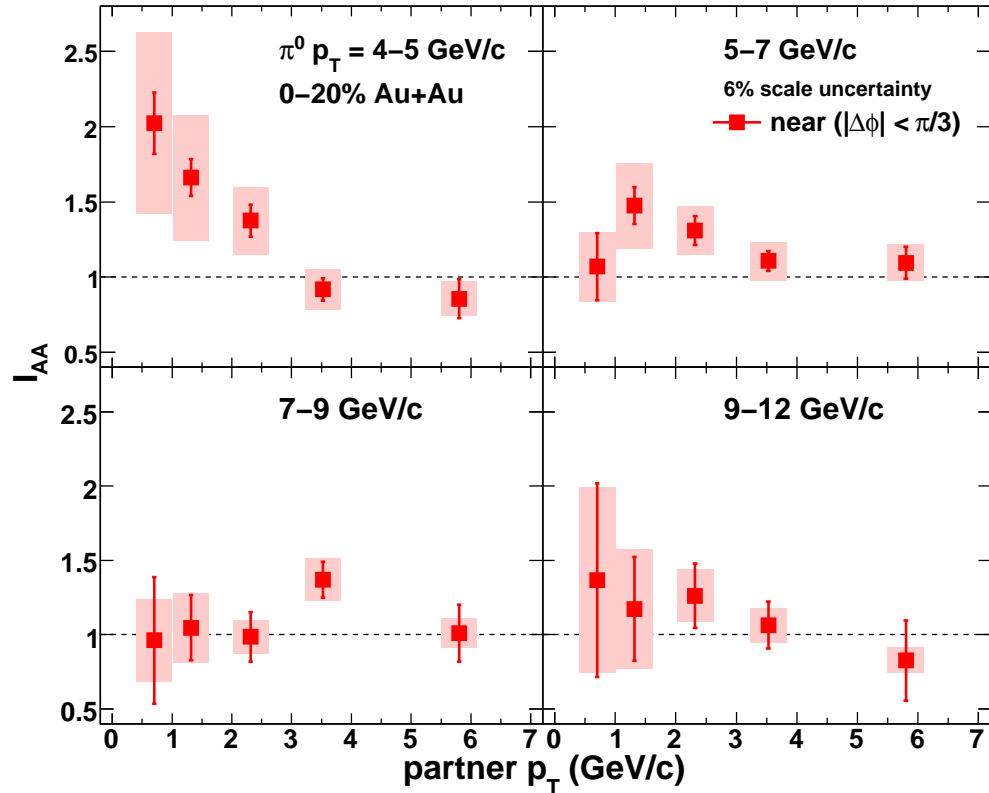


Figure 5.9: I_{AA} vs. partner p_T for the near-side jet angular integration region.

the differences in the results. However, the ZOWW calculation does predict that $I_{AA} > R_{AA}$, in general agreement with the data, while ACHNS predicts that $I_{AA} \lesssim R_{AA}$. The fact that this data is sufficiently precise to favor the ZOWW calculation is intriguing; however, the comparison would be more compelling if both models were to incorporate the same medium geometry profiling for a direct discrimination between the energy loss component of the calculations.

The trend in I_{AA} as being consistently higher than R_{AA} is unsupportive of a naive scenario where the surface bias from selecting high-momentum trigger particles creates a tendency for the recoil jet to pass through a large portion of the medium and suffer greater suppression than for untriggered single-particle cases. However, a significant competing effect arises from the steeper slopes of the untriggered yields compared to conditional pair yields. Since R_{AA} is composed from softer spectra than the conditional

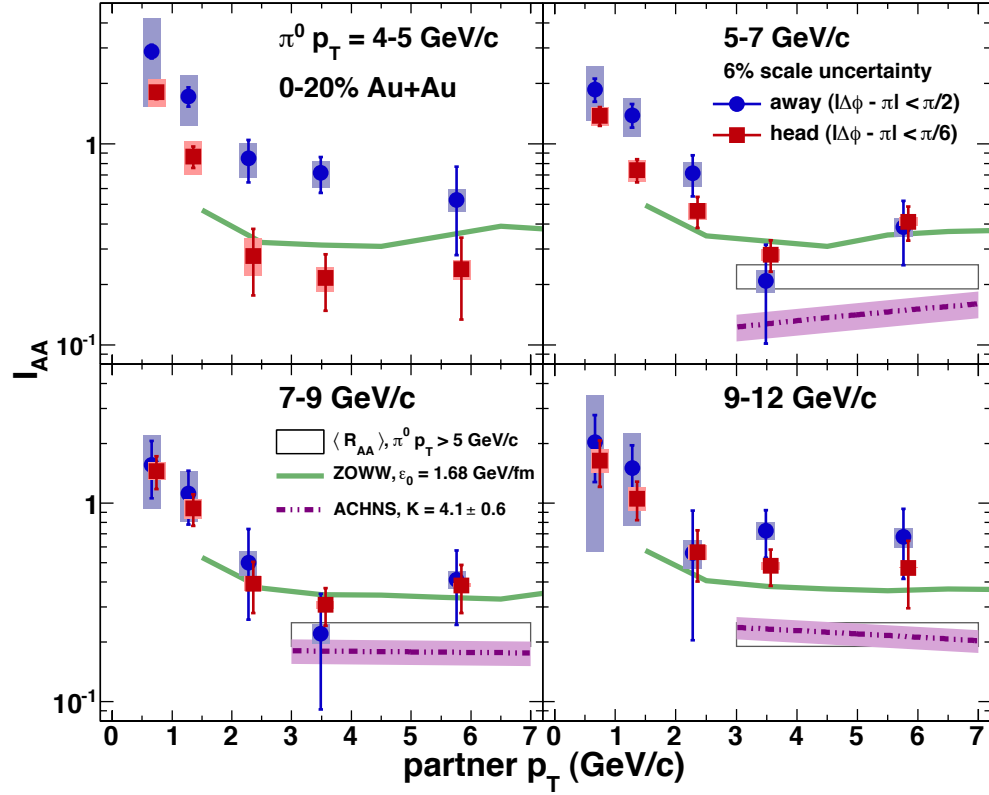


Figure 5.10: I_{AA} for the full away-side (blue) and the narrower head region (red) as a function of partner p_T . Calculations from ZOWW and ACHNS (see text) are included for comparison, along with R_{AA} for trigger $p_T > 5 \text{ GeV/c}$.

spectra used to calculate I_{AA} , it is more sensitive to fixed momentum losses (i.e. leftward shifts) in the Au+Au numerator than for flatter spectra.

5.4.1 Integrated yield and I_{AA} systematic uncertainties

The integrated yields are calculated for the central, high, and low systematic sets of PTY points, which gives the $v_2 + \pi^0 + h^\pm$ uncertainty. The background normalization uncertainty has been evaluated by adding and subtracting the background error to the central point, while the scale uncertainty was propagated in a straightforward manner as a multiplicative constant.

The proper assessment of I_{AA} uncertainties requires a determination of which components cancel in the Au+Au/p+p ratio. The type B error sources are not assumed

to cancel explicitly, however, the I_{AA} high and low errors are found by taking high-high, mid-mid, and low-low ratios, and not other combinations, since it is assumed that while the errors are not correlated, they are not anti-correlated either. A π^0 background uncertainty is very unlikely to go in opposite directions for the two species, for example. The remaining task is evaluation of differences in the background normalization and efficiency errors.

Since the background normalization procedure involves fundamentally different physics assumptions and implementation, it is important to treat them as completely independent.

The efficiency error receives a partial cancellation in the ratio. Recall the error sources in table 4.2. The momentum resolution, PC3 matching recalibration error, and MC/RD differences are all highly correlated in PISA between Runs 6 and 7. The embedding efficiency (5%), particle ratios (3%), and statistical errors (< 1%) remain. As a rough estimate of the uncanceled error, these are simply combined in quadrature to give a scale error of 6%.

Chapter 6

Summary, Interpretation, and a Look Ahead

In this chapter, the results of this analysis are summarized, and interpretations are offered as to their physical meaning and implications in light of the predictions and existing measurements.

6.1 Transverse momentum dependence of jet shapes and yields

Over a broad range of trigger and partner transverse momenta, the jet shape and yield information extracted from the correlations shows that:

- For $p_T^{\pi^0} < 7$, jets on the near side indicate enhanced yields in the lower partner p_T range which descends to an unmodified yield at higher $p_T^{h^\pm}$. Above 7 GeV/c, no near side yield modification is observed.
- On the away side, central Au+Au jet yields demonstrate a transition from enhancement to suppression at $p_T^{h^\pm} \approx 1$ GeV/c for all $p_T^{\pi^0}$ ranges. Above $p_T^{\pi^0} = 7$ GeV/c, the yield modification is the same for the whole away side compared to the narrower peak region, but at lower $p_T^{\pi^0}$, less consistency is observed: a large difference between the head and full away side persists through the full $p_T^{h^\pm}$ range for 4-5 GeV triggers, while the difference is smaller but still discernible in the 5-7 GeV $p_T^{\pi^0}$ range.

These effects can also be summarized by plotting a selection of the conditional yields which represent the same trends visually. This is done in figure 6.1.

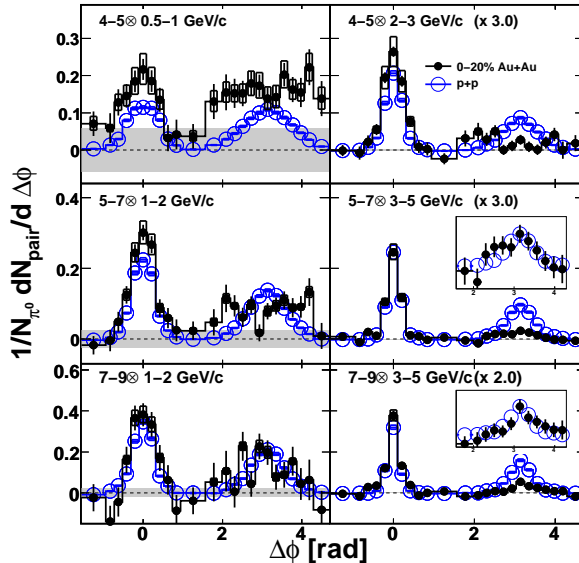


Figure 6.1: Selection of conditional jet yields for central Au+Au and p+p, highlighting the trends discussed in the text. The yields in the right-hand column have been scaled to show more detail. In the inset panels, the Au+Au yields have been normalized to match the p+p peak height to enable a comparison of the shapes.

The best current understanding of the near-side enhancement is that it receives a correlated contribution from the ridge, which is itself not yet well understood. One of the more conventional pictures describing ridge formation is that long-range (particularly in $\Delta\eta$) correlations are formed during the nuclear collision as partons pass near to each other, producing “flux tubes” of chromo-electric fields that are then pushed outward by the radial expansion of the fireball [41]. The physics of the ridge is an area of very active speculation, measurement, and calculation. This data provides one more experimental constraint for any new ridge description models to compare with.

6.2 Low and intermediate p_T phenomenology: what causes the double peak?

Although not not as visually pronounced as in lower- p_T correlations, the away-side shape, which is found to have poor compatibility with a Gaussian form in this analysis, exhibits a highly broadened shape, possibly even reminiscent of a double-peaked structure. In [14, 7] and other results, the peak offset falls in the 1.0-1.2 radian

range, corresponding to a speed of sound in the medium of about $0.2c$ using a simple application of the Mach formula [65]. This value of the sound speed is unexpectedly low given the high density of the medium, and may serve as one piece of evidence casting doubt on conical emission interpretations. However, a cone-like structure has been observed in three-particle correlations in the STAR detector at RHIC [2], whose full azimuthal acceptance is better suited for such measurements than PHENIX. This has led to claims that deflected-jet scenarios are incompatible with the data, and has been claimed to lend strong support for a Mach-cone interpretation.

The two-peaked structure has been observed $\sqrt{s_{NN}} = 158$ GeV at the Super Proton Synchrotron at CERN by the CERES collaboration [62], and at 62 GeV by the PHENIX collaboration [5]. There were even preliminary results in circulation suggesting that the offset peak shape was observed at 17 GeV at the SPS, a beam energy so low that it is highly unlikely that a thermalized QGP-like medium is produced in any appreciable volume. Such results call physical Mach-like correlation interpretations into question, and prompt a revisitation of the methodology involved in identifying the shape and amount of background, a topic to which we now turn.

6.2.1 Questions concerning the 2-source model

It should be noted that the correlation functions themselves do not exhibit any double-peaked structure in this analysis. The bimodal shape is introduced only after subtraction of the flow-modulated background. It is interesting to examine the the assumptions made in this analysis—and in all other correlations analyses found in the literature—that the pair correlations due to flow can be completely factorized from those due to jets, and that the flow component should take on its full value as measured in an independent analysis. As an example, the $4-5 \otimes 0.5-1$ GeV/c $C(\Delta\phi)$ is shown for 0-20% centrality in figure 6.2. A near + away-side single Gaussian fit is applied, with a free constant as the background level, simply to capture the essential shape. The

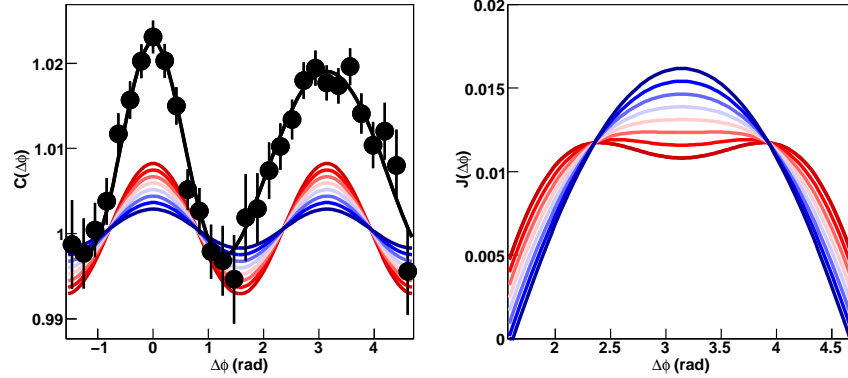


Figure 6.2: Simple example showing how a reduction in v_2 causes a transition from the bimodal to single-peaked jet shape.

darkest red curve represents the measured pair v_2 value used in this analysis, and each subsequent curve is a (1, 2, 3, ...) $\times 10\%$ reduction from this value. The normalization is fixed for all v_2 values as the ABS ξ level calculated for that bin. The right hand plot gives the background-subtracted jet function (not normalized per trigger). A 20-30% reduction in the v_2 results in a very different qualitative interpretation.

This simple exercise is intended not to question existing measurements of elliptic flow by PHENIX or others, but to demonstrate that the full-factorization assumption made by the two-source model carries significant ramifications, and that the background-subtracted result is highly sensitive to the pair v_2 input value. It is interesting that the mach-cone feature is most pronounced precisely where the jet correlation strength is weakest relative to the background. If the mach cone structure is truly due to physical, and not experimental, effects, it would be reassuring to see evidence of the the conical emission structure at higher trigger $p_T \otimes$ low $p_T^{h^\pm}$, where one might expect medium response from a very energetic parton. Unfortunately, the current statistics are poor in this region, and although the two peak structure could be hiding within this larger single peak, the data seem to be silent on this question for the moment. In fact, it is not clear that improved statistical precision would distinguish a physics vs. experimental bias

scenario, since a single, large peak could be formed equivalently through (a) a bimodal + central punchthrough component, (b) the merging of two split peaks (if the cone angle were to close, as predicted by the Cherenkov picture), or (c) the disappearance of the mach cone and replacement with a punch-through peak. Combinations of these options are also not precluded.

The addition of other components in the correlations besides jets and flow are likely to imply that the v_2 amplitude is overestimated. Moreover, if the sample of trigger particles is contaminated by background, the pair yield per trigger particle is reduced by (a) an enhancement of the background pedestal due to the isotropic formation of randomly-triggered pairs, and (b) a reduction in the correlated per-trigger pair yield in the peaks from an increase in fake trigger particles without a corresponding gain in signal pairs.

However, several of the alternative mechanisms listed in chapter 1, such as flow + surface emission, v_3 , event fluctuations or 3-jet events with enhanced selection through isotropic background production, etc. are quantitatively vague notions at this time, and it is hoped that the “non-flow effects” proposed in the literature are made more concrete in terms of a physical picture and a quantitative estimation, so that they are distinguished from phenomena that are already described in more conventional frameworks.

6.3 High p_T phenomenology: surface emission or punchthrough?

In light of the previous discussion, the high- p_T region studied in this analysis is of particular value because (a) the flow amplitude is miniscule in compared to the jet correlation strength, so any of the systematic biases mentioned in the previous section are negligible in comparison with the other uncertainties, and (b) this region is expected to be amenable to pQCD calculations, which are currently best constraint for leading parton E-loss models. In fact, jet quenching calculations similar to the one described

in section 1.6.1 have been recently performed specifically for comparison with I_{AA} from this analysis, and are discussed in section 5.4.

As an additional consideration, the PID dependence is weaker at high p_T because (a) it is above the recombination/coalescence region which begins to diminish near 5-6 GeV, and (b) the parton to p vs pion fragmentation is more similar since $m_{\pi^0}, m_p \ll E_{parton}$.

One important puzzle revolves around the question of why the jet peak is highly suppressed at high energies, but its shape appears unmodified. Two primary explanations are often made, which are not mutually exclusive. One is that the medium is so opaque to color charges that only hard-scattering vertices allowing emission from the surface of the fireball permit an escape of high-momentum hadrons. This surface-bias effect is often invoked in R_{AA} interpretations as well. A second picture is that since gluon emission is somehow quantized, it is possible that a small number of hard gluons are radiated through parton-medium interactions as the dominant energy loss mechanism, rather than many soft gluons.

An major conclusion from this analysis is that although the data lacks high statistical precision at the highest trigger p_T , no double-peaked structure is discernible on the away side for *any* partner momenta, even at the lowest end of the range. If collective medium response effects increase with the energy of hard-scattered traversing partons, the high-trigger-low-partner momentum regime is where one would expect to see the most pronounced effects. Therefore, although a modified shape is observed at the lowest trigger and partner p_T values, conical emission scenarios are not well supported by the results from this analysis.

Finally, the comparison of conditional pair yields in Au+Au compared to a $p+p$ reference as measured by I_{AA} shows consistently that iaa is larger than or similar to R_{AA} , and that the difference becomes larger at the highest trigger momenta. Since the two observables do not necessarily express energy loss of hard-scattered partons in the

same way, their comparison affords an additional measure of constraint for energy loss and medium response models to match.

6.4 Conclusion

In this analysis, the transition with p_T from enhanced and medium-modified jets to suppressed, vacuum-like jets has been quantified with identified neutral pion trigger particles over a broad momentum range and different collision centralities. It was observed that for triggers in the 4-5 (5-7) GeV/c range, the onset of modification occurs below 3-5 (2-3) GeV/c in partner p_T . The level of suppression above the transitional region was measured with high precision, enabling new comparisons with models and thus improved constraints on theories describing energy loss and its implications for the quark-gluon plasma phase.

Bibliography

- [1] B. I. Abelev, M. M. Aggarwal, Z. Ahammed, A. V. Alakhverdyants, B. D. Anderson, D. Arkhipkin, G. S. Averichev, J. Balewski, O. Barannikova, L. S. Barnby, J. Baudot, S. Baumgart, D. R. Beavis, R. Bellwied, F. Benedosso, M. J. Betancourt, R. R. Betts, A. Bhasin, A. K. Bhati, H. Bichsel, J. Bielcik, J. Bielcikova, B. Biritz, L. C. Bland, I. Bnzarov, M. Bombara, and B. E. Bonner. Long range rapidity correlations and jet production in high energy nuclear collisions. Phys. Rev. C, 80(6):064912, Dec 2009.
- [2] B. I. Abelev et al. Indications of Conical Emission of Charged Hadrons at RHIC. Phys. Rev. Lett., 102:052302, 2009.
- [3] D Acosta and CDF. Underlying event in hard interactions at the fermilab tevatron p p collider. Phys. Rev. D, 70(7), Oct 2004.
- [4] J Adams, M Aggarwal, Z Ahammed, and J Amonett. Direct observation of dijets in central au+ au collisions at 200 gev. Phys. Rev. Lett., Jan 2006.
- [5] A Adare, S. S Adler, S Afanasiev, C Aidala, N. N Ajitanand, Y Akiba, H Al-Bataineh, J Alexander, A Al-Jamel, K Aoki, L Aphecetche, R Armendariz, S. H Aronson, J Asai, E. T Atomssa, R Averbeck, T. C Awes, B Azmoun, V Babintsev, G Baksay, L Baksay, A Baldisseri, K. N Barish, P. D Barnes, B Bassalleck, S Bathe, S Batsouli, V Baublis, F Bauer, A Bazilevsky, S Belikov, R Bennett, Y Berdnikov, A. A Bickley, M. T Bjorndal, J. G Boissevain, H Borel, K Boyle, M. L Brooks, D. S Brown, N Bruner, D Bucher, H Buesching, V Bumazhnov, G Bunce, J. M Burward-Hoy, S Butsyk, X Camard, S Campbell, J.-S Chai, P Chand, B. S Chang, W. C Chang, J.-L Charvet, S Chernichenko, J Chiba, C. Y Chi, M Chiu, I. J Choi, R. K Choudhury, T Chujo, P Chung, A Churnyn, V Cianciolo, C. R Cleven, Y Cobigo, B. A Cole, M. P Comets, P Constantin, M Csanad, T Csoergo, J. P Cussonneau, T Dahms, K Das, G David, F Deak, M. B Deaton, K Dehmelt, H Delagrangé, A Denisov, D d'Enterria, A Deshpande, E. J Desmond, A Devismes, O Dietzsch, A Dion, M Donadelli, J. L Drachenberg, O Drapier, A Drees, A. K Dubey, A Durum, D Dutta, V Dzhordzhadze, Y. V Efremenko, J Egdemir, F Ellinghaus, W. S Emam, A Enokizono, H En'yo, B Espagnon, S Esumi, K. O Eyser, D. E Fields, C Finck, M Finger, F Fleuret, S. L Fokin, B Forestier, B. D Fox, Z Fraenkel, J. E Frantz, A Franz, A. D Frawley, K Fujiwara, Y Fukao, S.-Y Fung, T Fusayasu, S Gadrat, I Garishvili, F Gastineau, M Germain, A Glenn, H Gong, M Gonin, J Gosset, Y Goto, R. Granier De Cassagnac, N Grau, S. V Greene, M. Grosse

Perdekamp, T Gunji, H.-A Gustafsson, T Hachiya, A. Hadj Henni, C Haegemann, J. S Haggerty, M. N Hagiwara, H Hamagaki, R Han, A. G Hansen, H Harada, E. P Hartouni, K Haruna, M Harvey, E Haslum, K Hasuko, R Hayano, M Heffner, T. K Hemmick, T Hester, J. M Heuser, X He, P Hidas, H Hiejima, J. C Hill, R Hobbs, M Hohlmann, M Holmes, W Holzmann, K Homma, B Hong, A Hoover, T Horaguchi, D Hornback, M. G Hur, T Ichihara, V. V Ikonnikov, K Imai, M Inaba, Y Inoue, M Inuzuka, D Isenhower, L Isenhower, M Ishihara, T Isobe, M Issah, A Isupov, B. V Jacak, J Jia, J Jin, O Jinnouchi, B. M Johnson, S. C Johnson, K. S Joo, D Jouan, F Kajihara, S Kametani, N Kamihara, J Kamin, M Kaneta, J. H Kang, H Kanou, K Katou, T Kawabata, T Kawagishi, D Kawall, A. V Kazantsev, S Kelly, B Khachaturov, A Khanzadeev, J Kikuchi, D. H Kim, D. J Kim, E Kim, G.-B Kim, H. J Kim, Y.-S Kim, E Kinney, A Kiss, E Kistenev, A Kiyomichi, J Klay, C Klein-Boesing, H Kobayashi, L Kochenda, V Kochetkov, R Kohara, B Komkov, M Konno, D Kotchetkov, A Kozlov, A Kral, A Kravitz, P. J Kroon, J Kubart, C. H Kuberg, G. J Kunde, N Kurihara, K Kurita, M. J Kweon, Y Kwon, G. S Kyle, R Lacey, Y.-S Lai, J. G Lajoie, A Lebedev, Y Le Bornec, S Leckey, D. M Lee, M. K Lee, T Lee, M. J Leitch, M. A. L Leite, B Lenzi, H Lim, T Liska, A Litvinenko, M. X Liu, X Li, X. H Li, B Love, D Lynch, C. F Maguire, Y. I Makdisi, A Malakhov, M. D Malik, V. I Manko, Y Mao, G Martinez, L Masek, H Masui, F Matathias, T Matsumoto, M. C McCain, M Mccumber, P. L Mcgaughey, Y Miake, P Mikes, K Miki, T. E Miller, A Milov, S Mioduszewski, G. C Mishra, M Mishra, J. T Mitchell, M Mitrovski, A. K Mohanty, A Morreale, D. P Morrison, J. M Moss, T. V Moukhanova, D Mukhopadhyay, M Muniruzzaman, J Murata, S Nagamiya, Y Nagata, J. L Nagle, M Naglis, I Nakagawa, Y Nakamiya, T Nakamura, K Nakano, J Newby, M Nguyen, B. E Norman, A. S Nyanin, J Nystrand, E O'Brien, S. X Oda, C. A Ogilvie, H Ohnishi, I. D Ojha, H Okada, K Okada, M Oka, O. O Omiwade, A Oskarsson, I Otterlund, M Ouchida, K Oyama, K Ozawa, R Pak, D Pal, A. P. T Palounek, V Pantuev, V Papavassiliou, J Park, W. J Park, S. F Pate, H Pei, V Penev, J.-C Peng, H Pereira, V Peresedov, D. Yu Peressounko, A Pierson, C Pinkenburg, R. P Pisani, M. L Purschke, A. K Purwar, J. M Qualls, H Qu, J Rak, A Rakotozafindrabe, I Ravinovich, K. F Read, S Rembeczki, M Reuter, K Reygers, V Riabov, Y Riabov, G Roche, A Romana, M Rosati, S. S. E Rosendahl, P Rosnet, P Rukoyatkin, V. L Rykov, S. S Ryu, B Sahlmuller, N Saito, T Sakaguchi, S Sakai, H Sakata, V Samsonov, L Sanfratello, R Santo, H. D Sato, S Sato, S Sawada, Y Schutz, J Seele, R Seidl, V Semenov, R Seto, D Sharma, T. K Shea, I Shein, A Shevel, T.-A Shibata, K Shigaki, M Shimomura, T Shohjoh, K Shoji, A Sickles, C. L Silva, D Silvermyr, C Silvestre, K. S Sim, C. P Singh, V Singh, S Skutnik, M Slunecka, W. C Smith, A Soldatov, R. A Soltz, W. E Sondheim, S. P Sorensen, I. V Sourikova, F Staley, P. W Stankus, E Stenlund, M Stepanov, A Ster, S. P Stoll, T Sugitate, C Suire, J. P Sullivan, J Sziklai, T Tabaru, S Takagi, E. M Takagui, A Taketani, K. H Tanaka, Y Tanaka, K Tanida, M. J Tannenbaum, A Taranenko, P Tarjan, T. L Thomas, M Togawa, A Toia, J Tojo, L Tomasek, H Torii, R. S Towell, V-N Tram, I Tserruya, Y Tsuchimoto, S. K Tuli, H Tydesjoe, N Tyurin, T. J Uam, C Vale, H Valle, H. W Vanhecke, J Velkovska, M Velkovsky, R Vertesi, V Veszpremi, A. A Vinogradov, M Virius, M. A Volkov, V Vrba, E Vznuzdaev, M Wagner, D W. System size and energy dependence of jet-induced hadron pair correlation shapes in cu+cu and au+au

collisions at root s-nn 200 and 62.4 gev. *Phys. Rev. Lett.*, 98(23):232302, Jan 2007.

- [6] A Adare, S Afanasiev, C Aidala, N. N Ajitanand, Y Akiba, H Al-Bataineh, J Alexander, A Al-Jamel, K Aoki, L Aphecetche, R Armendariz, S. H Aronson, J Asai, E. T Atomssa, R Averbeck, T. C Awes, B Azmoun, V Babintsev, G Baksay, L Baksay, A Baldisseri, K. N Barish, P. D Barnes, B Bassalleck, S Bathe, S Batsouli, V Baublis, F Bauer, A Bazilevsky, S Belikov, R Bennett, Y Berdnikov, A. A Bickley, M. T Bjorndal, J. G Boissevain, H Borel, K Boyle, M. L Brooks, D. S Brown, D Bucher, H Buesching, V Bumazhnov, G Bunce, J. M Burward-Hoy, S Butsyk, S Campbell, J. S Chai, B. S Chang, J. L Charvet, S Chernichenko, J Chiba, C. Y Chi, M Chiu, I. J Choi, T Chujo, P Chung, A Churn, V Cianciolo, C. R Cleven, Y Cobigo, B. A Cole, M. P Comets, P Constantin, M Csanad, T Csoergo, T Dahms, K Das, G David, M. B Deaton, K Dehmelt, H Delagrange, A Denisov, D d'Enterria, A Deshpande, E. J Desmond, O Dietzsch, A Dion, M Donadelli, J. L Drachenberg, O Drapier, A Drees, A. K Dubey, A Durum, V Dzhordzhadze, Y. V Efremenko, J Egdemir, F Ellinghaus, W. S Emam, A Enokizono, H En'yo, B Espagnon, S Esumi, K. O Eyser, D. E Fields, M Finger, M Finger, F Fleuret, S. L Fokin, B Forestier, Z Fraenkel, J. E Frantz, A Franz, A. D Frawley, K Fujiwara, Y Fukao, S. Y Fung, T Fusayasu, S Gadrat, I Garishvili, F Gastineau, M Germain, A Glenn, H Gong, M Gonin, J Gosset, Y Goto, R. Greiner de Casagnac, N Grau, S. V Greene, M. Goose Perdekamp, T Gunji, H. A Gustafsson, T Hachiya, A. Hadj Henni, C Haegemann, J. S Haggerty, M. N Hagiwara, H Hamagaki, R Han, H Harada, E. P Hartouni, K Haruna, M Harvey, E Haslum, K Hasuko, R Hayano, M Heffner, T. K Hemmick, T Hester, J. M Heuser, X He, H Hiejima, J. C Hill, R Hobbs, M Hohlmann, M Holmes, W Holzmann, K Homma, B Hong, T Horaguchi, D Hornback, M. G Hur, T Ichihara, K Imai, J Imrek, M Inaba, Y Inoue, D Isenhower, L Isenhower, M Ishihara, T Isobe, M Issah, A Isupov, B. V Jacak, J Jia, J Jin, O Jinnouchi, B. M Johnson, K. S Joo, D Jouan, F Kajihara, S Kametani, N Kamihara, J Kamin, M Kaneta, J. H Kang, H Kanou, T Kawagishi, D Kawall, A. V Kazantsev, S Kelly, A Khanzadeev, J Kikuchi, D. H Kim, D. J Kim, E Kim, Y. S Kim, E Kinney, A Kiss, E Kistenev, A Kiyomichi, J Klay, C Klein-Boesing, L Kochenda, V Kochetkov, B Komkov, M Konno, D Kotchetkov, A Kozlov, A Kral, A Kravitz, P. J Kroon, J Kubart, G. J Kunde, N Kurihara, K Kurita, M. J Kweon, Y Kwon, G. S Kyle, R Lacey, Y. S Lai, J. G Lajoie, A Lebedev, Y Le Bornec, S Leckey, D. M Lee, M. K Lee, T Lee, M. J Leitch, M. A. L Leite, B Lenzi, H Lim, T Liska, A Litvinenko, M. X Liu, X Li, X. H Li, B Love, D Lynch, C. F Maguire, Y. I Makdisi, A Malakhov, M. D Malik, V. I Manko, Y Mao, L Masek, H Masui, F Matathias, M. C McCain, M Mccumber, P. L Mcgaughey, Y Miake, P Mikes, K Miki, T. E Miller, A Milov, S Mioduszewski, G. C Mishra, M Mishra, J. T Mitchell, M Mitrovski, A Morreale, D. P Morrison, J. M Moss, T. V Moukhanova, D Mukhopadhyay, J Murata, S Nagamiya, Y Nagata, J. L Nagle, M Naglis, I Nakagawa, Y Nakamiya, T Nakamura, K Nakano, J Newby, M Nguyen, B. E Norman, A. S Nyanin, J Nystrand, E O'Brien, S. X Oda, C. A Ogilvie, H Ohnishi, I. D Ojha, H Okada, K Okada, M Oka, O. O Omiwade, A Oskarsson, I Otterlund, M Ouchida, K Ozawa, R Pak, D Pal, A. P. T Palounek, V Pantuev, V Papavassiliou, J Park, W. J Park, S. F Pate, H Pei, J. C Peng, H Pereira, V Peresedov, D. Yu Peressounko, C Pinkenburg, R. P Pisani, M. L

- Purschke, A. K Purwar, H Qu, J Rak, A Rakotozafindrabe, I Ravinovich, K. F Read, S Rembeczki, M Reuter, K Reygers, V Riabov, Y Riabov, G Roche, A Romana, M Rosati, S. S. E Rosendahl, P Rosnet, P Rukoyatkin, V. L Rykov, S. S Ryu, B Sahlmueller, N Saito, T Sakaguchi, S Sakai, H Sakata, V Samsonov, H. D Sato, S Sato, S Sawada, J Seele, R Seidl, V Semenov, R Seto, D Sharma, T. K Shea, I Shein, A Shevel, T. A Shibata, K Shigaki, M Shimomura, T Shohjoh, K Shoji, A Sickles, C. L Silva, D Silvermyr, C Silvestre, K. S Sim, C. P Singh, V Singh, S Skutnik, M Slunecka, W. C Smith, A Soldatov, R. A Soltz, W. E Sondheim, S. P Sorensen, I. V Sourikova, F Staley, P. W Stankus, E Stenlund, M Stepanov, A Ster, S. P Stoll, T Sugitate, C Suire, J. P Sullivan, J Sziklai, T Tabaru, S Takagi, E. M Takagui, A Taketani, K. H Tanaka, Y Tanaka, K Tanida, M. J Tannenbaum, A Taranenko, P Tarjan, T. L Thomas, M Togawa, A Toia, J Tojo, L Tomasek, H Torii, R. S Towell, V. N Tram, I Tserruya, Y Tsuchimoto, S. K Tuli, H Tydesjo, N Tyurin, C Vale, H Valle, H. W Van Hecke, J Velkovska, R Vertesi, A. A Vinogradov, M Virius, V Vrba, E Vznuzdaev, M Wagner, D Walker, X. R Wang, Y Watanabe, J Wessels, S. N White, N Willis, D Winter, C. L Woody, M Wysocki, W Xie, Y. L Yamaguchi, A Yanovich, Z Yasin, J Ying, S Yokkaichi, G. R Young, I Younus, I. E Yushmanov, W. A Zajc, O Zaudtke, C Zhang, S Zhou, J Zimanyi, and L Zolin. Quantitative constraints on the transport properties of hot partonic matter from semi-inclusive single high transverse momentum pion suppression in au plus au collisions at root s-nn=200 gev. Physical Review C, 77(6):064907, Jan 2008.
- [7] A Adare, S Afanasiev, C Aidala, NN Ajitanand, Y Akiba, H Al-Bataineh, J Alexander, A Al-Jamel, K Aoki, and L Aphecetche. Dihadron azimuthal correlations in au+au collisions at 200 gev. Physical Review C, 78(1):14901, 2008.
- [8] A Adare and PHENIX. Harmonic flow of charged hadrons in au+au collisions at 200 gev: a probe for thermalization. in preparation.
- [9] K Adcox, SS Adler, M Aizama, NN Ajitanand, Y Akiba, H Akikawa, J Alexander, A Al-Jamel, M Allen, and G Alley. Phenix detector overview. Nuclear Inst. and Methods in Physics Research, A, 499(2-3):469–479, 2003.
- [10] K Adcox, J Ajitanand, J Alexander, J Barrette, R Belkin, D Borland, WL Bryan, R Du Rietz, K El Chenawi, and A Cherlin. Construction and performance of the phenix pad chambers. Nuclear Inst. and Methods in Physics Research, A, 497(2-3):263–293, 2003.
- [11] K Adcox, NN Ajitanand, J Alexander, D Autrey, R Averbeck, B Azmoun, KN Barish, VV Baublis, R Belkin, and S Bhaganatula. Phenix central arm tracking detectors. Nuclear Inst. and Methods in Physics Research, A, 499(2-3):489–507, 2003.
- [12] C Adler, A Denisov, E Garcia, M Murray, H Stroebele, and S White. The rhic zero degree calorimeters. Nuclear Inst. and Methods in Physics Research, A, 470(3):488–499, 2001.
- [13] S. S Adler, S Afanasiev, C Aidala, N. N Ajitanand, Y Akiba, A Al-Jamel, J Alexander, K Aoki, L Aphecetche, R Armendariz, S. H Aronson, R Averbeck, T. C Awes,

V Babintsev, A Baldisseri, K. N Barish, P. D Barnes, B Bassalleck, S Bathe, S Batsouli, V Baublis, F Bauer, A Bazilevsky, S Belikov, M. T Bjornndal, J. G Boissevain, H Borel, M. L Brooks, D. S Brown, N Bruner, D Bucher, H Buesching, V Bumazhnov, G Bunce, J. M Burward-Hoy, S Butsyk, X Camard, P Chand, W. C Chang, S Chernichenko, C. Y Chi, J Chiba, M Chiu, I. J Choi, R. K Choudhury, T Chujo, V Cianciolo, Y Cobigo, B. A Cole, M. P Comets, P Constantin, M Csanad, T Csorgo, J. P Cussonneau, D d'Enterria, K Das, G David, F Deak, H Delagrang, A Denisov, A Deshpande, E. J Desmond, A Devismes, O Dietzsch, J. L Drachenberg, O Drapier, A Drees, A Durum, D Dutta, V Dzhordzhadze, Y. V Efremenko, H En'yo, B Espagnon, S Esumi, D. E Fields, C Finck, F Fleuret, S. L Fokin, B. D Fox, Z Fraenkel, J. E Frantz, A Franz, A. D Frawley, Y Fukao, S. Y Fung, S Gadrat, M Germain, A Glenn, M Gonin, J Gosset, Y Goto, R. Granier De Casagnac, N Grau, S. V Greene, M. Grosse Perdekamp, H. A Gustafsson, T Hachiya, J. S Haggerty, H Hamagaki, A. G Hansen, E. P Hartouni, M Harvey, K Hasuko, R Hayano, X He, M Heffner, T. K Hemmick, J. M Heuser, P Hidas, H Hiejima, J. C Hill, R Hobbs, W Holzmann, K Homma, B Hong, A Hoover, T Horaguchi, T Ichihara, V. V Ikonnikov, K Imai, M Inaba, M Inuzuka, D Isenhow, L Isenhow, M Ishihara, M Issah, A Isupov, B. V Jacak, J Jia, O Jinnouchi, B. M Johnson, S. C Johnson, K. S Joo, D Jouan, F Kajihara, S Kametani, N Kamihara, M Kaneta, J. H Kang, K Katou, T Kawabata, A. V Kazantsev, S Kelly, B Khachaturov, A Khanzadeev, J Kikuchi, D. J Kim, E Kim, G. B Kim, H. J Kim, E Kinney, A Kiss, E Kistenev, A Kiyomichi, C Klein-Boesing, H Kobayashi, L Kochenda, V Kochetkov, R Kohara, B Komkov, M Konno, D Kotchetkov, A Kozlov, P. J Kroon, C. H Kuberg, G. J Kunde, K Kurita, M. J Kweon, Y Kwon, G. S Kyle, R Lacey, J. G Lajoie, Y Le Bornec, A Lebedev, S Leckey, D. M Lee, M. J Leitch, M. A. L Leite, X. H Li, H Lim, A Litvinenko, M. X Liu, C. F Maguire, Y. I Makdisi, A Malakhov, V. I Manko, Y Mao, G Martinez, H Masui, F Matathias, T Matsumoto, M. C McCain, P. L Mcgaughey, Y Miake, T. E Miller, A Milov, S Mioduszewski, G. C Mishra, J. T Mitchell, A. K Mohanty, D. P Morrison, J. M Moss, D Mukhopadhyay, M Muniruzzaman, S Nagamiya, J. L Nagle, T Nakamura, J Newby, A. S Nyanin, J Nystrand, E O'Brien, C. A Ogilvie, H Ohnishi, I. D Ojha, H Okada, K Okada, A Oskarsson, I Otterlund, K Oyama, K Ozawa, D Pal, A. P. T Palounek, V Pantuev, V Papavassiliou, J Park, W. J Park, S. F Pate, H Pei, V Penev, J. C Peng, H Pereira, V Peresedov, A Pierson, C Pinkenburg, R. P Pisani, M. L Purschke, A. K Purwar, J. M Qualls, J Rak, I Ravinovich, K. F Read, M Reuter, K Reygers, V Riabov, Y Riabov, G Roche, A Romana, M Rosati, S. S. E Rosendahl, P Rosnet, V. L Rykov, S. S Ryu, N Saito, T Sakaguchi, S Sakai, V Samsonov, L Sanfratello, R Santo, H. D Sato, S Sato, S Sawada, Y Schutz, V Semenov, R Seto, T. K Shea, I Shein, T. A Shibata, K Shigaki, M Shimomura, A Sickles, C. L Silva, D Silvermyr, K. S Sim, A Soldatov, R. A Soltz, W. E Sondheim, S. P Sorensen, I. V Sourikova, F Staley, P. W Stankus, E Stenlund, M Stepanov, A Ster, S. P Stoll, T Sugitate, J. P Sullivan, S Takagi, E. M Takagui, A Taketani, K. H Tanaka, Y Tanaka, K Tanida, M. J Tannenbaum, A Taranenko, P Tarjan, T. L Thomas, M Togawa, J Tojo, H Torii, R. S Towell, V-N Tram, I Tserruya, Y Tsuchimoto, H Tydesjo, N Tyurin, T. J Uam, H. W Van Hecke, J Velkovska, M Velkovsky, V Veszpremi, A. A Vinogradov, M. A Volkov, E Vznuzdaev, X. R Wang, Y Watanabe, S. N White, N Willis, F. K Wohn, C. L

Woody, W Xie, A Yanovich, S Yokkaichi, G. R Young, I. E Yushmanov, W. A Zajc, C Zhang, S Zhou, J Zimanyi, L Zolin, and X Zong. Jet properties from dihadron correlations in p plus p collisions at root s=200 gev. *Phys. Rev. D*, 74(7):072002, Jan 2006. Notes.

- [14] S. S Adler, S Afanasiev, C Aidala, N. N Ajitanand, Y Akiba, J Alexander, R Amirikas, L Aphetche, S. H Aronson, R Averbek, T. C Awes, R Azmoun, V Babintsev, A Baldisseri, K. N Barish, P. D Barnes, B Bassalleck, S Bathe, S Batsouli, V Baublis, A Bazilevsky, S Belikov, Y Berdnikov, S Bhagavatula, J. G Boissevain, H Borel, S Borenstein, M. L Brooks, D. S Brown, N Bruner, D Bucher, H Buesching, V Bumazhnov, G Bunce, J. M Burward-Hoy, S Butsyk, X Camard, J. S Chai, P Chand, W. C Chang, S Chernichenko, C. Y Chi, J Chiba, M Chiu, I. J Choi, J Choi, R. K Choudhury, T Chujo, V Cianciolo, Y Cobigo, B. A Cole, P Constantin, D d'Enterria, G David, H Delagrang, A Denisov, A Deshpande, E. J Desmond, A Devismes, O Dietzsch, O Drapier, A Drees, R Du Rietz, A Durum, D Dutta, Y. V Efremenko, K El Chenawi, A Enokizono, H En'yo, S Esumi, L Ewell, D. E Fields, F Fleuret, S. L Fokin, B. D Fox, Z Fraenkel, J. E Frantz, A Franz, A. D Frawley, S. Y Fung, S Garpman, T. K Ghosh, A Glenn, G Gogiberidze, M Gonnin, J Gosset, Y Goto, R Granier De Cassagnac, N Grau, S. V Greene, M Grosse Perdekamp, W Guryn, H. A Gustafsson, T Hachiya, J. S Haggerty, H Hamagaki, A. G Hansen, E. P Hartouni, M Harvey, R Hayano, N Hayashi, X He, M Heffner, T. K Hemmick, J. M Heuser, M Hibino, J. C Hill, W Holzmann, K Homma, B Hong, A Hoover, T Ichihara, V. V Ikonnikov, K Imai, D Isenhower, M Ishihara, M Issah, A Isupov, B. V Jacak, W. Y Jang, Y Jeong, J Jia, O Jinnouchi, B. M Johnson, S. C Johnson, K. S Joo, D Jouan, S Kametani, N Kamihara, J. H Kang, S. S Kapoor, K Katou, S Kelly, B Khachaturov, A Khanzadeev, J Kikuchi, D. H Kim, D. J Kim, D. W Kim, E Kim, G. B Kim, H. J Kim, E Kistenev, A Kiyomichi, K Kiyoyama, C Klein-Boesing, H Kobayashi, L Kochenda, V Kochetkov, D Koehler, T Kohama, M Kopytine, D Kotchetkov, A Kozlov, P. J Kroon, C. H Kuberg, K Kurita, Y Kuroki, M. J Kweon, Y Kwon, G. S Kyle, R Lacey, V Ladygin, J. G Lajoie, A Lebedev, S Leckey, D. M Lee, S Lee, M. J Leitch, X. H Li, H Lim, A Litvinenko, M. X Liu, Y Liu, C. F Maguire, Y. I Makdisi, A Malakhov, V. I Manko, Y Mao, G Martinez, M. D Marx, H Masui, F Matathias, T Matsumoto, P. L Mcgaughey, E Melnikov, F Messer, Y Miake, J Milan, T. E Miller, A Milov, S Mioduszewski, R. E Mischke, G. C Mishra, J. T Mitchell, A. K Mohanty, D. P Morrison, J. M Moss, F Muhlbacher, D Mukhopadhyay, M Muniruzzaman, J Murata, S Nagamiya, J. L Nagle, T Nakamura, B. K Nandi, M Nara, J Newby, P Nilsson, A. S Nyanin, J Nystrand, E O'Brien, C. A Ogilvie, H Ohnishi, I. D Ojha, K Okada, M Ono, V Onuchin, A Oskarsson, I Otterlund, K Oyama, K Ozawa, D Pal, A. P. T Palounek, V Pantuev, V Papavassiliou, J Park, A Parmar, S. F Pate, T Peitzmann, J. C Peng, V Peresedov, C Pinkenburg, R. P Pisani, F Plasil, M. L Purschke, A. K Purwar, J Rak, I Ravinovich, K. F Read, M Reuter, K Reygers, V Riabov, Y Riabov, G Roche, A Romana, M Rosati, P Rosnet, S. S Ryu, M. E Sadler, N Saito, T Sakaguchi, M Sakai, S Sakai, V Samsonov, L Sanfratello, R Santo, H. D Sato, S Sato, S Sawada, Y Schutz, V Semenov, R Seto, M. R Shaw, T. K Shea, T. A Shibata, K Shigaki, T Shiina, C. L Silva, D Silvermyr, K. S Sim, C. P Singh, V Singh, M Sivertz, A Soldatov, R. A Soltz, W. E Sondheim, S. P Sorensen, I. V Sourikova,

- F Staley, P. W Stankus, E Stenlund, M Stepanov, A Ster, S. P Stoll, T Sugitate, J. P Sullivan, E. M Takagui, A Taketani, M Tamai, K. H Tanaka, Y Tanaka, K Tanida, M. J Tannenbaum, P Tarjan, J. D Tepe, T. L Thomas, J Tojo, H Torii, R. S Towell, I Tserruya, H Tsuruoka, S. K Tuli, H Tydesjo, N Tyurin, H. W Van Hecke, J Velkovska, M Velkovsky, V Veszpremi, L Villatte, A. A Vinogradov, M. A Volkov, E Vznuzdaev, X. R Wang, Y Watanabe, S. N White, F. K Wohn, C. L Woody, W Xie, Y Yang, A Yanovich, S Yokkaichi, G. R Young, I. E Yushmanov, W. A Zajc, C Zhang, S Zhou, S. J Zhou, and L Zolin. Dense-medium modifications to jet-induced hadron pair distributions in au+au collisions at $\sqrt{s_{NN}}=200$ gev. *Phys. Rev. Lett.*, 97(5):052301, Jan 2006.
- [15] SS Adler, S Afanasiev, C Aidala, NN Ajitanand, Y Akiba, J Alexander, R Amirikas, L Aphecetche, SH Aronson, R Averbeck, TC Awes, R Azmoun, V Babintsev, A Baldisseri, KN Barish, PD Barnes, B Bassalleck, S Bathe, S Batsouli, V Baublis, A Bazilevsky, S Belikov, Y Berdnikov, S Bhagavatula, JG Boissevain, H Borel, S Borenstein, ML Brooks, DS Brown, N Bruner, D Bucher, H Buesching, V Bumazhnov, G Bunce, JM Burward-Hoy, S Butsyk, X Camard, JS Chai, P Chand, WC Chang, S Chernichenko, CY Chi, J Chiba, M Chiu, IJ Choi, J Choi, RK Choudhury, T Chujo, V Cianciolo, Y Cobigo, BA Cole, P Constantin, DG d'Enterria, G David, H Delagrang, A Denisov, A Deshpande, EJ Desmond, O Dietzsch, O Drapier, A Drees, R Du Rietz, A Durum, D Dutta, YV Efremenko, K El Chenawi, A Enokizono, H En'yo, S Esumi, L Ewell, DE Fields, F Fleuret, SL Fokin, BD Fox, Z Fraenkel, JE Frantz, A Franz, AD Frawley, SY Fung, S Garpman, TK Ghosh, A Glenn, G Gogiberidze, M Gonin, J Gosset, Y Goto, RG de Casagnac, N Grau, SV Greene, MG Perdekamp, W Guryn, HA Gustafsson, T Hachiya, JS Hagerty, H Hamagaki, AG Hansen, EP Hartouni, M Harvey, R Hayano, X He, M Heffner, TK Hemmick, JM Heuser, M Hibino, JC Hill, W Holzmann, K Homma, B Hong, A Hoover, T Ichihara, VV Ikonnikov, K Imai, D Isenhower, M Ishihara, M Issah, A Isupov, BV Jacak, WY Jang, Y Jeong, J Jia, O Jinnouchi, BM Johnson, SC Johnson, KS Joo, D Jouan, S Kametani, N Kamihara, JH Kang, SS Kapoor, K Katou, S Kelly, B Khachaturov, A Khanzadeev, J Kikuchi, DH Kim, DJ Kim, DW Kim, E Kim, GB Kim, HJ Kim, E Kistenev, A Kiyomichi, K Kiyoyama, C Klein-Boesing, H Kobayashi, L Kochenda, V Kochetkov, D Koehler, T Kohama, M Kopytine, D Kotchetkov, A Kozlov, PJ Kroon, CH Kuberg, K Kurita, Y Kuroki, MJ Kweon, Y Kwon, GS Kyle, R Lacey, V Ladygin, JG Lajoie, A Lebedev, S Leckey, DM Lee, S Lee, MJ Leitch, XH Li, H Lim, A Litvinenko, MX Liu, Y Liu, CF Maguire, YI Makdisi, A Malakhov, VI Manko, Y Mao, G Martinez, MD Marx, H Masui, F Matathias, T Matsumoto, PL McGaughey, E Melnikov, F Messer, Y Miake, J Milan, TE Miller, A Milov, S Mioduszewski, RE Mischke, GC Mishra, JT Mitchell, AK Mohanty, DP Morrison, JM Moss, F Muhlbacher, D Mukhopadhyay, M Muniruzzaman, J Murata, S Nagamiya, JL Nagle, T Nakamura, BK Nandi, M Nara, J Newby, P Nilsson, AS Nyanin, J Nystrand, E O'Brien, CA Ogilvie, H Ohnishi, ID Ojha, K Okada, M Ono, V Onuchin, A Oskarsson, I Otterlund, K Oyama, K Ozawa, D Pal, APT Palounek, VS Pantuev, V Papavassiliou, J Park, A Parmar, SF Pate, T Peitzmann, JC Peng, V Peresedov, C Pinkenburg, RP Pisani, F Plasil, ML Purschke, AK Purwar, J Rak, I Ravinovich, KF Read, M Reuter, K Reygers, V Riabov, Y Riabov, G Roche, A Romana, M Rosati, P Ros-

net, SS Ryu, ME Sadler, N Saito, T Sakaguchi, M Sakai, S Sakai, V Samsonov, L Sanfratello, R Santo, HD Sato, S Sato, S Sawada, Y Schutz, V Semenov, R Seto, MR Shaw, TK Shea, TA Shibata, K Shigaki, T Shiina, CL Silva, D Silvermyr, KS Sim, CP Singh, V Singh, M Sivertz, A Soldatov, RA Soltz, WE Sondheim, SP Sorensen, IV Sourikova, F Staley, PW Stankus, E Stenlund, M Stepanov, A Ster, SP Stoll, T Sugitate, JP Sullivan, EM Takagui, A Taketani, M Tamai, KH Tanaka, Y Tanaka, K Tanida, MJ Tannenbaum, P Tarjan, JD Tepe, TL Thomas, J Tojo, H Torii, RS Towell, I Tserruya, H Tsuruoka, SK Tuli, H Tydesjo, N Tyurin, HW van Hecke, J Velkovska, M Velkovsky, L Villatte, AA Vinogradov, MA Volkov, E Vznuzdaev, XR Wang, Y Watanabe, SN White, FK Wohn, CL Woody, W Xie, Y Yang, A Yanovich, S Yokkaichi, GR Young, IE Yushmanov, WA Zajc, C Zhang, S Zhou, SJ Zhou, and L Zolin. Identified charged particle spectra and yields in au plus au collisions at $\sqrt{s_{NN}}=200$ gev. *Physical Review C*, 69(3):034909, Jan 2004.

- [16] SS Adler, S Afanasiev, C Aidala, NN Ajitanand, Y Akiba, J Alexander, R Amirikas, L Aphetche, SH Aronson, R Averbeck, TC Awes, R Azmoun, V Babintsev, A Baldisseri, KN Barish, PD Barnes, B Bassalleck, S Bathe, S Batsouli, V Baublis, F Bauer, A Bazilevsky, S Belikov, Y Berdnikov, S Bhagavatula, JG Boissevain, H Borel, S Borenstein, ML Brooks, DS Brown, N Bruner, D Bucher, H Buesching, V Bumazhnov, G Bunce, JM Burward-Hoy, S Butsyk, X Camard, JS Chai, P Chand, WC Chang, S Chernichenko, CY Chi, J Chiba, M Chiu, IJ Choi, J Choi, RK Choudhury, T Chujo, V Cianciolo, Y Cobigo, BA Cole, P Constantin, D d'Enterria, G David, H Delagrangé, A Denisov, A Deshpande, EJ Desmond, A Devismes, O Dietzsch, O Drapier, A Drees, KA Drees, R Du Rietz, A Durum, D Dutta, YV Efremenko, K El Chenawi, A Enokizono, H En'yo, S Esumi, L Ewell, DE Fields, F Fleuret, SL Fokin, BD Fox, Z Fraenkel, JE Frantz, A Franz, AD Frawley, SY Fung, S Garpman, TK Ghosh, A Glenn, G Gogiberidze, M Gonnin, J Gosset, Y Goto, RG de Cassagnac, N Grau, SV Greene, MG Perdekamp, W Guryn, HA Gustafsson, T Hachiya, JS Haggerty, H Hamagaki, AG Hansen, EP Hartouni, M Harvey, R Hayano, N Hayashi, X He, M Heffner, TK Hemmick, JM Heuser, M Hibino, JC Hill, W Holzmann, K Homma, B Hong, A Hoover, T Ichihara, VV Ikonnikov, K Imai, D Isenhower, M Ishihara, M Issah, A Isupov, BV Jacak, WY Jang, Y Jeong, J Jia, O Jinnouchi, BM Johnson, SC Johnson, KS Joo, D Jouan, S Kametani, N Kamihara, JH Kang, SS Kapoor, K Katou, S Kelly, B Khachaturov, A Khanzadeev, J Kikuchi, DH Kim, DJ Kim, DW Kim, E Kim, GB Kim, HJ Kim, E Kistenev, A Kiyomichi, K Kiyoyama, C Klein-Boesing, H Kobayashi, L Kochenda, V Kochetkov, D Koehler, T Kohama, M Kopytine, D Kotchetkov, A Kozlov, PJ Kroon, CH Kuberg, K Kurita, Y Kuroki, MJ Kweon, Y Kwon, GS Kyle, R Lacey, V Ladygin, JG Lajoie, A Lebedev, S Leckey, DM Lee, S Lee, MJ Leitch, XH Li, H Lim, A Litvinenko, MX Liu, Y Liu, CF Maguire, YI Makdisi, A Malakhov, VI Manko, Y Mao, G Martinez, MD Marx, H Masui, F Matathias, T Matsumoto, PL McGaughey, E Melnikov, F Messer, Y Miake, J Milan, TE Miller, A Milov, S Mioduszewski, RE Mischke, GC Mishra, JT Mitchell, AK Mohanty, DP Morrison, JM Moss, F Muhlbacher, D Mukhopadhyay, M Murrizaman, J Murata, S Nagamiya, JL Nagle, T Nakamura, BK Nandi, M Nara, J Newby, P Nilsson, AS Nyanin, J Nystrand, E O'Brien, CA Ogilvie, H Ohnishi, ID Ojha, K Okada, M Ono, V Onuchin, A Oskarsson, I Otterlund, K Oyama,

K Ozawa, D Pal, APT Palounek, V Pantuev, V Papavassiliou, J Park, A Parmar, SF Pate, T Peitzmann, JC Peng, V Peresedov, C Pinkenburg, RP Pisani, F Plasil, ML Purschke, AK Purwar, J Rak, I Ravinovich, KF Read, M Reuter, K Reygers, V Riabov, Y Riabov, G Roche, A Romana, M Rosati, P Rosnet, SS Ryu, ME Sadler, N Saito, T Sakaguchi, M Sakai, S Sakai, V Samsonov, L Sanfratello, R Santo, HD Sato, S Sato, S Sawada, Y Schutz, V Semenov, R Seto, MR Shaw, TK Shea, TA Shibata, K Shigaki, T Shiina, CL Silva, D Silvermyr, KS Sim, CP Singh, V Singh, M Sivertz, A Soldatov, RA Soltz, WE Sondheim, SP Sorensen, IV Sourikova, F Staley, PW Stankus, E Stenlund, M Stepanov, A Ster, SP Stoll, T Sugitate, JP Sullivan, EM Takagui, A Taketani, M Tamai, KH Tanaka, Y Tanaka, K Tanida, MJ Tannenbaum, P Tarjan, JD Tepe, TL Thomas, J Tojo, H Torii, RS Towell, I Tserruya, H Tsuruoka, SK Tuli, H Tydesjo, N Tyurin, HW van Hecke, J Velkovska, M Velkovsky, V Veszpremi, L Villatte, AA Vinogradov, MA Volkov, E Vznuzdaev, XR Wang, Y Watanabe, SN White, FK Wohn, CL Woody, W Xie, Y Yang, A Yanovich, S Yokkaichi, GR Young, IE Yushmanov, WA Zajc, C Zhang, S Zhou, SJ Zhou, and L Zolin. Measurement of transverse single-spin asymmetries for midrapidity production of neutral pions and charged hadrons in polarized p+p collisions at root s=200 gev. *Phys. Rev. Lett.*, 95(20):202001, Jan 2005.

- [17] SS Adler, S Afanasiev, C Aidala, NN Ajitanand, Y Akiba, J Alexander, R Amirikas, L Aphecetche, SH Aronson, R Averbeck, TC Awes, R Azmoun, V Babintsev, A Baldisseri, KN Barish, PD Barnes, B Bassalleck, S Bathe, S Batsouli, V Baublis, A Bazilevsky, S Belikov, Y Berdnikov, S Bhagavatula, JG Boissevain, H Borel, S Borenstein, ML Brooks, DS Brown, N Bruner, D Bucher, H Buesching, V Bumazhnov, G Bunce, JM Burward-Hoy, S Butsyk, X Camard, JS Chai, P Chand, WC Chang, S Chernichenko, CY Chi, J Chiba, M Chiu, IJ Choi, J Choi, RK Choudhury, T Chujo, V Cianciolo, Y Cobigo, BA Cole, P Constantin, DG d'Enterria, G David, H Delagrang, A Denisov, A Deshpande, EJ Desmond, O Dietzsch, O Drapier, A Drees, R Du Rietz, A Durum, D Dutta, YV Efremenko, K El Chenawi, A Enokizono, H En'yo, S Esumi, L Ewell, DE Fields, F Fleuret, SL Fokin, BD Fox, Z Fraenkel, JE Frantz, A Franz, AD Frawley, SY Fung, S Garpman, TK Ghosh, A Glenn, G Gogiberidze, M Gonin, J Gosset, Y Goto, RG de Casagnac, N Grau, SV Greene, MG Perdekamp, W Guryn, HA Gustafsson, T Hachiya, JS Haggerty, H Hamagaki, AG Hansen, EP Hartouni, M Harvey, R Hayano, X He, M Heffner, TK Hemmick, JM Heuser, M Hibino, JC Hill, W Holzmann, K Homma, B Hong, A Hoover, T Ichihara, VV Ikonnikov, K Imai, D Isenhower, M Ishihara, M Issah, A Isupov, BV Jacak, WY Jang, Y Jeong, J Jia, O Jinnouchi, BM Johnson, SC Johnson, KS Joo, D Jouan, S Kametani, N Kamihara, JH Kang, SS Kapoor, K Katou, S Kelly, B Khachaturov, A Khanzadeev, J Kikuchi, DH Kim, DJ Kim, DW Kim, E Kim, GB Kim, HJ Kim, E Kistenev, A Kiyomichi, K Kiyoyama, C Klein-Boesing, H Kobayashi, L Kochenda, V Kochetkov, D Koehler, T Kohama, M Kopytine, D Kotchetkov, A Kozlov, PJ Kroon, CH Kuberg, K Kurita, Y Kuroki, MJ Kweon, Y Kwon, GS Kyle, R Lacey, V Ladygin, JG Lajoie, A Lebedev, S Leckey, DM Lee, S Lee, MJ Leitch, XH Li, H Lim, A Litvinenko, MX Liu, Y Liu, CF Maguire, YI Makdisi, A Malakhov, VI Manko, Y Mao, G Martinez, MD Marx, H Masui, F Matathias, T Matsumoto, PL McGaughey, E Melnikov, F Messer, Y Miake, J Milan, TE Miller, A Milov, S Mioduszewski, RE Mischke,

- GC Mishra, JT Mitchell, AK Mohanty, DP Morrison, JM Moss, F Muhlbacher, D Mukhopadhyay, M Muniruzzaman, J Murata, S Nagamiya, JL Nagle, T Nakamura, BK Nandi, M Nara, J Newby, P Nilsson, AS Nyanin, J Nystrand, E O'Brien, CA Ogilvie, H Ohnishi, ID Ojha, K Okada, M Ono, V Onuchin, A Oskarsson, I Otterlund, K Oyama, K Ozawa, D Pal, APT Palounek, VS Pantuev, V Papavassiliou, J Park, A Parmar, SF Pate, T Peitzmann, JC Peng, V Peresedov, C Pinkenburg, RP Pisani, F Plasil, ML Purschke, AK Purwar, J Rak, I Ravinovich, KF Read, M Reuter, K Reygers, V Riabov, Y Riabov, G Roche, A Romana, M Rosati, P Rosnet, SS Ryu, ME Sadler, N Saito, T Sakaguchi, M Sakai, S Sakai, V Samsonov, L Sanfratello, R Santo, HD Sato, S Sato, S Sawada, Y Schutz, V Semenov, R Seto, MR Shaw, TK Shea, TA Shibata, K Shigaki, T Shiina, CL Silva, D Silvermyr, KS Sim, CP Singh, V Singh, M Sivertz, A Soldatov, RA Soltz, WE Sondheim, SP Sorensen, IV Sourikova, F Staley, PW Stankus, E Stenlund, M Stepanov, A Ster, SP Stoll, T Sugitate, JP Sullivan, EM Takagui, A Taketani, M Tamai, KH Tanaka, Y Tanaka, K Tanida, MJ Tannenbaum, P Tarjan, JD Tepe, TL Thomas, J Tojo, H Torii, RS Towell, I Tserruya, H Tsuruoka, SK Tuli, H Tydesjo, N Tyurin, HW van Hecke, J Velkovska, M Velkovsky, L Villatte, AA Vinogradov, MA Volkov, E Vznuzdaev, XR Wang, Y Watanabe, SN White, FK Wohn, CL Woody, W Xie, Y Yang, A Yanovich, S Yokkaichi, GR Young, IE Yushmanov, WA Zajc, C Zhang, S Zhou, and L Zolin. High-p(t) charged hadron suppression in au+au collisions at $\sqrt{s_{NN}}=200$ gev. Physical Review C, 69(3):034910, Jan 2004.
- [18] SS Adler, M Allen, G Alley, R Amirkas, Y Arai, TC Awes, KN Barish, F Barta, S Batsouli, and S Belikov. Phenix on-line systems. Nuclear Inst. and Methods in Physics Research, A, 499(2-3):560–592, 2003.
- [19] SS Adler, T Chujo, EJ Desmond, L Ewell, TK Ghosh, JS Haggerty, T Ichihara, BV Jacak, SC Johnson, and HJ Kehayias. Phenix on-line and off-line computing. Nuclear Inst. and Methods in Physics Research, A, 499(2-3):593–602, 2003.
- [20] S Agostinelli, J Allison, K Amako, J Apostolakis, H Araujo, P Arce, M Asai, D Axen, S Banerjee, and G Barrand. Geant4—a simulation toolkit. Nuclear Inst. and Methods in Physics Research, A, 506(3):250–303, 2003.
- [21] N. N Ajitanand, J. M Alexander, P Chung, W. G Holzmann, M Issah, Roy A Lacey, A Shevel, and A Taranenko. Decomposition of harmonic and jet contributions to particle-pair correlations at ultrarelativistic energies. Physical Review C, 72(1), Jul 2005.
- [22] M Alford, A Schmitt, K Rajagopal, and T Schäfer. Color superconductivity in dense quark matter. Reviews of Modern Physics, Jan 2008.
- [23] M Allen, MJ Bennett, M Bobrek, JB Boissevain, S Boose, E Bosze, C Britton, J Chang, CY Chi, and M Chiu. Phenix inner detectors. Nuclear Inst. and Methods in Physics Research, A, 499(2-3):549–559, 2003.
- [24] C Amsler, M Doser, M Antonelli, DM Asner, KS Babu, H Baer, HR Band, RM Barnett, E Bergren, and J Beringer. Review of particle physics. Phys Lett B, 667(1-5):1–6, 2008.

- [25] Nestor Armesto, Matteo Cacciari, Tetsufumi Hirano, James L Nagle, and Carlos A Salgado. Constraint fitting of experimental data with a jet quenching model embedded in a hydrodynamical bulk medium. [arXiv](#).
- [26] SH Aronson, J Bowers, J Chiba, G Danby, A Drees, O Fackler, A Franz, JP Freidberg, W Guryn, and A Harvey. Phenix magnet system. Nuclear Inst. and Methods in Physics Research, A, 499(2-3):480–488, 2003.
- [27] Alejandro Ayala, Eleazar Cuautle, Isabel Dominguez, Antonio Ortiz, and Guy Paic. Fine structure in the azimuthal transverse momentum correlations at $\sqrt{s_{NN}} = 200$ gev using the event shape analysis. [arXiv](#), hep-ph, Jan 2009.
- [28] B B Back. The phobos perspective on discoveries at rhic, Jan 2005.
- [29] R Baier. Radiative energy loss of high energy quarks and gluons in a finite-volume quark-gluon plasma. Nuclear Physics B, 483(1-2):291–320, Jan 1997.
- [30] R Baier, D Schiff, and BG Zakharov. Energy loss in perturbative qcd, Jan 2000.
- [31] S Bass, C Gale, A Majumder, and C Nonaka. Systematic comparison of jet energy-loss schemes in a realistic hydrodynamic medium. Physical Review C, Jan 2009.
- [32] A Bettini. Introduction to Elementary Particle Physics. Cambridge, 2008.
- [33] K Boyle. Measurements of the double helicity asymmetry in pion production in proton collisions at $s = 200$ gev and the resulting constraints on the polarized gluon distribution in the proton. pages 1–211, Mar 2009.
- [34] P Braun-Munzinger and J Stachel. The quest for the quark–gluon plasma. Nature, Jan 2007.
- [35] Wojciech Broniowski, Wojciech Florkowski, and Leonid Ya Glozman. Update of the hagedorn mass spectrum. Phys. Rev. D, 70(11), Dec 2004.
- [36] J Casalderrey-Solana, E V Shuryak, and D Teaney. Hydrodynamic flow from fast particles. PoS, CFRNC2006:022, 2006.
- [37] A Chikanian, BS Kumar, N Smirnov, and E OBrien. A momentum reconstruction algorithm for the phenix spectrometer at brookhaven. Nucl Instrum Meth A, 371(3):480–488, Jan 1996.
- [38] John C Collins, Davison E Soper, and George Sterman. Factorization of hard processes in qcd. [arXiv](#), hep-ph, Jan 2004.
- [39] David d’Enterria. Jet quenching. [arXiv](#), nucl-ex, Jan 2009.
- [40] S Duerr, Z Fodor, J Frison, C Hoelbling, R Hoffmann, S. D Katz, S Krieg, T Kurth, L Lellouch, T Lippert, K. K Szabo, and G Vulvert. Ab initio determination of light hadron masses. Science, 322(5905):1224–1227, Jan 2008.
- [41] Adrian Dumitru, Francois Gelis, Larry McLerran, and Raju Venugopalan. Glasma flux tubes and the near side ridge phenomenon at RHIC. Nucl. Phys., A810:91, 2008.

- [42] Editors. Asymptotic freedom wins nobel. CERN Courier, November, 2004.
- [43] R K Ellis, W J Stirling, and B R Webber. QCD and Collider Physics. Cambridge University Press, 1996.
- [44] S Gubser, S Pufu, and A Yarom. Sonic booms and diffusion wakes generated by a heavy quark in thermal gauge-string Phys. Rev. Lett., Jan 2008.
- [45] R Hagedorn. On the hadronic mass spectrum. Il Nuovo Cimento A (1965-1970), Jan 1967.
- [46] H Hahn, E Forsyth, H Foelsche, M Harrison, J Kewisch, G Parzen, S Peggs, E Raka, A Ruggiero, and A Stevens. The rhic design overview. Nuclear Inst. and Methods in Physics Research, A, 499(2-3):245–263, 2003.
- [47] F Halzen and A D Martin. Quarks and Leptons: an introductory course in modern particle physics. Wiley, 1984.
- [48] M Harrison, T Ludlam, and S Ozaki. Rhic project overview. Nuclear Inst. and Methods in Physics Research, A, 499(2-3):235–244, 2003.
- [49] R Hwa. Hadron correlations in jets and ridges through parton recombination. pages 1–55, Apr 2009.
- [50] C De Jager, H De Vries, and C De Vries. Nuclear charge-and magnetization-density-distribution parameters from elastic electron At. Data Nucl. Data Tables, Jan 1974.
- [51] J Jia. Jiangyong’s thesis: High-pt charged hadron suppression in au au collisions. bnl.gov, Jan 2003.
- [52] F Karsch, E Laermann, and A Peikert. Quark mass and flavour dependence of the qcd phase transition. Nuclear Physics, Jan 2001.
- [53] D Kharzeev. Parton saturation and npart scaling of semi-hard processes in qcd. Phys Lett B, 561(1-2):93–101, May 2003.
- [54] Volker Koch. Introduction to chiral symmetry. arXiv, nucl-th, Jan 1995.
- [55] L Landau and I Pomeranchuk. Dokl. Akad. Nauk Ser. Fiz., 92:535, 1953.
- [56] L McLerran and R VENUGOPALAN. Computing quark and gluon distribution-functions for very large nuclei. Phys. Rev. D, 49(5):2233–2241, Jan 1994.
- [57] A B Migdal. Physical Review.
- [58] Michael L Miller, Klaus Reygers, Stephen J Sanders, and Peter Steinberg. Glauber modeling in high-energy nuclear collisions, Jan 2007.
- [59] A Milov. Charged particle multiplicity measurement in au-au collisions using the pad chambers of the phenix detector at rhic.

- [60] JT Mitchell, Y Akiba, L Aphecetche, R Averbek, TC Awes, V Baublis, A Bazilevsky, MJ Bennett, H Buesching, and J Burward-Hoy. Event reconstruction in the phenix central arm spectrometers. Nuclear Inst. and Methods in Physics Research, A, 482(1-2):491–512, 2002.
- [61] B Müller and J Nagle. Results from the relativistic heavy ion collider. Annual Reviews, Jan 2006.
- [62] Mateusz Ploskon. Two particle azimuthal correlations at high transverse momentum in pb-au at 158 agev/c. Nuclear Physics A, 783(1-4):527 – 530, 2007. Proceedings of the 2nd International Conference on Hard and Electromagnetic Probes of High-Energy Nuclear Collisions - Hard Probes 2006.
- [63] Antonio D Polosa and Carlos A Salgado. Jet shapes in opaque media. Physical Review C, 75(4):041901, Jan 2007.
- [64] Thomas Schfer. Nearly perfect fluidity. Physics, 2:88, Oct 2009.
- [65] Edward Shuryak. The Fate of the Initial State Perturbations in Heavy Ion Collisions. Phys. Rev., C80:054908, 2009.
- [66] Anne Sickles, Michael P McCumber, and Andrew Adare. Extraction of correlated jet pair signals in relativistic heavy ion collisions. arXiv, nucl-ex, Jan 2009. to be submitted to PRC.
- [67] Michael J Tannenbaum. Review of hard scattering and jet analysis. arXiv, nucl-ex, Jan 2006.
- [68] Thomas A Trainor. Zyam and v2: Underestimating jet yields from dihadron azimuth correlations.
- [69] Ramona Vogt. Ultrarelativistic Heavy Ion Collisions. Elsevier, 2007.
- [70] Quan Wang and Fuqiang Wang. Non-flow correlations in a cluster model.
- [71] Xin-Nian Wang. Resolving minijets in the minimum-biased events of hadronic interactions. Phys Rev D, 1992.
- [72] Rui Wei and for the PHENIX Collaboration. Phenix measurements of azimuthal anisotropy for pi0 production at high pt in au+au collisions at 200 gev. arXiv, nucl-ex, Jan 2009.
- [73] F Wilczek. Asymptotic freedom: From paradox to paradigm. Proceedings of the National Academy of Sciences, Jan 2005.
- [74] H. Zhang, J. F. Owens, E. Wang, and X. N. Wang. Phys. Rev. Lett., 103:032302, 2009.

Appendix A

Correlation functions and conditional pair multiplicities

In this section the mathematical notation and definitions of correlation functions and conditional yields are explained, followed by a summary of some relevant results preceding this analysis.

A.0.1 General pair correlation functions

A correlation function¹ describes the coincidence of production of particles selected in a category A with those of type B into elements of phase space $d^3\mathbf{p}_A$ and $d^3\mathbf{p}_B$ around the momentum vectors \mathbf{p}_A and \mathbf{p}_B in an event sample:

$$C(\mathbf{p}_A, \mathbf{p}_B) \equiv \frac{\frac{1}{N_{evt}} \frac{d^6 N^{AB}}{d^3\mathbf{p}_A d^3\mathbf{p}_B}}{\left(\frac{1}{N_{evt}} \frac{d^3 N^A}{d^3\mathbf{p}_A} \right) \left(\frac{1}{N_{evt}} \frac{d^3 N^B}{d^3\mathbf{p}_B} \right)} \quad (\text{A.1})$$

If A and B are completely uncorrelated, the numerator factorizes in the same way as for the denominator, and $C = 1$. In practice, the A and B particle classes occupy some well-defined region in phase space since they are constrained by detector acceptance and selections applied in an analysis. When A and B are binned into phase space regions Γ_A and Γ_B , the ‘‘factorized’’ correlation function is defined as

$$C_{\text{Factorized}} = \frac{\int_{\Gamma_A} d^3\mathbf{p}_A \int_{\Gamma_B} d^3\mathbf{p}_B \frac{1}{N_{evt}} \frac{d^6 N^{AB}}{d^3\mathbf{p}_A d^3\mathbf{p}_B}}{\left(\int_{\Gamma_A} d^3\mathbf{p}_A \frac{1}{N_{evt}} \frac{d^3 N^A}{d^3\mathbf{p}_A} \right) \left(\int_{\Gamma_B} d^3\mathbf{p}_B \frac{1}{N_{evt}} \frac{d^3 N^B}{d^3\mathbf{p}_B} \right)} \quad (\text{A.2})$$

¹ This section is closely based on work originally done by Paul Stankus (*stankuspw@ornl.gov*), which is documented in PHENIX Technical Note 412. Currently the document is not publically available. For a related discussion, see appendix A of [7].

A.0.2 Angular correlations

The focus of this analysis is on azimuthal correlations, in which the full the full polar angle acceptance of the PHENIX detector is integrated over for each trigger and partner momentum bin \mathcal{A}, \mathcal{B} to give the azimuthal single-particle and pair distributions:

$$\frac{1}{N_{evt}} \frac{dN^A}{d\phi_A} \equiv \int_{\mathcal{A}} dp_A d\theta_A \frac{1}{N_{evt}} \frac{d^3 N^A}{dp_A d\theta_A d\phi_A} \quad (\text{same for B}) \quad (\text{A.3})$$

$$\frac{1}{N_{evt}} \frac{d^2 N^{AB}}{d\phi_A d\phi_B} \equiv \int_{\mathcal{A}} dp_A d\theta_A \int_{\mathcal{B}} dp_B d\theta_B \frac{1}{N_{evt}} \frac{d^6 N^{AB}}{dp_A d\theta_A d\phi_A dp_B d\theta_B d\phi_B} \quad (\text{A.4})$$

The phase-space region for relative angles between A and B includes the parameters for each type, connected within the integration through $\delta(\Delta\phi - (\phi_A - \phi_B))$. Thus the relative azimuthal correlation function is

$$C(\Delta\phi) \equiv \frac{\int_0^{2\pi} d\phi_A \int_0^{2\pi} d\phi_B \delta(\Delta\phi - (\phi_A - \phi_B)) \frac{1}{N_{evt}} \frac{d^2 N^{AB}}{d\phi_A d\phi_B}}{\int_0^{2\pi} d\phi_A \int_0^{2\pi} d\phi_B \delta(\Delta\phi - (\phi_A - \phi_B)) \left(\frac{1}{N_{evt}} \frac{dN^A}{d\phi_A} \frac{1}{N_{evt}} \frac{dN^B}{d\phi_B} \right)} \quad (\text{A.5})$$

$$= \frac{2\pi}{n^A n^B} \int_0^{2\pi} d\phi_A \int_0^{2\pi} d\phi_B \delta(\Delta\phi - (\phi_A - \phi_B)) \frac{1}{N_{evt}} \frac{d^2 N^{AB}}{d\phi_A d\phi_B} \quad (\text{A.6})$$

A.0.3 Conditional pair multiplicities

The quantity of final interest in correlations analyses is typically the yield of correlated pairs *per* trigger particle, which is equivalent to describing the probability of obtaining a certain number of type B particles, given the existence of a type A particle. This conditional relative-angle pair distribution is a distinct quantity from that defined in equation A.2, which makes no distinction between type A and B particles in the sense that they could be exchanged without affecting the result.

The probability of obtaining a type B particle given the presence of A (equivalent to obtaining an AB pair given A) is

$$\frac{d^3 n^{B|A}}{d^3 \mathbf{p}_B}(\mathbf{p}_A, \mathbf{p}_B) = \frac{\frac{1}{N_{evt}} \frac{d^6 N^{AB}}{d^3 \mathbf{p}_A d^3 \mathbf{p}_B}}{\frac{1}{N_{evt}} \frac{d^3 N^A}{d^3 \mathbf{p}_A}} \quad (\text{A.7})$$

More specifically, the conditional $\Delta\phi$ pair multiplicity is the azimuthal pair distribution divided by the number of trigger particles. Using the definitions in equations A.3-A.4 and integrating over the appropriate phase space intervals gives

$$\begin{aligned} n^{B|A}(\Delta\phi) &= \frac{1}{N^A} \frac{dN^{AB}}{d(\Delta\phi)} \equiv \frac{\int_0^{2\pi} d\phi_A \int_0^{2\pi} d\phi_B \delta(\Delta\phi - (\phi_A - \phi_B)) \frac{1}{N_{evt}} \frac{d^2 N^{AB}}{d\phi_A d\phi_B}}{\int_0^{2\pi} d\phi_A \frac{1}{N_{evt}} \frac{dN^A}{d\phi_A}} \\ &= \frac{1}{n^A} \int_0^{2\pi} d\phi_A \int_0^{2\pi} d\phi_B \delta(\Delta\phi - (\phi_A - \phi_B)) \frac{1}{N_{evt}} \frac{d^2 N^{AB}}{d\phi_A d\phi_B} \quad (\text{A.8}) \end{aligned}$$

This expression differs from equation A.6 only in the prefactor, immediately providing a connection between the conditional pair yield of equation A.8 and $C(\Delta\phi)$:

$$\frac{1}{N^A} \frac{dN^{AB}}{d(\Delta\phi)} = \frac{n^B}{2\pi} C(\Delta\phi) \quad (\text{A.9})$$

The experimental procedure for calculating these quantities and for extracting the correlations due to jets from those of other sources is described in detail in chapter 3.

Appendix B

The negative binomial distribution

The negative binomial distribution (NBD) is a discrete probability distribution of the number of failures in a sequence of Bernoulli trials needed to get a specified number of successes. It is sometimes called Pascal's distribution when the number of desired outcomes is integer-valued. It gives a complementary result to that specified by a binomial distribution. For example, if one throws a die repeatedly until the third time a 6 appears, the probability distribution of "non-6's" appearing before the third 6 is a NBD.

The probability density function is

$$f_{NB}(n; k, p) = \binom{n+k-1}{k-1} p^k (1-p)^n \quad (\text{B.1})$$

where

- p : probability to get desired outcome
- $k - 1$: number of occurrences of desired outcome
- n : number of failures

The binomial coefficient can be expressed with Gamma functions, giving the following representation:

$$f_{NB}(n; k, p) = \frac{\Gamma(n+k)}{n! \Gamma(k)} p^k (1-p)^n. \quad (\text{B.2})$$

The probability can be expressed in terms of the mean μ as

$$p = \frac{k}{k + \mu} \quad (\text{B.3})$$

so that the NBD can be expressed as

$$g_{NB}(n; k, \mu) = \frac{\Gamma(n + k)}{n! \Gamma(k)} \frac{(\mu/k)^n}{(1 + \mu/k)^{n+k}} \quad (\text{B.4})$$

In the limit that the number of successes k is very large, the NBD becomes a Poisson distribution:

$$\lim_{k \rightarrow \infty} g_{NB}(n; \mu) = \frac{\mu^n}{n!} e^{-\mu}. \quad (\text{B.5})$$

Thus the NBD possesses similar properties to the Poisson, where k controls the deviation from Poisson behavior, and the NBD has a larger variance for small k values. The variance is related to k and μ as

$$\left(\frac{\sigma}{\mu}\right)^2 = \frac{1}{k} + \frac{1}{\mu}. \quad (\text{B.6})$$

Again, in the limit of large k values the relation $\sigma^2 = \mu$ is recovered, which is a characteristic feature of the Poisson distribution.

Appendix C

Run lists for Runs 6 and 7

Bad Run 7 runs: 229545 230083 230680 231156 235889 235890 235891 235892
235893 235894 235895 235900 235901 235902 236004 236005 236007 236008 236009
236137 238327 238530 238531 238682 238683 238684 238698 238843 238845 238846
238847 238848 238971 239306 239307 239308 239312 229793 228640 236385 239834
239914 240043 232459 230249 240073 232459 231717 235804 228339 239839 230665
229680 234523 236465

Appendix D

$\pi^0 \rightarrow 2\gamma$ decay kinematics

D.1 Minimum and maximum decay photon energies

The photon energy limits can be obtained by Lorentz-boosting the photon 4-momentum from the decay center of mass to the lab.

$$\begin{pmatrix} E_\gamma \\ p_{\gamma\parallel} \end{pmatrix} = \begin{pmatrix} \gamma & \gamma\beta \\ \gamma\beta & \gamma \end{pmatrix} \begin{pmatrix} E_\gamma^* \\ p_{\gamma\parallel}^* \end{pmatrix} \quad (\text{D.1})$$

Here, p_{\parallel} is the photon momentum pointing in the direction of the parent momentum, and the starred frame is the decay CM. If the angle in the parent rest frame between the emitted photon and p_{\parallel} is ψ^* , the photon energy in the lab is then

$$E_\gamma = \gamma \frac{m}{2} (1 + \beta \cos \psi^*). \quad (\text{D.2})$$

The minimum and maximum E_γ occurs when photon emission is antiparallel and parallel to the parent momentum, respectively:

$$E_\gamma^{(\min)} = \frac{1}{2} (E_p \mp p_p). \quad (\text{D.3})$$

D.2 Distribution of decay angles

The parent-daughter angle distribution of photons is sought as a function of parent momentum for parent $\rightarrow 2\gamma$ decays. We begin by boosting the decay photon from the

lab to the (starred) decay CM,

$$\begin{pmatrix} E_\gamma^* \\ p_{\gamma\parallel}^* \end{pmatrix} = \begin{pmatrix} \gamma & -\gamma\beta \\ -\gamma\beta & \gamma \end{pmatrix} \begin{pmatrix} E_\gamma \\ p_{\gamma\parallel} \end{pmatrix} \quad (\text{D.4})$$

or, more explicitly,

$$\begin{pmatrix} \frac{m}{2} \\ \frac{m}{2} \cos \psi^* \end{pmatrix} = \begin{pmatrix} \gamma & -\gamma\beta \\ -\gamma\beta & \gamma \end{pmatrix} \begin{pmatrix} E_\gamma \\ E_\gamma \cos \psi \end{pmatrix}. \quad (\text{D.5})$$

Applying the boost gives

$$\frac{m}{2} = \gamma E_\gamma (1 - \beta \cos \psi) \quad (\text{D.6})$$

and

$$\frac{m}{2} \cos \psi^* = \gamma E_\gamma (\cos \psi - \beta). \quad (\text{D.7})$$

Dividing (D.7) by (D.6) gives

$$\cos \psi^* = \frac{\cos \psi - \beta}{1 - \beta \cos \psi}. \quad (\text{D.8})$$

We write

$$\frac{dN_\gamma}{d\psi} = \frac{dN_\gamma}{d \cos \psi^*} \frac{d \cos \psi^*}{d \cos \psi} \frac{d \cos \psi}{d\psi} \quad (\text{D.9})$$

Assuming that photon emission is isotropic in the decay CM, $\frac{dN_\gamma}{d \cos \psi^*}$ is uniform from -1 to 1, so we say that it is 1/2 for unit normalization. Performing the derivatives then yields the result

$$\frac{dN_\gamma}{d\psi} = \frac{(1 - \beta^2) \sin \psi}{2(1 - \beta \cos \psi)^2}. \quad (\text{D.10})$$

Since the decay angle distribution is constrained by the momentum of the photon as well as the parent, the allowable angular range for a given E_γ bin is a relevant quantity and is obtained by arranging equation D.6 as

$$\cos \psi = \frac{1}{\beta} \left(1 - \frac{m}{2\gamma E_\gamma} \right) \quad (\text{D.11})$$

or, expressing in terms of parent energy and momenta and noting that the E_γ and ψ are inversely related,

$$\cos \psi^{(\min)} = \frac{E_p}{p_p} \left(1 - \frac{m^2}{2E_p E_\gamma^{(\min)}} \right). \quad (\text{D.12})$$

Appendix E

PC3 recalibration

E.1 PC3 match distributions from embedding output

E.2 Matching distributions from PISA simulations

E.2.1 Run 6

The matching parameters and their fits are shown in figure E.4 (***) Need to update these figs? Check.).

The quality of the fits could be improved by fitting the two charges separately (as done for the embedding study in section 4.3.1), but it was decided that the accuracy of the PISA matching recalibration was sufficient for this study, particularly in comparison to the data. In almost all bins, the recalibrated values of $\mu(\sigma)$ agree with 0(1) within 0.1σ . A notable exception is a jump in the widths below 1.0 GeV, however the larger values appear for the kaons and protons, which are strongly de-weighted at low p_T ($w \sim 0.1$) when the species are combined. A systematic uncertainty of will be assigned for imperfections in the matching recalibration.

E.2.2 Run 7 embedding simulation output

Once this correction was applied, the means and widths of the matching distributions were at their proper values within 10% (figure E.6).

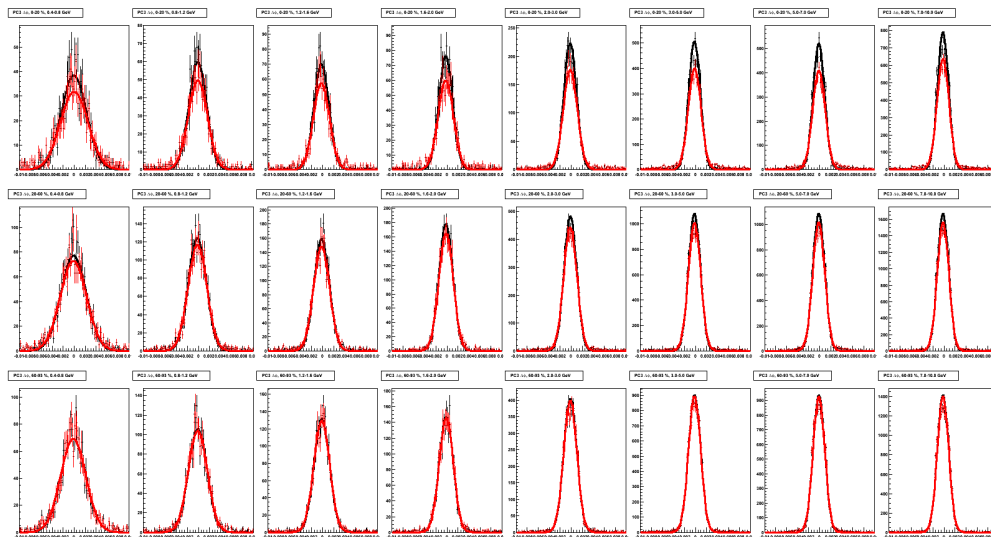


Figure E.1: PC3 $\Delta\phi$ raw matching distributions from embedding output in radians for type S (black) and type R (red) tracks.

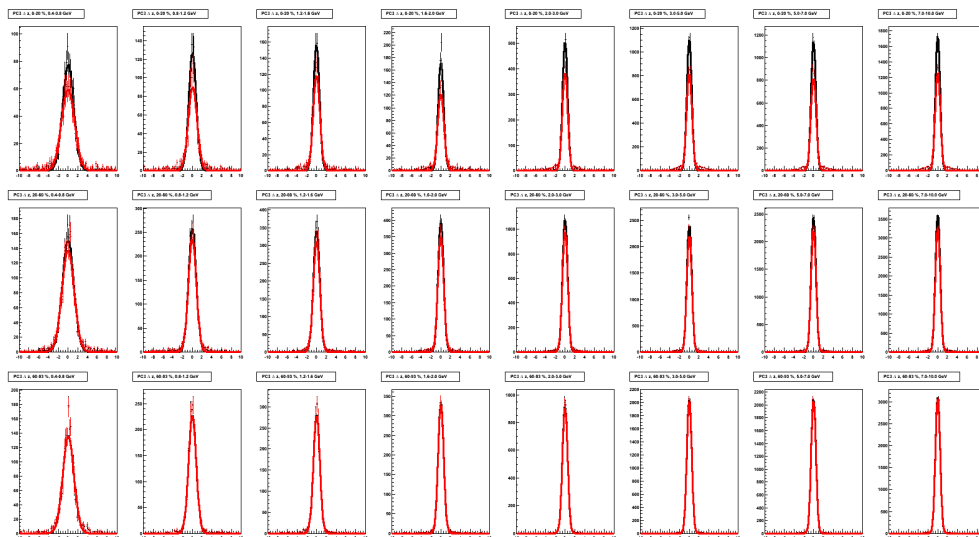


Figure E.2: PC3 Δz raw matching distributions from embedding output in cm for type S (black) and type R (red) tracks.

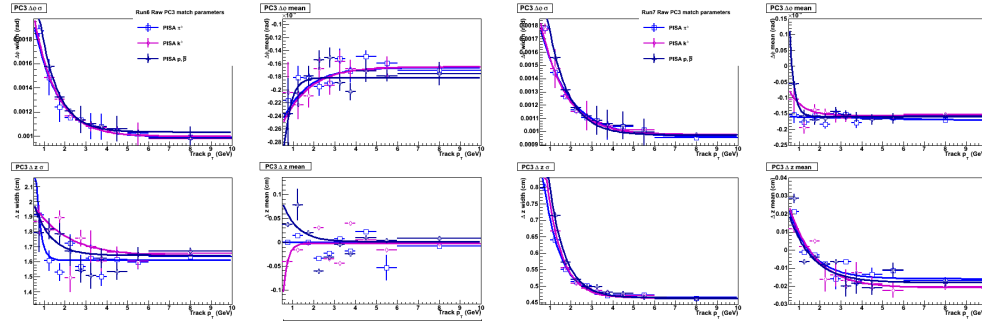


Figure E.3: Run 6 (left) and Run 7 (right) fits to the raw matching parameters vs. p_T . Some fits are imprecise but the resulting recalibrated widths and means remained within a few percent of their target values.

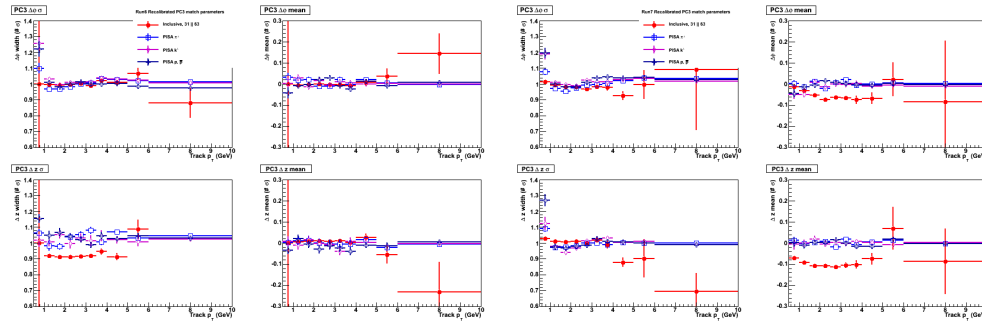


Figure E.4: Run 6 (left) and Run 7 (right) widths and means of recalibrated, signalized PC3 matching parameters.

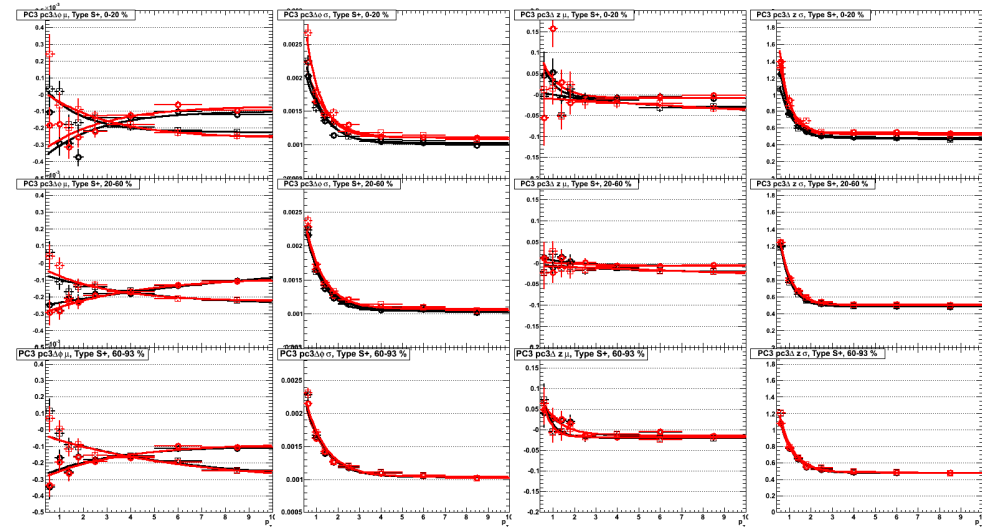


Figure E.5: PC3 $\Delta\phi$ and dz widths and means in radians and cm as a function of p_T for + and - tracks. Black = type S, and red = type R. The fits are used to recalibrate the data.

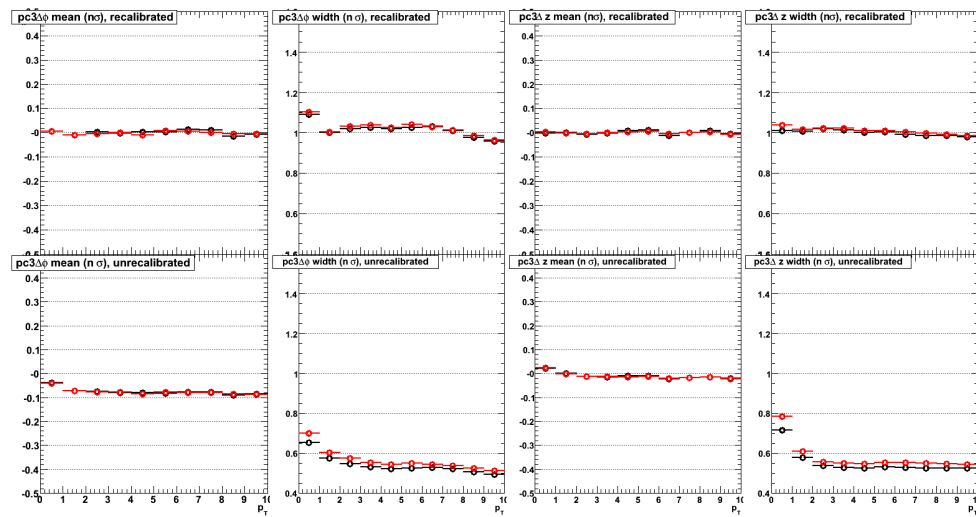


Figure E.6: Recalibrated (top) and un-recalibrated means and widths of PC3 matching distributions in units of σ .

Appendix F

Correlation Functions

F.1 $p+p$

F.2 Au+Au

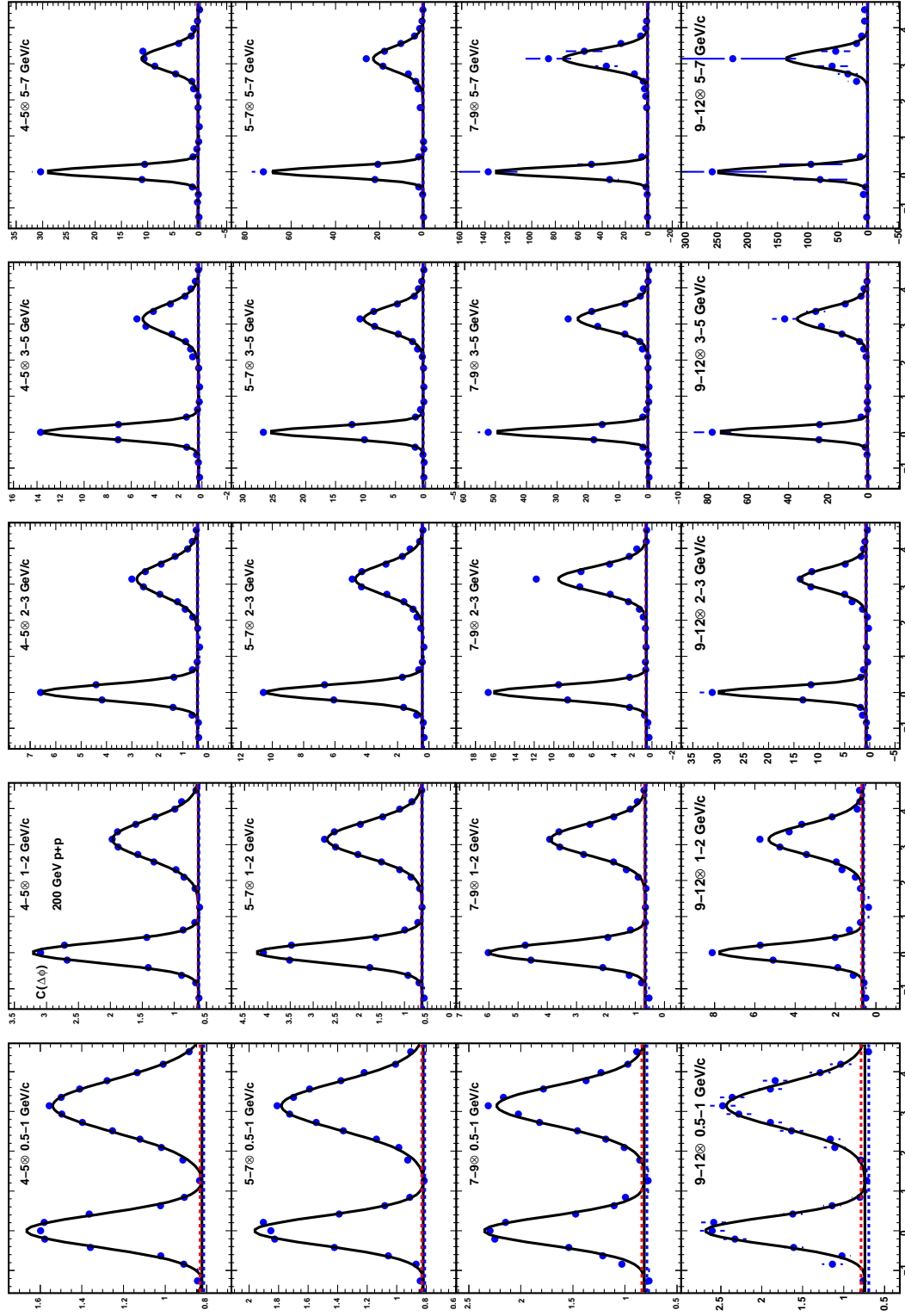


Figure F.1: p+p Correlation functions.

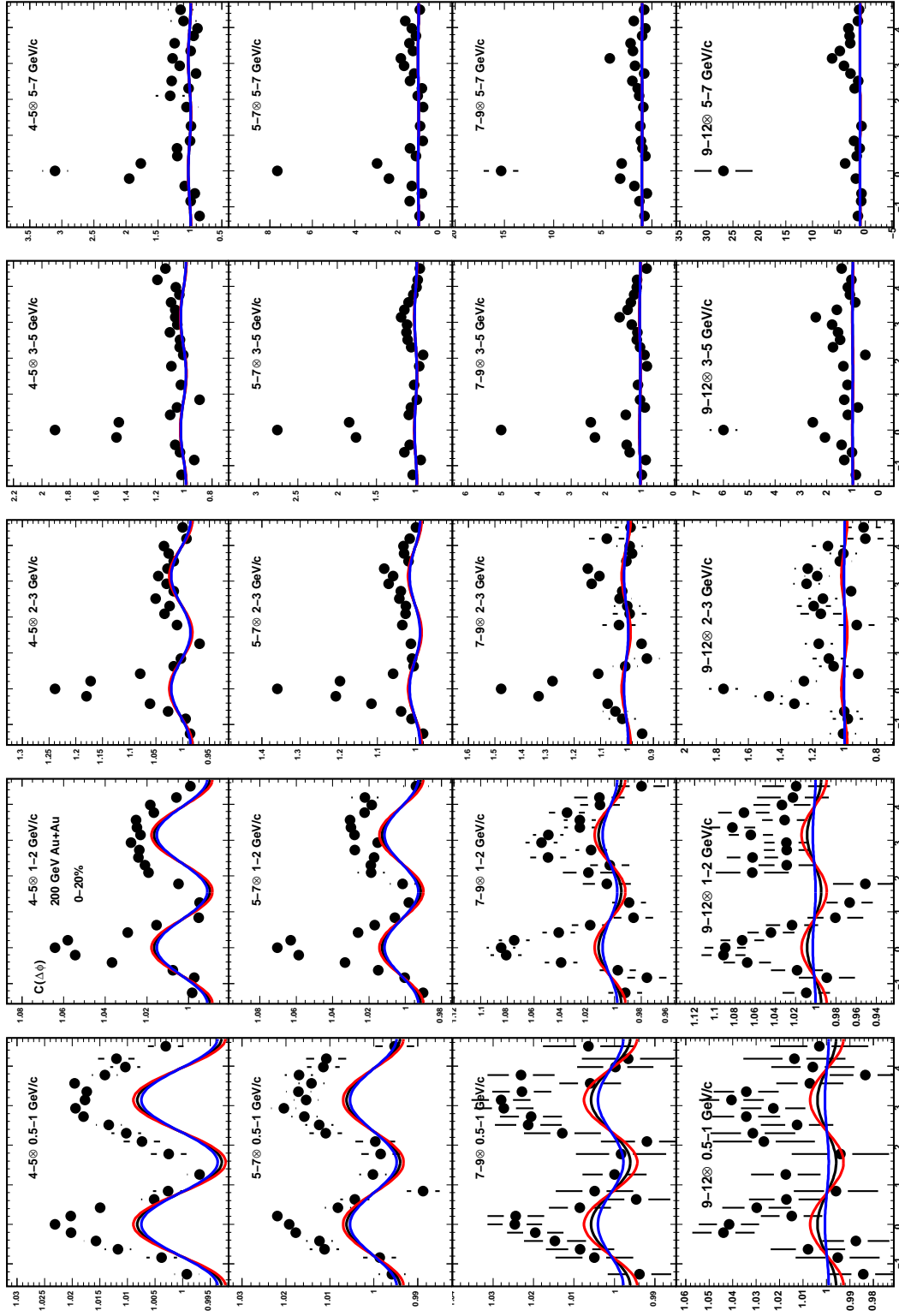


Figure F.2: Au+Au Correlation functions, 0-20%.

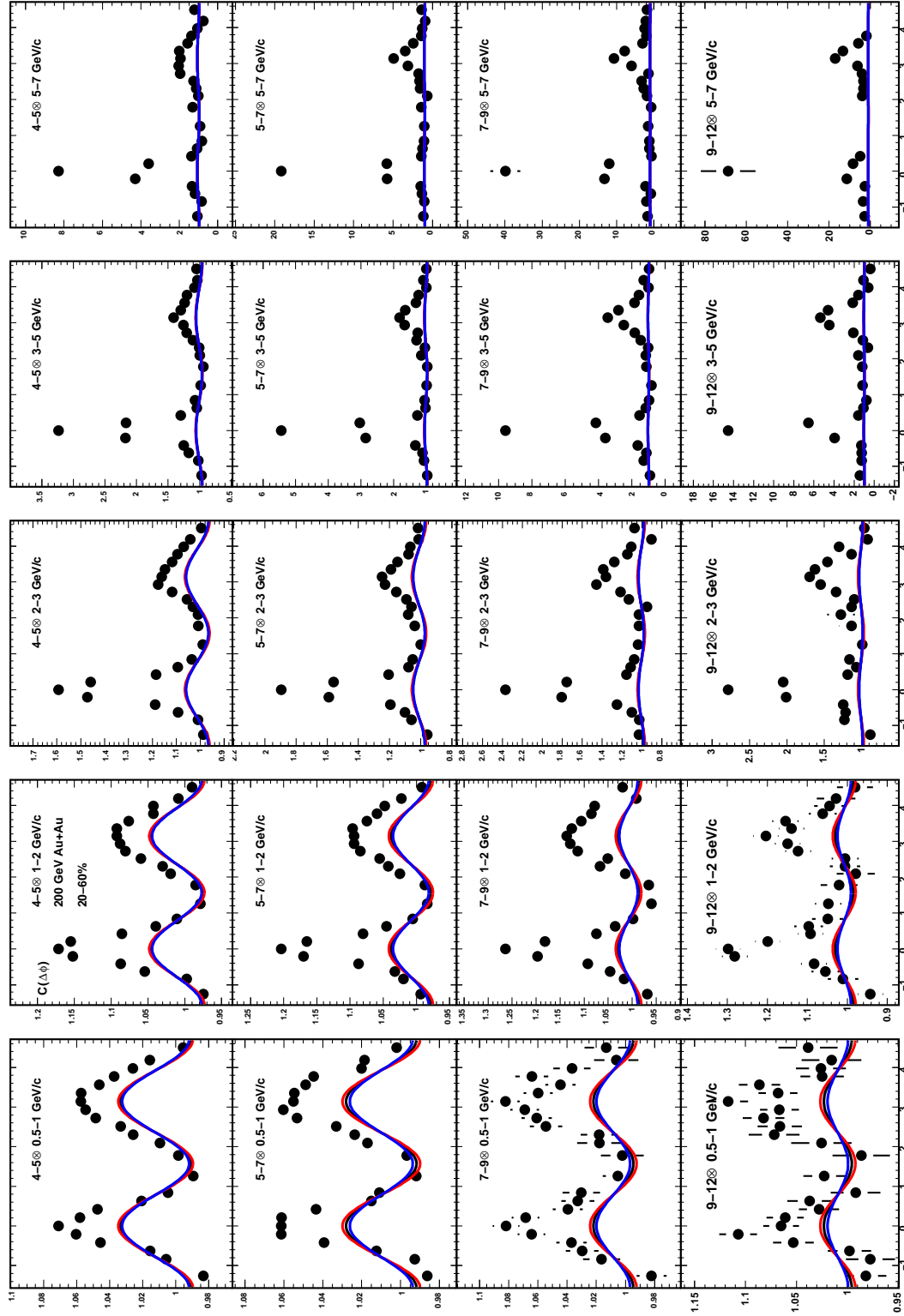


Figure F.3: Au+Au Correlation functions, 20-60%.